DETERMINATION OF THE MECHANICAL PROPERTIES OF THE PORCINE THORACIC AORTA AND AN ANALYSIS OF THE STRESS CONCENTRATION IN FIBER REINFORCED NONLINEAR SOLIDS

A Dissertation

by

MANOJ MYNENI

Submitted to the Graduate and Professional School of
Texas A&M University
in partial fulfillment of the requirements for the degree of

DOCTOR OF PHILOSOPHY

Co-Chairs of Committee,	Kumbakonam R. Rajagopal
	Chandler C. Benjamin
Committee Members,	John C. Criscione
	Alan D. Freed
	Joseph E. Pasciak
Head of Department,	Andreas A. Polycarpou

December 2021

Major Subject: Mechanical Engineering

ABSTRACT

Knowledge of the mechanical properties of the thoracic aorta and determining appropriate constitutive relations are essential in developing computational methodologies for accurate prognosis of vascular diseases like aortic aneurysm and dissection. We study tearing and uniaxial properties of the porcine thoracic aorta, and investigate the influence of certain constitutive assumptions on the local stress distribution around a circular hole in two-fiber reinforced materials.

We performed peeling experiments on the ascending and the descending segments of the porcine thoracic aorta to evaluate its tearing characteristics. The stretch experienced by the peeled halves, peel force per unit width and peeling energy per unit area reveal segment-specific differences in the tearing characteristics of the porcine thoracic aorta. Further, the influence of non-linear mechanical response of the aorta on the estimation of the peeling energy per unit area is investigated.

Using uniaxial extension tests, we examine the directional variation of the mechanical properties of the porcine thoracic aorta. Dumbbell-shaped samples are cut from the aortic wall at five different orientations with respect to the circumferential direction of the aorta and are subjected to cyclic uniaxial extension and extension until failure. Specimens in all the orientations considered show a nonlinear constitutive response that is typical of collagenous soft tissues. Shear strain under uniaxial extension demonstrates clearly discernible anisotropy of the mechanical response of the porcine aorta. The samples oriented at 45° and 60° with respect to the circumferential direction show a peculiar crescent-shaped shear strain-nominal stretch response. Failure stress indicates a decreasing tensile strength of the porcine aortic wall from the circumferential direction to the longitudinal direction.

The forms of the stored energy function that are commonly used for modeling arteries are dependent only on a subset of the full invariant set that is necessary to model two-fiber reinforced materials. We study the influence of such assumptions on the deformation and the stress distribution around a small circular hole in a thin nonlinearly elastic large sheet reinforced by two families

of fibers undergoing large deformations. Results indicate a strong influence of the constitutive assumptions on the stress concentration factors. A significant difference in the stress concentration factor distribution around the hole is observed when using a constitutive relation based on a partial set of invariants (I_4, I_6) versus an "extended" constitutive relation that incorporates the full set of invariants appropriate for a body reinforced with fibers and reduces appropriately to the orthotropic linearized elastic case. We show how two constitutive relations that exhibit a similar biaxial behavior in the absence of discontinuities display noticeable differences in the presence of discontinuities like a circular hole.

DEDICATION

To family, friends, teachers and gurus.

ACKNOWLEDGMENTS

I thank my advisors, Professor K. R. Rajagopal and Professor Chandler Benjamin, for their constant support throughout my PhD. I am grateful to Professor Rajagopal for giving me his time and counsel during my graduate studies. His emphasis on careful thought and language will stick with me for the rest of my career. Dr. Benjamin has always been available for any question, advice, or help I needed. I could not have imagined a more approachable and friendly advisor than Dr. Benjamin. I also thank Prof. Criscione, Prof. Freed, and Prof. Pasciak for serving on the dissertation committee. I am thankful to Akshay Rao, Mingliang Jiang and Raghuveer Lalitha Sridhar for their important contributions to the experimental work I pursued.

I want to thank my friends and lab mates for making my stay in College Station and my journey through my PhD enjoyable.

I am grateful to my family for providing me the encouragement for the successful completion of this work.

CONTRIBUTORS AND FUNDING SOURCES

Contributors

This work was supported by a dissertation committee consisting of Professor K. R. Rajagopal [advisor] and Professor Chandler Benjamin [co-advisor] of the Department of Mechanical Engineering and Alan Freed of the Department of Mechanical Engineering and Professor John Criscione of the Department of Biomedical Engineering and Professor Joseph Pasciak of the Department of Mathematics.

Chapter 2 of this dissertation was completed by the student in collaboration with Akshay Rao and Mingliang Jiang of the Department of Mechanical Engineering. Chapter 3 was completed in collaboration with Raghuveer Lalitha Sridhar of the Department of Mechanical Engineering. All other work was completed by the student independently.

Funding Sources

This study was funded by Texas Engineering Experiment Station (TEES). The student received the dissertation fellowship from the Office of Graduate and Professional Studies of Texas A&M University in his final year. Its contents are solely the responsibility of the authors and do not necessarily represent the official views of the TEES.

TABLE OF CONTENTS

Page

LIST OF FIGURES

FIGURE Page

LIST OF TABLES

TABLE Page

1. INTRODUCTION

Thoracic aortic disease comprises of a range of degenerative, structural and traumatic disorders and presentations. Deaths due to the diseases of the aorta and its branches account for 43,000 to 47,000 annually in the United States [5]. Although the number of deaths due to thoracic aortic disease remains unclear, it is generally believed to cause twice the number of deaths as that of abdominal aortic aneurysms. The two most common presentations of the thoracic aortic disease are aortic aneurysm, which is an abnormal dilatation of the aorta, and aortic dissection, which is a catastrophic separation of the layers of the aorta. Recent estimates indicate a rising incidence of death caused by thoracic aortic aneurysms and dissections worldwide[6]. The incidence of thoracic aortic aneurysms is estimated to be 10.4 per 100,000 people per year, while that of aortic dissection is estimated at 3 to 6 per 100,000 people per year in the United States.

Current guidelines for the treatment of thoracic aortic aneurysms are based on the maximum aortic diameter and its growth rate. Thoracic aortic aneurysms grow in size at an average rate of 0.10 cm to 0.29 cm annually. They remain mostly asymptomatic during this growth phase until a catastrophic event like dissection or rupture occurs. Due to the absence of suggestive symptoms, an estimated 95% of the thoracic aortic aneurysms (TAA) remain undiagnosed until they rupture or dissect[7]. A surgical intervention is recommended when the diameter of the TAA is 5.5cm or greater [5]. If comorbidities like bicuspid aortic valve and Marfan syndrome are present, an earlier surgical intervention is recommended. For the ascending aortic aneurysms, a diameter beyond 6.0cm increases the probability of devastating complications by 25.2%. For the descending aortic aneurysms, a diameter of 7.0cm is known to appreciably increase the risk of rupture [8]. However, 31% of the patients would have already suffered a dissection or rupture before an aneurysm reaches a diameter of 6.0 cm in the ascending aorta, and 43% of the patients suffer dissection or rupture before the diameter of the descending aorta reaches 7.0 cm.

A criterion for surgical intervention purely based on diameter and its growth rate is too simplistic to be a reliable predictor of outcome in patients harboring an aneurysm ([9],[7]). Recent

experimental studies on thoracic aortic aneurysms identified alterations in the mechanical behavior and microstructural composition of the aneurysmatic tissue when compared to a non-aneurysmal tissue ([10], [11], [12], [13], [14]). This knowledge led to the exploration of various biomechanical criteria like wall stress, distensibility, equivalent diameter, etc., for providing a better estimation of the patient specific risk of aneurysm rupture ([15], [16]). However, as mentioned in a recent review by Martufi et al.[17], the threshold or cut-off values for the various biomechanical indices are yet to be defined, and clinical studies evaluating these indices are lacking. Understanding the mechanical properties of healthy and aneurysmatic aortic tissue in the presence of various comorbidities like bicuspid aortic valve, atherosclerosis, connective tissue disorders, etc., is essential in developing and evaluating such criteria.

Aortic dissection, unlike an aneurysm, cannot be detected before its occurrence[18]. An intimal tear is present in 90% of the cases of aortic dissection. It allows blood to enter the aortic wall resulting in a false channel (also called false lumen) that obstructs the flow of blood to lower organs[5]. Due to similarities in symptoms with other cardiac events, many aortic dissections(AD) are routinely misdiagnosed as myocardial infarctions[19]. Stanford and Debakey classifications are commonly used to stratify the types of aortic dissections[2] (see figure 1.1b). Stanford type-A (Debakey type I and type II) dissection involving the ascending aorta occurs in two-thirds of the aortic dissection cases and has an associated 40% immediate mortality. Stanford type-B (Debakey type III) dissection involving the descending aorta occurs in one-thirds of the cases and is more chronic in nature. Despite significant advances in the diagnosis and management of aortic dissection, in-hospital mortality rates of patients with an aortic dissection remain high[20]. Various studies on the pathogenesis of aortic dissection suggest that aortic dissection is the end process of several pathological and microstructural changes occurring in aortic wall[21]. These changes occur due to normal ageing as well as pathological changes associated with several risk factors. Aortic dissection is commonly associated with a number of risk factors of which the most important are chronic hypertension, atherosclerosis, bicuspid aortic valve, presence of aortic aneurysm, and connective tissue disorders like Marfan syndrome, Ehlers-Danlos syndrome, etc.[20]. The high

mortality rates due to aortic dissection can only be reduced through the understating of diseased aortic conditions that may lead to the initiation and the propagation of aortic dissection.

In the following section, we summarize the experimental and computational methods employed to investigate the mechanics of thoracic aortic aneurysm and dissection.

1.1 Mechanical characterization of thoracic aortic aneurysm and dissection

The knowledge of the anatomic structure of the aortic wall helps us in understanding the experimental techniques employed to analyze its mechanical behavior and form a perspective on the experimental observations reported in literature. The aorta is a conduit that originates from heart and supplies oxygenated blood to the systemic vasculature. Arteries are generally classified based on their mechanical function as elastic (storing energy during systole and releasing energy during diastole) and muscular arteries. The aorta and other large arteries are regarded as elastic arteries. Human aortic diameter and wall thickness decreases from the aortic root to the abdominal aorta [22]. The aortic wall is anatomically divided three layers, each having distinct physiological function and microstructural composition: tunica intima, tunica media and tunica adventitia. Intima is the inner most layer of all blood vessels. It contains endothelial cells, a basal lamina containing mainly type-IV collagen, and connective tissue. In aorta, a subendothelial layer is also present which contains connective tissue, smooth muscle cells and some fibroblasts [1]. Media is the thickest layer of the thoracic aorta containing alternating layers of elastic tissue and smooth muscle cells. These layers are reinforced by collagen fibers. Thickness of these musculo-elastic fascicles remains nearly constant across the wall thickness but their number decreases with increasing distance from the heart. Adventitia is the outermost layer consisting of a network of collagen fibers interspersed with elastin, nerves, fibroblasts. In the thoracic aorta, adventitia also contains vasa vasorum, a network of small blood vessels supplying nutrients to outer media. The main function of the adventitia is thought to be the protection of aorta against overdistension. Nevertheless, the contribution of adventitia to the mechanical behaviour of aorta cannot be neglected. Figure 1.1a shows a schematic of the aortic wall.

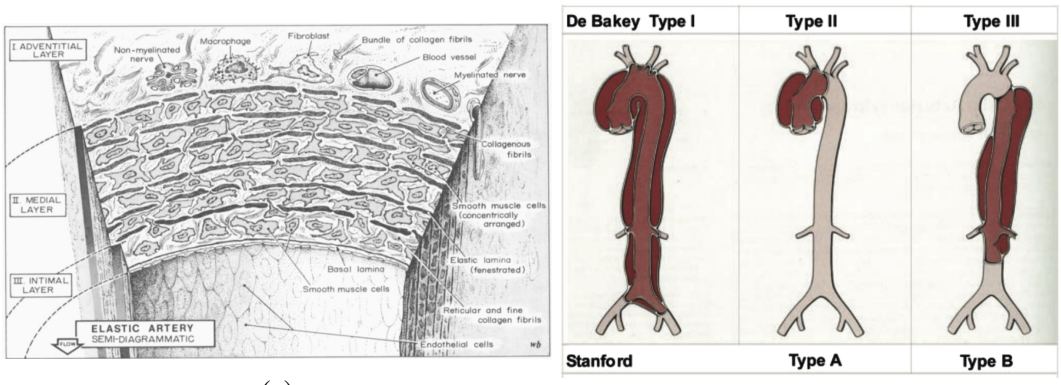

(a) (b)

Figure 1.1: (a) Schematic of the aortic wall[1] (b) Classification of aortic dissection[2].

Previous studies investigated the tensile, tearing and rupture properties of the healthy and diseased thoracic aortic tissue as well as the properties of the individual layers ([17], [16], [23]). Compositional differences have also been identified between the healthy and the diseased tissues [13]. Below, we provide a brief overview of the experimental work on the mechanical characterization of the thoracic aorta and its aneurysms and dissections.

1.1.1 Uniaxial and biaxial tests

Extensive studies on the mechanical characterization of the ascending thoracic aortic aneurysmatic tissue were undertaken in the past two decades using uniaxial and biaxial experiments. Almost all these experiments were conducted on rectangular, square, or dumbbell shaped specimens cut along the circumferential and the longitudinal directions of the aorta. Mohan and Melvin ([24], [25]) conducted uniaxial and biaxial tests on the non-diseased human thoracic aorta obtained from cadavers to determine quasistatic and dynamic rupture properties. They observed that the stretch at which failure occurs is similar under quasistatic and dynamic loading. The stress at failure, however, was significantly higher in dynamic tests compared to quasistatic tests. Uniaxial experiments by Vorp et al.[10] on ascending thoracic aortic aneurysm (ATAA) identified a significantly lower failure strength (Circ: ATAA = 1.18$\pm$0.12 MPa versus non-ATAA = 1.80 $\pm$ 0.24 MPa, Long: ATAA = 1.21$\pm$0.09 MPa versus non-ATAA = 1.71 $\pm$ 0.14 MPa) and a significantly

higher maximum tangent modulus (Circ: ATAA = 4.48$\pm$0.59 Mpa versus non-ATAA = 2.61 $\pm$ 0.26 MPa, Long: ATAA = 4.61$\pm$0.42 MPa versus non-ATAA = 3.25 $\pm$ 0.63 MPa) for the ATAA tissue compared to a non-aneurysmal tissue. However, Iliopoulos et al. [26] later showed that, when the specimens are age-matched, the uniaxial tensile strength remains similar between the aneurysmatic and non-aneurysmatic tissue. Sokolis et al. [27] later confirmed this observation. They further showed significant regional variations (along the circumference of the aorta) in the tensile strength, wall thickness and maximum elastic modulus in ascending thoracic aneurysms. Sokolis et al. [12] examined the directional (circumferential vs. longitudinal) and region-specific (anterior, right lateral, posterior, left lateral) uniaxial failure properties of the intima, the media and the adventitial layers of ATAAs. The medial and the adventitial layers exhibited higher failure strength in the circumferential direction compared to the longitudinal direction, while the intimal layer demonstrated statistically insignificant difference between the two directions. Garcia-Herrera et al. [28] studied the uniaxial tensile properties of the non-aneurysmal and the aneurysmal aorta from patients with and without a bicuspid aortic valve. They found a strong influence of age on tensile properties. Compared to the effect due to age, the pathologies did not seem to have a discernible effect on the rupture strength. Aneurysmatic tissue operated in the stiffer portion of the stress-strain curve while healthy tissues operated in the heel region of the stress-strain curve. Based on their uniaxial tensile tests on ATAA, Khanafer et al.[29] suggested a strong positive correlation between the failure stress and the maximum elastic modulus and an inverse correlation between the failure stress and the local thickness of the tissue. A study by Pichamuthu et al.[30] revealed the higher tensile strength of the aneurysmatic tissue in patients with bicuspid aortic valves (BAV) compared to patients with tricuspid aortic valves. Intriguingly, patients with BAV are more prone to the development and rupture of an aneurysm compared to TAV patients. Ferrara et al. [31] in a large study on 403 ATAA specimens reported higher uniaxial tensile strength of the male aneurysmatic aorta compared to the female aneurysmatic aorta. All these uniaxial studies reported higher tensile strength in the circumferential direction compared to the longitudinal direction of the aorta.

In vivo loading on the aorta or an aortic aneurysm is far from being uniaxial. Internal pressure

and axial stretch acting on the aorta induce a biaxial state of loading. Therefore, a biaxial test would provide better insight into the response of the aorta under in vivo loads compared to a uniaxial test. Okamata et al.[32] conducted planar biaxial tests on square specimens of the dilated human ascending aorta. They observed a reduction in the strain at which tissue specimens start rapid stiffening in older patients ($>$ 50 years) compared to younger patients ($<$ 50 years), confirming the hypothesis based on uniaxial tests that the aneurysmatic tissue is much stiffer than the healthy tissue. A later study by Pham et al.[33] provided more evidence to this hypothesis. They noticed that the areal strain under biaxial extension at a given stress level was lower in an aneurysmatic tissue with BAV compared to the one without BAV. Choudhary et al.[34] examined the equibiaxial properties of the healthy and aneurysmatic tissues and reported a decrease in the elastin content and an increase in the collagen content in ATAA. Giuseppe et al.[35] reported significant regional differences between the biaxial mechanical responses of the tissue extracted from an aneurysm. In particular, the tissue obtained from the major curvature of a BAV aneurysm wall was less stiffer than that of a TAV aneurysm wall. This suggests a local weakening in patients with BAV.

While significant progress has been made in unravelling the uniaxial and the biaxial properties of thoracic aortic aneurysms, very few studies have focused on the uniaxial or biaxial properties of dissected aortic tissue. Manopoulos et al.[36] studied the tensile behavior of the individual layers of the dissected and the non-dissected thoracic aortic aneurysms. They observed a significant reduction in the tensile strength of the inner layers of the dissected aneurysms compared to non-dissected aneurysms. This observation gives an insight into why certain aneurysms dissect while others do not. So far, the only study reporting the mechanical behaviour of dissected ascending aortic specimens under biaxial testing is by Babu et al.[37]. Specimens from non-dissected half of the aortas from patients who suffered aortic dissection were tested under a load controlled biaxial protocol. They then obtained the stiffness values in the low (before the toe) and high stress (after the toe) portions of the stress-strain curves. Age did not have a significant effect on the dissected tissue stiffness. However, they observed a significantly higher stiffness in the high stress regime for dissected specimens compared to normal aortic stiffness reported in literature.

Maclean et al. [38] evaluated the tensile properties of the thoracic aorta in the radial direction. Sommer et al.[39] conducted uniaxial tests on coin shaped specimens punched out of the abdominal aortic wall with loading applied in the radial direction of the aorta. Tong et al.[40] performed similar experiments on carotid artery specimens. Overall, these tests indicate a significantly lower uniaxial tensile strength of the aorta in the radial direction (100-150 kPa) compared to the circumferential and the longitudinal directions (0.5-3 MPa).

1.1.2 Bulge inflation tests

Due to the anisotropic nature of the aorta and the loading experienced by it in vivo, the constitutive response and the failure properties obtained from the uniaxial tests may not be sufficient to characterize the tissue rupture in an aneurysm. Bulge-inflation tests, where a circular specimen extracted from an aorta is pressurized from one side to expand like a bubble, were conducted on ascending thoracic aortic aneurysms by Duprey, Arvil and colleagues to glean the rupture characteristics of the aneurysmatic tissue under internal pressure. Following paragraph reports some important observations from their investigation.

Kim et al.[41] studied the deformation undergone by ATAA specimens undergoing bulge inflation tests, and examined the direction of tear propagation during rupture. The tear propagated in an oblique manner closer to the circumferential direction, but not in the circumferential or the axial direction. Additionally they suggested the importance of local stress concentrations on the initiation of failure. Using bulge-inflation experiments, Romo et al.[42] showed that the rupture of the aorta occurred not at the location of highest stress but at a location where there is a localization of strain field and localized thinning of the vessel wall. Duprey et al.[14] compared the stress and stretch at rupture obtained from bulge-inflation tests with the failure properties obtained from uniaxial tests. The stress at rupture under inflation was closer to the uniaxial tensile strength along the axial direction. The stretch at rupture, however, was similar in all the tests. Davis et al.([43],[44]) studied the local mechanical properties of thoracic aortic aneurysms using a bulge inflation test. They showed the mechanically heterogeneous nature of the tissue at a length scale of 1mm and highlighted the importance of considering inhomogeneities at millimeter scale to evaluate the potential rupture

locations of aneurysms.

1.1.3 Strength of the aortic media determined through the infusion of fluid

During the chronic phase of Stanford type-B aortic dissection, tear propagation typically occurs in the outer thirds of the medial layer, resulting in the delamination of the aortic wall into two halves. Early research on the delamination strength of the aorta were conducted by examining the infusion pressure required to inject fluid into the media of the thoracic aorta using a hypodermic needle. Using this technique, Robertson and Smith[45] studied the dissection properties of the aortas from human cadavers obtained after autopsy. They investigated the variation of injection pressure (pressure required to inject fluid into the aortic wall) along the length of the aorta. They found that the pressure required to inject water was immensely higher ($>$500 mm Hg) than the in-vivo blood pressure and the injection pressure decreases as one moves away from the heart. Hirst and Johns[46] observed a decrease in injection pressure with age in human autopsy aortas. Also, longer exposure to high pressure increased the tendency of aorta to dissect. They observed that the aortas dissected when exposed to 430 mm Hg pressure for an hour.

Roach and colleagues carried out several studies on human and porcine aortas using the protocol described above. They opened the aorta longitudinally and injected fluid from the intimal side. They studied the pressure-volume relation of the bleb as the fluid was being injected into the aortic media using a video camera. The projected area on the video plane was used to calculate the energy required for dissection/injection. Carson and Roach[47] measured the mean pressure required to initiate dissection in porcine thoracic aortas was 77.2$\pm$1.5 kPa($\tilde{5}$79mmHg). Tiessen and Roach [48] measured the injection pressure in human autopsy aortas. According to their study, injection depth into the wall and age did not impact the medial strength. In calcified abdominal aortas (due to atherosclerosis), the tear went around the plaque rather than cutting through it. No clear conclusion was made on the effect of calcified plaques.

He and Roach[49] conducted infusion experiments on porcine descending thoracic aortas pressurized internally at 130 mmHg. They observed the difference in pressure between the lumen and the bleb to be 52$\pm$10 mmHg for the propagation to occur. Tam et al.[50] examined the influence

of tear depth on the peak pressure required for the infusion of fluid in porcine aortas. As noted by them, an increase in the depth of the tear decreased the peak pressure required for dissection.

1.1.4 Peeling experiments

While direct tension tests were used to quantify the radial failure strength of the aortic media, peeling experiments were used to measure the energy required for the propagation of a tear. Sommer et al. [39] used peel tests to study healthy human abdominal aortic media. Peeling energy per unit reference area(T) was calculated as 5.1$\pm$0.6 mJ/cm^2 for the circumferential specimens and 7.6$\pm$2.7 mJ/cm^2 for the axial specimens. Histological studies revealed a rougher dissection surface for axial specimens with several torn elastic fibers. The cut spread over 6-7 elastic laminae sometimes propagating towards the intimal side and sometimes towards the adventitial side. In contrast to axial specimens, circumferential specimens produced a smooth surface with dissection propagating between the same elastic lamina where the cut was made.

Tong et al.[40] conducted peeling experiments on human carotid bifurcations. Intima-media interface displayed lower peeling energy per unit area compared to adventitia-media interface. Also, they observed a significant difference in T for the specimens from common carotid artery near the bifurcations, and the carotid artery branches. Tong et al.[51] investigated T in thrombus covered wall specimens of abdominal aortic aneurysms. Two different displacement rates of the tongues, 1.0mm/min and 1.0 mm/sec, were used for peeling experiments. Higher displacement rate produced an average increase in the force values by 28%. As the thrombus ages, they observed a reduction in the amount of elastin and collagen in the wall. Additionally, the ratio of elastin to collagen significantly decreased with thrombus age. T also reduced with thrombus age for intima-media composite and anisotropic dissection properties disappeared.

Majority of the aortic dissections (67%) occur in the ascending aorta. Pasta et al.[52] investigated the variation of peeling energy in non-aneurysmal and aneurysmal human ascending thoracic aortas. They observed a significant reduction in peeling energy in diseased specimens compared to non aneurysmal specimens. Also, aneurysmal specimens with bicuspid aortic valve morphology showed lower peeling energy than those with tricuspid aortic valve(normal) morphology. Angouras

et al.[53] reported regional differences in the peel force per unit width in ascending thoracic aortic aneurysms. Also, peel force per unit width decreased with patient's age indicating an increased risk of dissection in older patients. Noble et al.[54] studied peeling energies of collagenase, elastase and gluteraldehyde treated porcine thoracic aortic specimens. Collagenase digests collagen, elastase digests elastin, and gluteraldehyde is known to create stable crosslinks within elastin and collagen. Collagenase treated specimens showed lower peeling energy than control specimens whereas elastase treatment showed little effect. Gluteraldehyde treatment not only increased the dissection energy but also reduced the difference between the axial and the circumferential dissection energies. These experiments suggest the role of collagen in the propagation of a tear during an aortic dissection.

Although dissections rarely occur in coronary arteries, Wang et al.[55] studied peeling energies in human coronary arteries from explanted hearts during cardiac transplantation. They also observed that the tear propagation in intima required higher average peeling energy than in media. Also, the distribution of peeling energies, as were commonly assumed, was not a normal distribution. Since dissection is a spatially varying process, they propose a need to change the commonly employed peeling protocol, which only gives the average peeling energy.

1.1.5 Theoretical and empirical models for evaluating thoracic aneurysm rupture risk and dissection propagation

Development of empirical or computational models to predict the rupture risk of an aneurysm or the occurrence of aortic dissection is essential to provide patient-specific prognosis of the thoracic aortic disease. Knowledge obtained from invasive in vitro mechanical characterization of aneurysmatic and dissected tissue aids the development of such models. Various biomechanical criteria have been proposed to evaluate the patient specific rupture risk in case of abdominal aortic aneurysms ([9], [17], [16]). Some attempts have been made recently to propose such criteria for thoracic aortic aneurysms, though clinical studies confirming their usability are lacking. Duprey et al.[14] suggested a normalized rupture criteria for aneurysm rupture based on the local collagen fiber angle and failure stress/stretch derived from bulge-inflation experiments. Luo et al.[56],

He et al. ([57], [58]) proposed machine-learning based correlations to evaluate the rupture risk of ATAAs. Liu et al.[59] proposed a novel probabilistic and anisotropic rupture risk criterion for ATAAs. This criterion is based on a generalization of the Tsai-Hill criterion, which has been applied in the past to simulate damage in anisotropic fiber reinforced composites. They applied this criterion to evaluate the rupture risk of 41 patient specific aneurysm geometries.

Parameters like stress, strain, etc., used in these criteria can be evaluated in patient-specific geometries only with the specification of an appropriate constitutive relation to model the mechanical behavior of the aorta. Different constitutive relations have been used to model the behavior of the aortic wall. Earlier studies on thoracic aortic aneurysms utilized the exponential Fung-type constitutive relations ([32], [60], [11], [26], [12]) to model the mechanical response under uniaxial and biaxial extension. Due to the lack of a clear physical association with any microstructural constituents of the extracellular matrix of the aorta for Fung-type exponential models, most of the recent studies employ fiber-based or microstructure-based constitutive relations that take into account the composition of the extracellular matrix (percentage of elastin, collagen, smooth muscle cells) and the distribution in the orientation of collagen fibers. Gasser and Holzapfel[61] presented a XFEM based approach to model tear propagation in an arterial wall. They used the two-fiber model proposed by Gasser et al.[62] to model the mechanical response of the artery. Ferrara and Pandolfi[63] combined a cohesive traction-separation law with the two fiber model to simulate tear propagation in an artery. A similar work based on cohesive zone formulation for cylindrical arterial geometries was presented by Wang et al.([64], [65]). Rausch et al[66] used a particle-continuum approach to model tear propagation in an aorta. A four-fiber family model proposed by Baek et al.[67] was utilized in their study. More recently, Gültekin and colleagues([68], [69]) developed a phase field approach to model crack propagation in an aorta. Korenczuk et al.[70] developed a multiscale model to evaluate the rupture risk of ascending thoracic aneurysms. Davis et al.([44], [43]) used a modified form of the two-fiber model to fit local deformations undergone by an aneurysm tissue under a bulge-inflation test. However, none of these models have been applied to predict the rupture risk of aneurysms or to model the propagation of dissection in vivo.

1.2 Outline of the current work

Earlier studies have indicated that the tearing properties of the aorta are dependent on the circumferential location from which the specimens are obtained. Also, there is a significantly higher incidence of aortic dissection and aneurysm in the ascending aorta compared to the descending aorta. Further, in several cases of aortic dissection the false lumen extends through the entire length of the aorta. Computational models for predicting the propagation of aortic dissection require the knowledge of the segment-specific (ascending, arch, descending, abdominal) tearing properties of the aorta in healthy and diseased states. **The first objective of this dissertation is to evaluate the segment-specific variation in the tearing properties of the porcine thoracic aorta**. We use porcine aorta for our experiments due to its similarities in mechanical response and microstructure with healthy young humans. *As a part of this study, we also investigate the influence of the nonlinear mechanical response of the aorta on the estimation of peeling energy per unit area*. Chapter 2 presents the details of this work.

Human and animal aortas are anisotropic, and various anisotropic constitutive relations have been used to model their mechanical response[71]. Most of these constitutive relations assume the aorta to have an orthotropic material symmetry with respect to the circumferential-radial, longitudinal-radial and circumferential-longitudinal planes. Material parameters for these constitutive relations are often determined by fitting the constitutive response data obtained from uniaxial and biaxial tests conducted on circumferentially and longitudinally oriented specimens to the theoretically predicted response. It is well-known that uniaxial and biaxial tests with loading applied along the directions of symmetry are insufficient to characterize the constitutive response of anisotropic materials (particularly the shear response). Yet, very few studies focus on the mechanical response and rupture characteristics of the aorta in the directions that do not coincide with the circumferential, longitudinal and radial directions. **The second objective of the current work is to determine the anisotropic constitutive response of the porcine thoracic aorta**. Uniaxial experiments were conducted on dumbbell shaped specimens oriented at five different angles with respect to the circumferential direction. *Further, we evaluate the efficacy of the constitutive param-*

eters determined from biaxial tests in predicting the anisotropic uniaxial response of the porcine thoracic aorta. We present the details of this work in chapter 3

The final objective of this dissertation is to investigate the deformation and the stress distribution around a small circular hole in a thin non-linearly elastic large sheet reinforced by two families of fibers. Local stress distribution and stress concentration factor around inhomogeneities become important in determining the location of rupture in an aortic aneurysm([41],[43], [44], [14]). Any inaccuracies in the local stress distribution predicted due to the use of simplified constitutive relations may lead to incorrect prognosis of the rupture risk of an aneurysm. The first constitutive relation we consider, called the standard-fiber reinforcing model, is derived from a stored energy function that is dependent on a partial set of invariants needed to model two-fiber reinforced materials. Such constitutive relations have been extensively used to model the response of biological tissues. Two-fiber models for arteries and myocardium due to Holzapfel and colleagues([72], [62], [73]), a four-fiber model for arteries due to Baek et al.[67] and models for the myocardium due to Humphrey and Yin ([74], [75]) are some examples of constitutive relations that are based on partial set of invariants. Muprhy, Horgan and colleagues ([76], [77], [78], [79], [80]) have showed the limitations of such models in modeling the shear and even the uniaxial mechanical behavior of anisotropic materials. Therefore, we consider a second constitutive relation that is an extension of the first relation to include all the invariants such that it reduces appropriately to the orthotropic linearized elastic constitutive relation. Chapter 4 provides description of the boundary value problems and the results of this study.

Finally, chapter 5 summarizes the important conclusions of this dissertation.

2. SEGMENTAL VARIATIONS IN THE PEEL CHARACTERISTICS OF THE PORCINE THORACIC AORTA

2.1 Introduction

Aortic dissection occurs predominantly in the thoracic aorta and the mechanisms for the initiation and the propagation of a tear in aortic dissection are not well understood. In this chapter, we study the tearing characteristics of the porcine thoracic aorta using a peeling test, and we estimate the peeling energy per unit area in the ascending and the descending segments. The stretch and the peel force per unit width undergone by the peeled halves of the rectangular specimens are measured. The influence of the nonlinear constitutive response of the porcine thoracic aorta on the estimation of peeling energy is investigated. A comparison between the peeling characteristics of different segments of the porcine thoracic aorta is presented.

Altered hemodynamics (typically hypertension) with a concomitant weakening of the aortic media due to aging and disease are the factors commonly associated with aortic dissection[81]. Canine and porcine models were previously used to examine the hemodynamic and structural factors influencing the tear propagation in aortic dissection ([23], [82]) due to the similarities with humans in terms of aortic diameter and microstructure. Knowledge of the mechanical properties of the thoracic aorta in good health and disease, particularly the rupture properties, is essential for understanding the predisposition for the initiation and propagation of a tear in aortic dissection.

Peeling test, trouser test, in-plane shear test are some of the techniques that have been used to analyze the tearing properties of the aorta [23]. Of interest here is the peeling test, in which, a tear created near the center of the thickness of a rectangular specimen is propagated through the full length of the specimen. Rivlin and Thomas[83] developed a framework to calculate the energy

required in creating a tear in polymeric materials undergoing large deformations. Sommer et al. [39] used peel tests to characterize the peel force per unit width and the energy required for the propagation of tear (peeling energy) in healthy human abdominal aortic media. The difference between the external work done and the internal stored energy was used for calculating the peeling energy. The energy stored in the peel specimen at the end of the test was calculated using a linear relationship between the first Piola-Kirchhoff stress in the peeled arms and the corresponding stretch. Small values of the first Piola-Kirchhoff stress was reported to be the reason for this assumption. This experimental protocol was applied to measure the peeling energy in healthy and diseased arteries.

Since the peel force/width required is much higher in the thoracic aorta (126 $\pm$ 6.6 N/m in circ, 149 $\pm$ in 7.6 N/m long[52]), where aortic dissection typically occurs[20], compared to the abdominal aorta (22.9 $\pm$ 2.9 N/m in circ, 34.8 $\pm$ 15.5 N/m in long[39]), it may not be appropriate to assume a linear relation between the first Piola-Kirchhoff stress and stretch for the estimation of internal energy in the thoracic aorta. A significant amount of the external work done during peeling could be stored in the peel specimen as internal energy. Assuming a linear relationship between stress and stretch may over or under predict the tearing energy depending on the stretches undergone by the peel specimen during the test. The difference in the peel force/width also indicates a segmental variation in the peel characteristics along the length of the aorta. The objectives of this study are two fold: 1) Measure the local stretch experienced in the peeled halves of a rectangular sample during the peel experiment and investigate the influence of the non-linear behaviour of the aorta in the estimation of peeling energy and 2) study the segmental variation in the peel characteristics of the porcine thoracic aorta.

2.2 Materials and Methods

Eleven porcine aortas were collected from the Rosenthal meat center on Texas A&M University campus and transported in ice. The aortas were obtained from 8 month old castrated male hogs of various breeds weighing about 250-300 lbs. The aorta was separated into the ascending (Asc) and the descending segments. The descending aorta was further divided into the upper descending

(Udes) or proximal and the lower descending (Ldes) or distal segments at the third branching arteries. After the removal of the loose connective tissue, the samples were stored at -20°C in centrifuge tubes containing 0.01M Phosphate Buffer Saline (PBS) solution. The day before the experiments, samples were taken out and were allowed to slowly thaw overnight in a refrigerator at 4°C. Two circumferential and two longitudinal rectangular specimens were dissected from each segment of the thoracic aorta. Figure 2.1 illustrates the location of the samples within each segment. One set of circumferentrial and longitudinal specimens from each segment were used for peel tests. The remaining set was used for uniaxial tests. Testing was performed within 2-3 months after obtaining the aortas. No animals were killed for the purpose of this study.

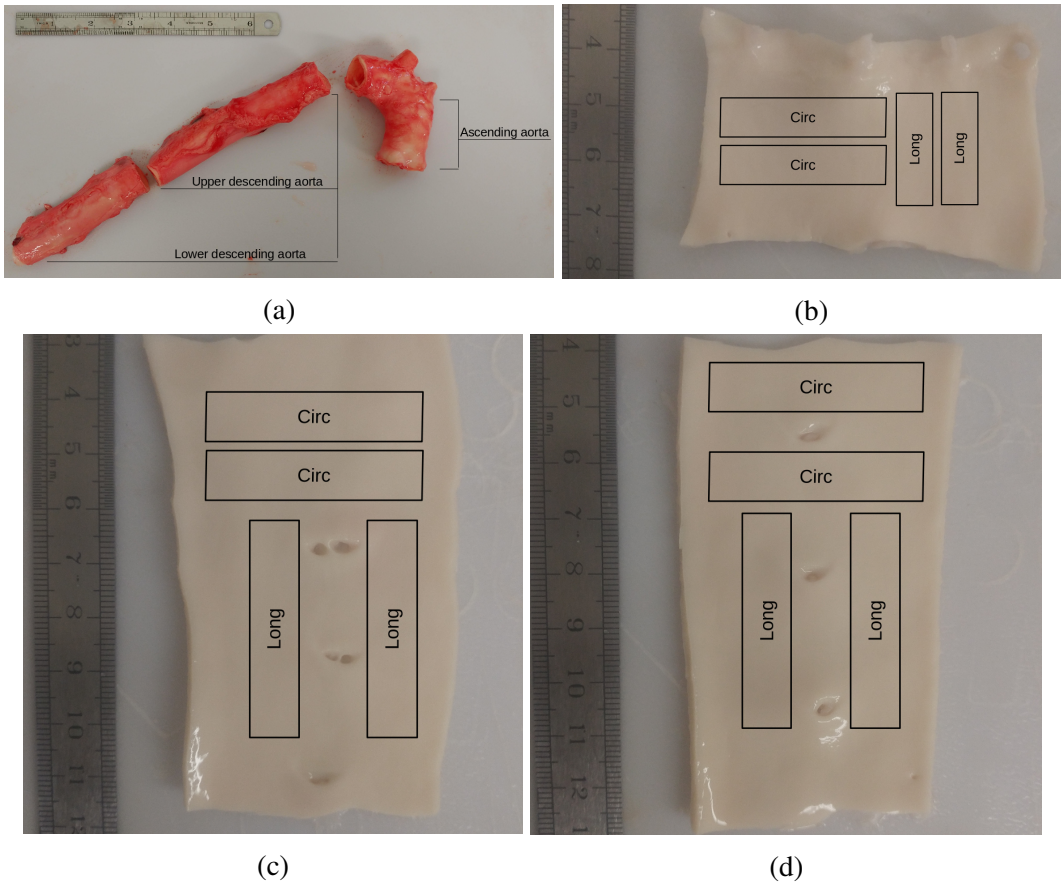

Figure 2.1: Schematic of the location of peel and uniaxial samples in individual segments (a) Aorta separated into ascending, upper descending and lower descending segments (b) Ascending aorta (c) Upper descending aorta (d) Lower descending aorta. The top of each picture represents a location closest to heart in each segment.

2.2.1 Peel Tests

Sample Preparation:

A small incision ($\sim$ 1-2mm) was created in the rectangular samples parallel to the intimal layer using a scalpel. This incision was extended length-wise to create a tear by manually applying force using a forceps until a desired tear length was obtained (approx. 8-12mm). This resulted in two halves of nearly equal thickness, one containing the intima and the inner-media and the other containing the outer media and the adventitia. Images of the sample were taken from the top and the side with the intimal layer facing down. These images were used for measuring the dimensions of the specimen. Width and thickness data for the peel specimens are given in table 2.1. Accuracy of the measurement is about $\pm$0.15mm. The length of the specimens varied between the segments and for different aortas due to the size of the available tissue.

Table 2.1: Width and thickness of the circumferential(circ) and longitudinal(long) peel specimens

Dimension (mm)	Asc-circ	Asc-long	Udes-circ	Udes-long	Ldes-circ	Ldes-long
Width	7.9 ± 1.2	9.4 ± 1.6	10.1 ± 1.6	9.4 ± 1.6	8.7 ± 0.3	9.3 ± 1.2
Thickness	3.1 ± 0.3	3.2 ± 0.4	2.7 ± 0.5	2.5 ± 0.3	2.0 ± 0.3	2.3 ± 0.5

2.2.1.1 Experimental Protocol:

Equal number of black glass microspheres (American Crafts- POP! microbeads-27352) of diameter $\sim 500\mu m$ were attached at regular intervals close to the edge of the specimen along its length on the intimal and the adventitial sides using cyanoacrylate super glue (5-8 on each side). The specimen was then mounted onto a biaxial machine. The clamps were displaced away from each other at a rate of 10mm/min to extend the tear. One of the previous studies reported negligible differences in the peeling characteristics when the test was conducted at a displacement rate of 1-10mm/min[84]. Therefore, a displacement rate of 10mm/min was chosen in order to minimize the time the tissue remains unhydrated. Force and displacement data were recorded every 0.1s.

A mirror oriented at 45° with the vertical axis was placed on the side. Reflected images of the specimen were captured during the experiment using a camera mounted above the mirror. Images were acquired at 0.6s interval. There is negligible distortion in the images due to reflection. These images were used for the measurement of stretch in the peeled specimen during the test.

The average thickness of the thicker peeled half was measured after the experiment using imaging and the thickness of the other half was calculated by subtracting this value from the average thickness of the whole specimen.

2.2.1.2 Stretch measurement:

Centroids of the markers are extracted from the images using MATLAB image processing toolbox. For details regarding the marker tracking and the MATLAB program associated with it, refer to [85]. A brief description of the steps involved in locating the centroids of the markers are given in table 2.2.

Table 2.2: Algorithm for the image processing program and the MATLAB functions used

1. Read the image acquired during the experiment
2. Convert the image to binary scale, crop the region of interest and specify the threshold value between 0-1 to detect the markers: *imbinarize()*
3. Use area filter to remove extraneous objects: *bwareafilt()*
4. Erode and dilate the image to fill the small holes in the image of the markers: *imerode()* and *imdilate()*
5. Locate the centroids of the markers: *regionprops()*
6. Measure the Euclidean distance between the adjacent markers and divide by the corresponding distance in first image to compute the stretch value: *pdist()*

Figure 2.2a shows an image of a specimen taken during the test and figure 2.2b shows the same image after the image filters are applied and the centroids of the markers superimposed onto the image. A pair of markers next to each other is called a marker set. The initial distance between two markers in each marker set was measured from the image taken at the start of the test. Similarly, distance between the markers in each marker set was calculated in each image taken during the test. Since the tissue between the markers is nearly straight in the initial and the peeled configurations, the stretch is measured as the ratio of the distance between the markers in a marker set in the current image and the initial image.

Figure 2.2c depicts the typical variation of the ratio of the current distance to the initial distance between two markers in a marker set during a peel test. The ratio is initially 1 and as the markers take a 90° turn near the tear tip, the distance between them decreases and hence the ratio decreases.

As the markers move away from the tear tip, the ratio of the current distance to the initial distance reaches a near constant value. Small oscillations in the ratio of the current distance to the initial distance is due to the slight movement of the peel specimen towards and away from the mirror during the experiment. The region between the markers reaches a near uniaxial state of stress at a certain distance beyond the tear tip. Based on this observation, a rectangular region spread symmetrically about the tear tip (approximately 2.5mm on each side from the tear tip) is defined such that the torn tissue is under uniaxial state of stress beyond this region. We call this the *tear propagation zone* and stretch experienced by the peeled tissue between two markers in a marker set is reported only when the marker set under consideration crosses this tear propagation zone.

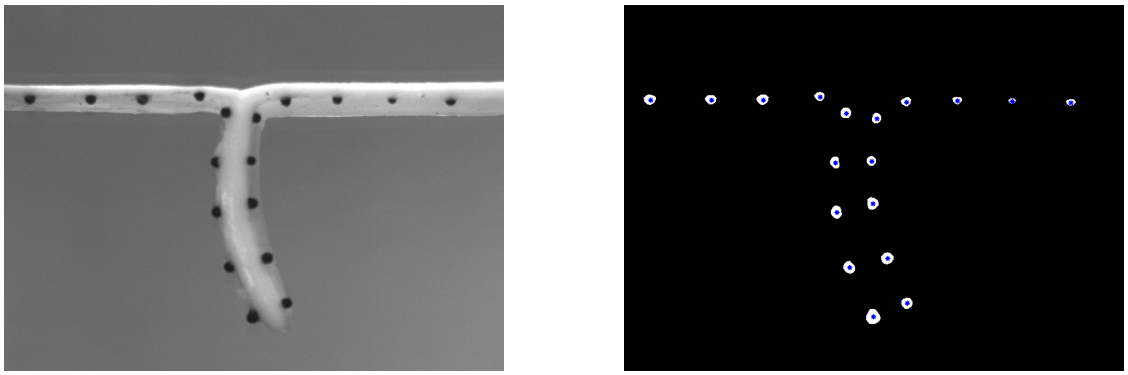

(a) (b)

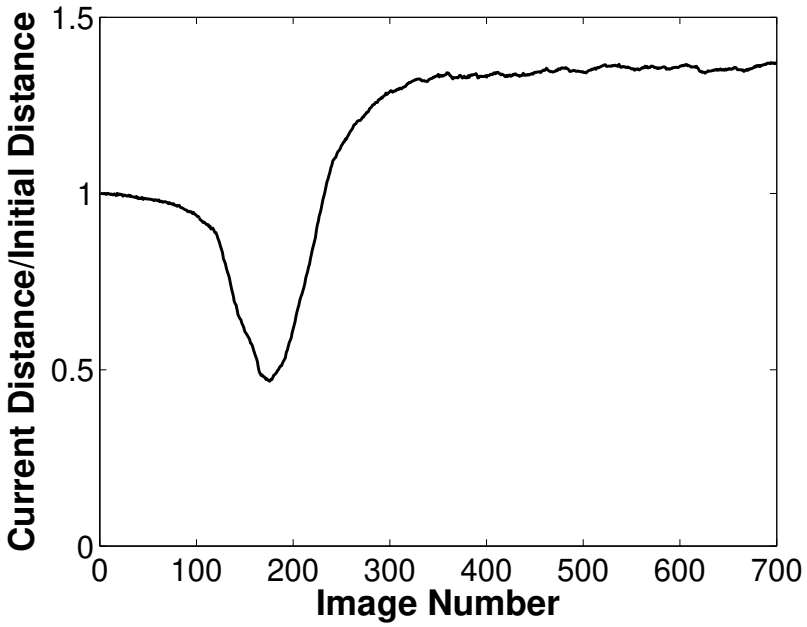

(c)

Figure 2.2: (a) Image acquired during the experiment (b) Image processed using the MATLAB program (Centroids of the markers are superposed on the markers themselves) (c) Ratio of the current distance to the initial distance between a marker set during the experiment.

Figure 2.3 shows a sequence of images with the image number and the ratio of current distance to initial distance between markers 2 and 3 on the left peeled half. Ratio remains near 1 when the markers are away from the tear. As the tear propagates and marker 2 approaches the tear tip (figure 2.3b), the ratio starts decreasing and reaches a minimum value (0.47 in this case, figure 2.3c) when

the tear tip is nearly half way between markers 2 and 3. As the tear propagates further and marker 3 reaches the tear tip, the ratio reaches 1 (figure 2.3d). the ratio of current distance to initial distance starts increasing from this point until it reaches a near constant value (~ 1.36). Figure 2.3e shows an image when the portion of the tissue between marker 2 and 3 becomes horizontal and straight. This is when the marker set is considered to have crossed the tear propagation zone.

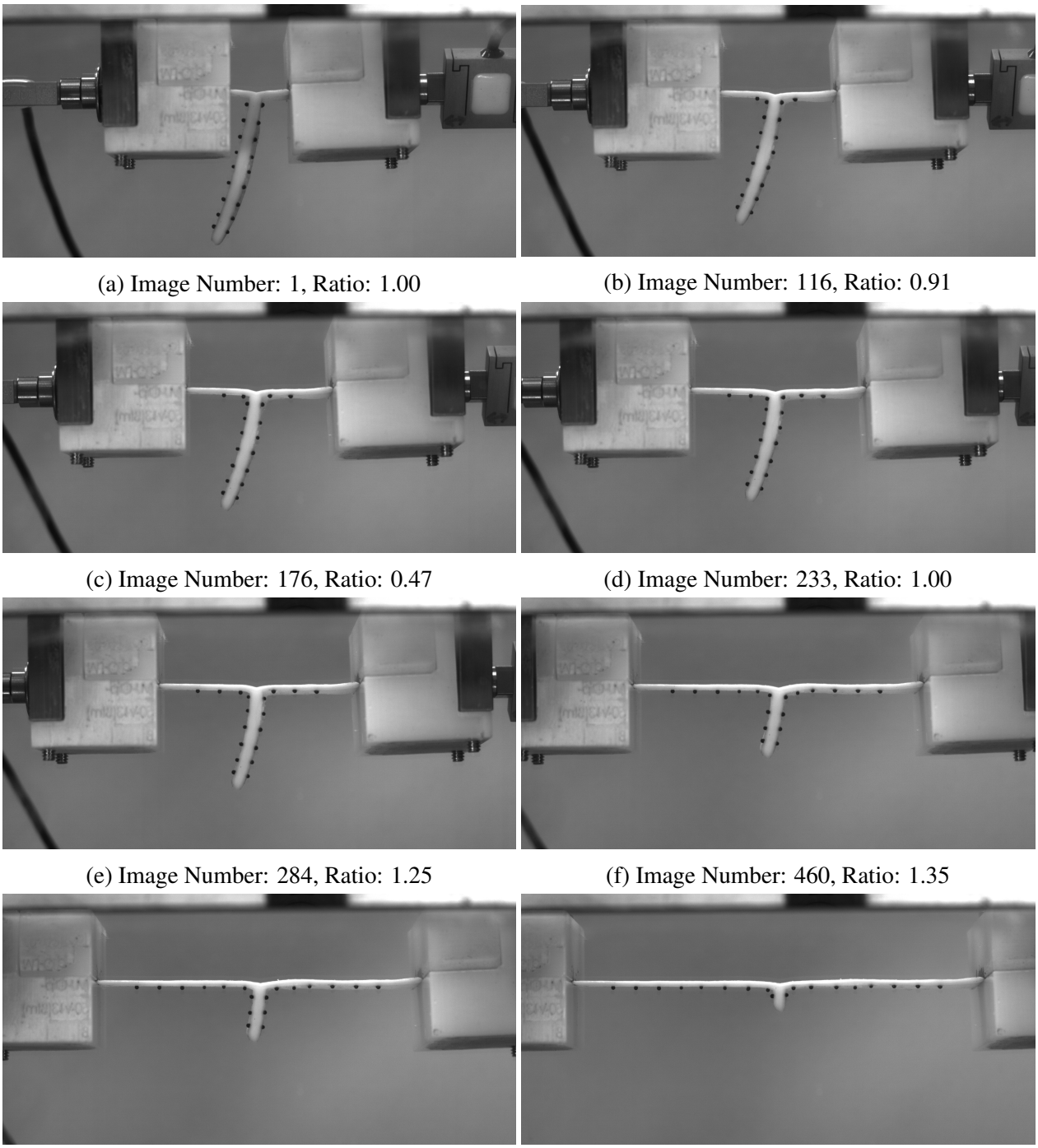

(a) Image Number: 1, Ratio: 1.00

(b) Image Number: 116, Ratio: 0.91

(c) Image Number: 176, Ratio: 0.47

(d) Image Number: 233, Ratio: 1.00

(e) Image Number: 284, Ratio: 1.25

(f) Image Number: 460, Ratio: 1.35

(g) Image Number: 530, Ratio: 1.36

(h) Image Number: 700, Ratio: 1.37

Figure 2.3: Sequence of images with image number and the ratio of current distance to initial distance between markers 2 and 3 (i.e. marker set 2) on the left peeled half(intimal half) during the experiment. Marker 1 refers to marker closest to the tear tip in image 1.

Tear length measurement: Tear length was computed at the end of the test based on the mean stretches of the intimal and the adventitial halves and the distance moved by the clamps during the experiment. If S_0 and S_1 are the distances between the clamps when the first marker and last marker on the intimal or the adventitial halves cross the tear tip respectively, and λ_i and λ_a are the mean stretches of the intimal and the adventitial halves respectively when the last marker crosses the tear tip, tear length is computed using eq. 2.1

$$C = \frac{S_1 - S_0}{\lambda_i + \lambda_a} \tag{2.1}$$

This procedure is illustrated in figures 2.4a & 2.4b.

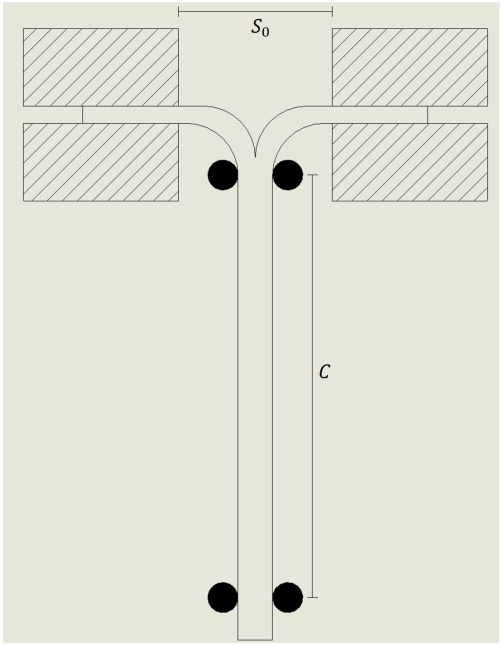

(a)

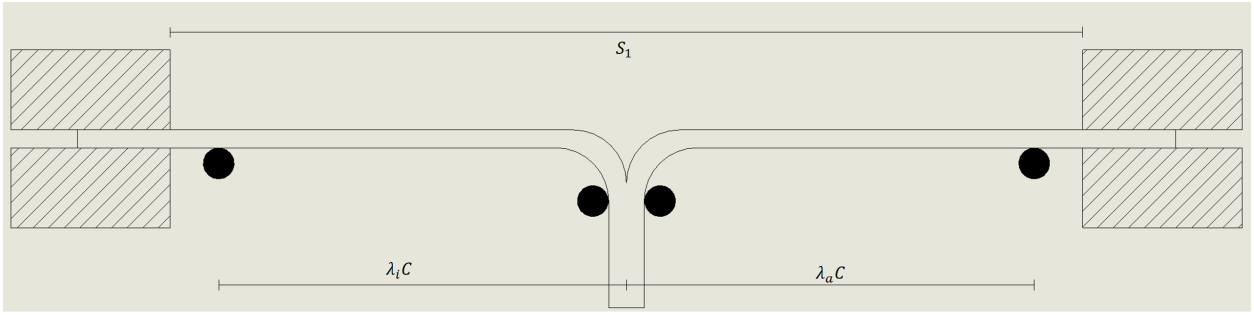

(b)

Figure 2.4: (a) shows the schematic of the peel sample when the first marker on the adventitial or intimal side is at the tear tip (b) shows the schematic of the peel sample when the last marker on the adventitial or intimal side is at the tear tip. Mean stretches are computed in the final image and tear length is calculated using equation 2.1

2.2.2 Uniaxial tests

Width and thickness data of the uniaxial specimens is given in table 2.3.

Table 2.3: Width and thickness of the uniaxial specimens

Dimension (mm)	Asc-circ	Asc-long	Udes-circ	Udes-long	Ldes-circ	Ldes-long
Width	8.3 ± 0.9	8.6 ± 0.9	9.7 ± 1.2	9.5 ± 1.0	9.0 ± 0.5	9.1 ± 0.9
Thickness	3.0 ± 0.2	3.0 ± 0.4	2.6 ± 0.4	2.7 ± 0.4	2.0 ± 0.4	2.2 ± 0.4

Glass markers were attached to the specimen using cyanoacrylate creating a 4x4 grid and 9 quadrilateral "cells" on the specimen. An image of a specimen during the uniaxial test is shown in figure 2.5. The specimen was then clamped onto the biaxial machine. A preload of $\approx$0.05N was applied to straighten the specimen. Clamps were displaced at a relative speed of 5mm/min to mimic the displacement rate undergone by each half of the peel specimen during the peel test. Preconditioning was not performed on the samples, inline with the protocol used for the peel tests. Specimens were elongated until complete rupture is achieved. Since the specimens are rectangular, failure often occurred near the clamps. Force and displacement data were recorded for every 0.1s. The force and displacement data after the start of the failure were discarded. Images were acquired from the top of the specimen at 1s interval. Load corresponding to each image was calculated to be the mean of the load values at the current time and the load values at $\pm$0.1s from current time. This was done to eliminate the possibility of error associated with the any time lag between image and load data. Thus, stress-stretch data is available at every 1s interval.

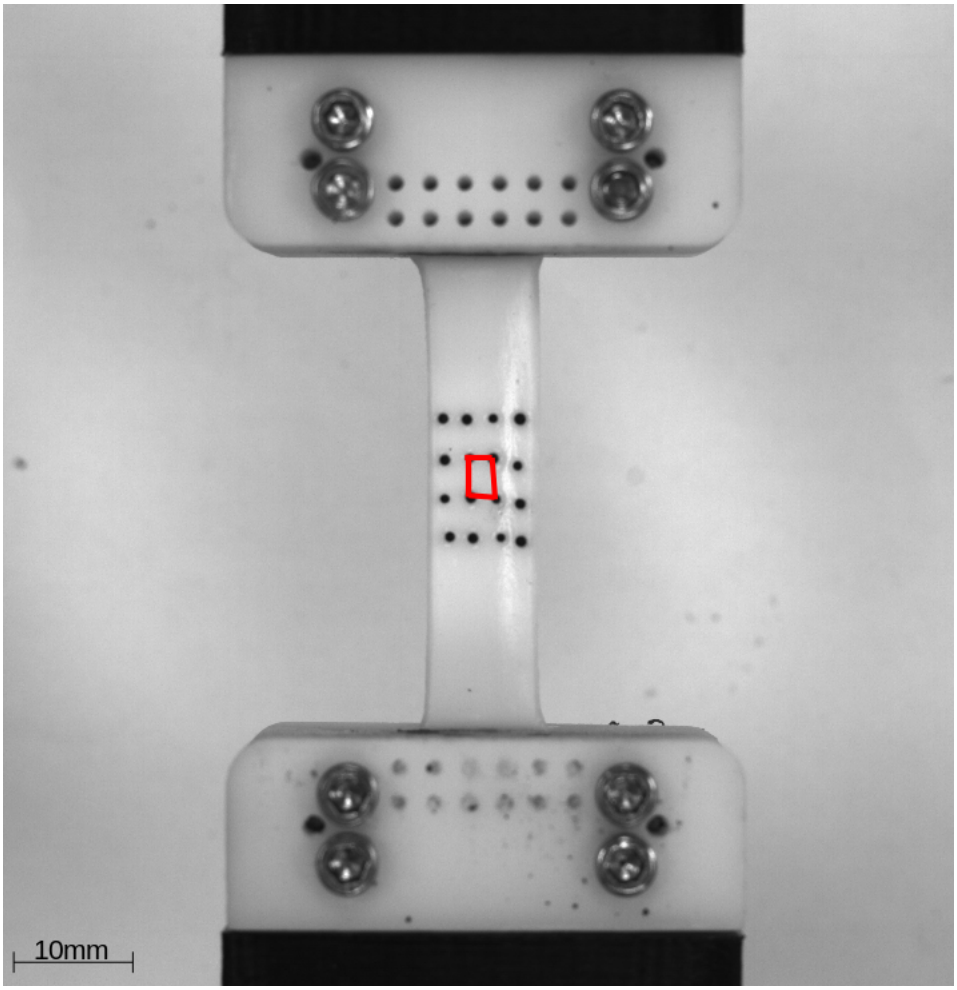

Figure 2.5: Image of a uniaxial sample taken during the test. A cell used for calculating the deformation gradient is shown in red color

Data analysis: Centroids of the glass markers are extracted from the images using a MATLAB program similar to the one used for peel tests. Since each cell may not be a perfect rectangle, the following transformation is used for the position coordinates to ensure displacement continuity between the cells

$$x = x_1\frac{(1-\xi)(1-\eta)}{4} + x_2\frac{(1+\xi)(1-\eta)}{4} + x_3\frac{(1+\xi)(1+\eta)}{4} + x_4\frac{(1-\xi)(1+\eta)}{4} \tag{2.2a}$$

$$y = y_1\frac{(1-\xi)(1-\eta)}{4} + y_2\frac{(1+\xi)(1-\eta)}{4} + y_3\frac{(1+\xi)(1+\eta)}{4} + y_4\frac{(1-\xi)(1+\eta)}{4} \tag{2.2b}$$

where (x, y) is the coordinate of a point within the cell in the current image and $(x_i, y_i), i = 1, .., 4$ are the position coordinates of the markers at the vertices of the cell in the current image. Jacobian of the transformation is defined to be

$$\mathbf{J} = \begin{bmatrix} \frac{\partial x}{\partial \xi} & \frac{\partial x}{\partial \eta} \\ \frac{\partial y}{\partial \xi} & \frac{\partial y}{\partial \eta} \end{bmatrix} \tag{2.3}$$

The deformation gradient is then calculated using equations 2.4 & 2.5

$$\underbrace{\begin{bmatrix} \frac{\partial x}{\partial \xi} & \frac{\partial x}{\partial \eta} \\ \frac{\partial y}{\partial \xi} & \frac{\partial y}{\partial \eta} \end{bmatrix}}_{\mathbf{J}} = \underbrace{\begin{bmatrix} \frac{\partial x}{\partial X} & \frac{\partial x}{\partial Y} \\ \frac{\partial y}{\partial X} & \frac{\partial y}{\partial Y} \end{bmatrix}}_{\mathbf{F}} \underbrace{\begin{bmatrix} \frac{\partial X}{\partial \xi} & \frac{\partial X}{\partial \eta} \\ \frac{\partial Y}{\partial \xi} & \frac{\partial Y}{\partial \eta} \end{bmatrix}}_{\mathbf{J}_0} \tag{2.4}$$

$$\mathbf{F} = \mathbf{J}\mathbf{J}_0^{-1} \tag{2.5}$$

The deformation gradient for the uniaxial test is taken as the average deformation gradient of the three adjacent cells at the center of the grid. The first Piola-Kirchhoff stress is computed using the load, and the undeformed cross-sectional area calculated from the width and thickness measured from the images taken before the experiment . Eq. 2.6 is used for fitting the first Piola-Kirchhoff stress-stretch data , where α and β are the fitting parameters

$$P = \frac{\alpha}{\beta}\left(e^{\beta(\lambda-1)} - 1\right) \tag{2.6}$$

Curve fitting of the data was performed using MATLAB's *fit* function using Trust-Region algorithm, and goodness of the fit was determined using the r^2 values. The first Piola-Kirchhoff stress-

stretch data acquired at 1s interval until 10 sec before the start of visible failure was used for curve fitting. Failure of the specimen often occurred between 3-6 minutes after the start of the test due to the differences in the stretch values between the specimens at which the failure occurred near the clamps. Therefore, 180-350 points were used for curve fitting depending on the specimen. Note that α and β are not the material constants associated with the aorta; they are only the fitting parameters associated with the uniaxial stress-stretch data for a particular test. Figure 2.6 shows representative plots for the data from the uniaxial tests on aorta 5 and the fits achieved using eq. 2.6. Full data set used for curve fitting are shown in figure 2.6.

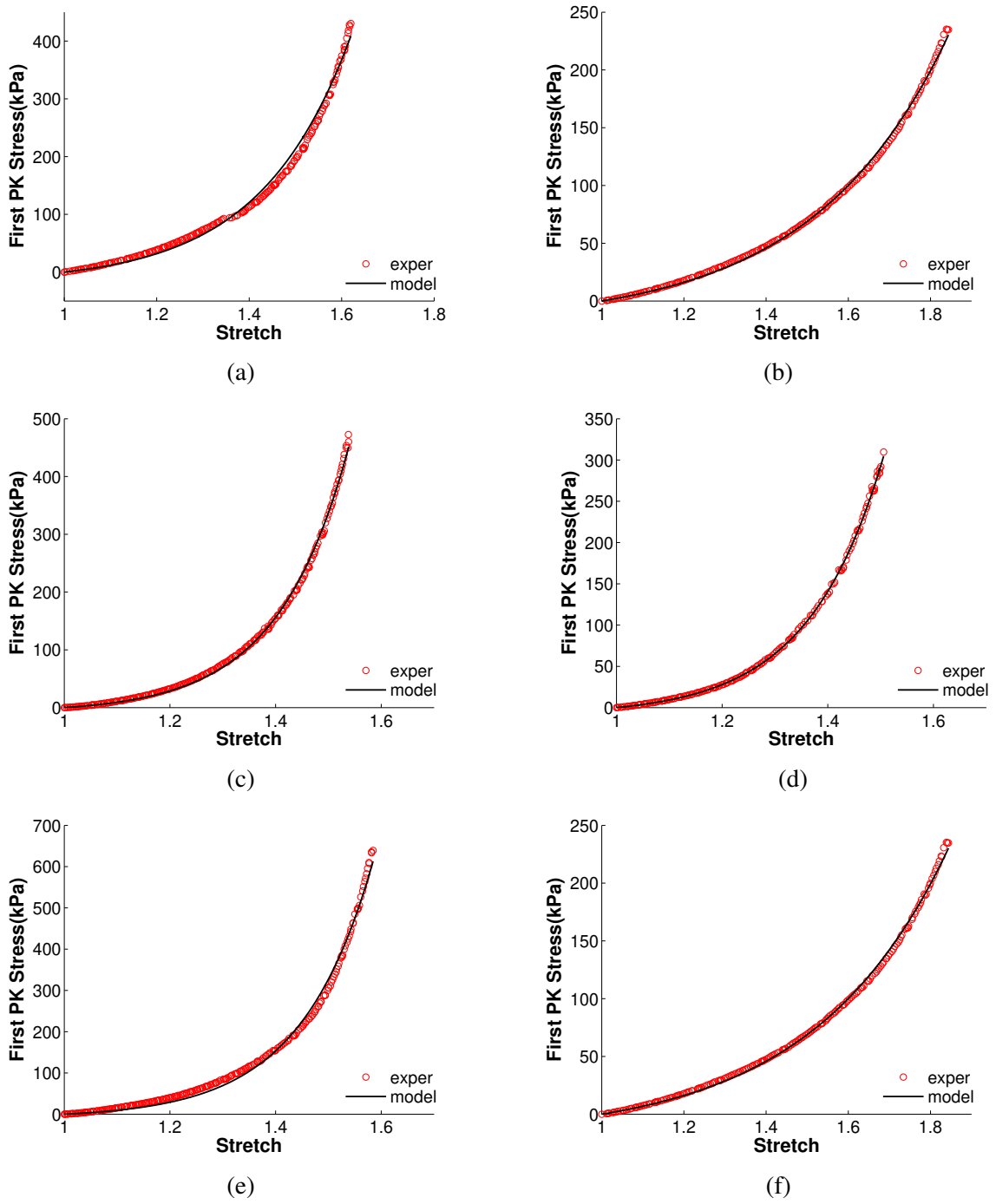

Figure 2.6: Representative plots (aorta 5) of the experimental data for (a) Ascending aorta-Circumferential (b) Ascending aorta- Longitudinal (c) Upper descending aorta-Circumferential (d) Upper descending aorta- Longitudinal (e) Lower descending aorta-Circumferential (f) Lower descending aorta- Longitudinal. The fit achieved using eq. 2.6 is shown as a continuous line

Table 2.4: r^2 values for the fits obtained using equation 2.6 for uniaxial specimens

Sample No.	Ascending		Upper Descending		Lower Descending	
	circ	long	circ	long	circ	long
1	0.998	0.999	0.999	0.997	0.997	0.998
2	0.998	0.997	0.996	0.992	0.998	0.996
3	0.999	0.996	0.999	0.998	0.998	0.988
4	0.994	0.998	0.997	0.995	0.995	0.997
5	0.991	0.998	0.998	0.999	0.994	0.998
6	0.998	0.996	0.996	0.998	0.992	0.992
7	0.999	0.991	0.995	0.997	0.987	0.998
8	0.998	0.998	0.998	0.993	0.996	0.999
9	0.998	0.998	0.996	0.998	0.994	0.990
10	0.994	0.999	0.996	0.998	0.993	0.994
11	0.991	0.991	0.999	0.996	0.995	0.992

Arteries are known to be viscoelastic and compressible, however, they are generally treated to be nearly elastic and incompressible[22]. Following this assumption and using the values of α and β obtained from the stress-stretch fit, the stored energy per unit volume (ψ) is computed as a function of stretch using eq. 2.7

$$\psi = \int_1^{\lambda} P d\lambda = \frac{\alpha}{\beta}\left((e^{\beta(\lambda-1)} - 1)/\beta - (\lambda - 1)\right) \tag{2.7}$$

2.2.3 Peeling Energy Calculation

Peeling energy is defined as the energy dissipated in the creation of a tear. Based on the assumption that arteries are nearly elastic, we assume that the energy dissipation due to the viscoelastic nature of the aorta is negligible compared to the stored energy and the energy lost in tearing during

the peel test. The work done by the external force during the peel experiment is thus partially stored as internal energy in the peel specimen and is partially dissipated in the creation of the new tear surfaces. Eq. 2.8 represents the energy balance used for the calculation of the peeling energy

$$\underbrace{\int_{S_0}^{S_1} F ds}_{\text{External work done}(W_{ext})} = \underbrace{\int_V \psi dV}_{\text{Stored energy}(W_{int})} + \underbrace{\int_A T dA}_{\text{Energy lost in peeling}} \tag{2.8}$$

where F is the force required for extending the tear or the peel force, $S_1 - S_0$ is the clamp displacement during the test, ψ is the stored energy per unit volume in the peeled tissue, V is the undeformed volume of the peeled tissue, T is the peeling energy per unit area, and A is the undeformed area of the surface exposed by the newly created tear (Symbol T is used because peeling is a process of tearing). Peeled halves are nearly under a state of uniaxial tension at the end of the test. Since peeled samples are rectangular with a constant width, Eq. 2.8 can be modified as

$$\int_{S_0}^{S_1} F ds = w \left(\int_0^C \psi(\lambda) t dc + \int_0^C T dc \right) \tag{2.9}$$

where C is the tear length(refer to figure 2.1) and w is the width of the specimen. The external work done in tearing, stored energy and peeling energy are calculated for the portion of the tissue between the first and the last markers. Two methods are used for the estimation of the mean peeling energy per unit area. The first method is similar to the one adopted by Sommer et al.[39], where the internal stored energy is calculated using a linear relation between the first Piola-Kirchhoff stress and the stretch. Using this method, mean peeling energy per unit area is calculated using eq. 2.10

$$T_{avg}^L = \left(\frac{F_{avg}}{w}(S_1 - S_0) - \frac{1}{2}\frac{F_{avg}}{w}(S_1 - S_0 - 2C) \right) / C \tag{2.10}$$

During the tear propagation, the force required for extending the tear reaches a plateau region where it shows an oscillatory behavior with peaks and valleys. F_{avg} is the average force in the plateau region.

In the second method, the mean peeling energy per unit area is calculated using eq. 2.11

$$T_{avg}^{NL} = \left(\frac{F_{avg}}{w}(S_1 - S_0) - C(t_i\psi(\lambda_i) + t_a\psi(\lambda_a)) \right) / C \tag{2.11}$$

where t_i and t_a are the mean thicknesses of the intimal and the adventitial halves respectively, C is the tear length, λ_i and λ_a are the mean stretches experienced by the intimal and the adventitial halves when the last marker crosses the tear tip. ψ is estimated using the fitting parameters obtained from the uniaxial test on the specimen oriented in the same direction as the peel specimen (i.e. if the peel specimen is a circumferentially oriented specimen, data from the uniaxial test on the circumferentially oriented specimen are used for the calculation of the stored energy per unit volume) and the stretch values measured during the peeling experiment.

2.3 Results

2.3.1 Uniaxial tests

Figure 2.7 depicts the variation of the first Piola-Kirchhoff stress with respect to stretch for the aortic specimens subjected to uniaxial state of stress. Pronounced anisotropy can be observed in all the segments with the circumferential direction being generally stiffer than the longitudinal direction for stretches larger than 1.2. Circumferential specimens from the descending aorta are stiffer compared to that of the ascending aorta for stretches greater than 1.2. However, no significant difference can be observed between the samples from the upper descending and the lower descending segments of the aorta. All the three segments demonstrate non-linear behavior with an initially softer and an increasingly stiffer response. The non-linearity is milder (lower rate of stiffness increase) in the specimens from the ascending segment compared to the descending segment. Tables 2.5 and 2.6 show the fitting parameters α and β for the circumferential and the longitudinal specimens from different segments of the aorta ($r^2 > 0.98$).

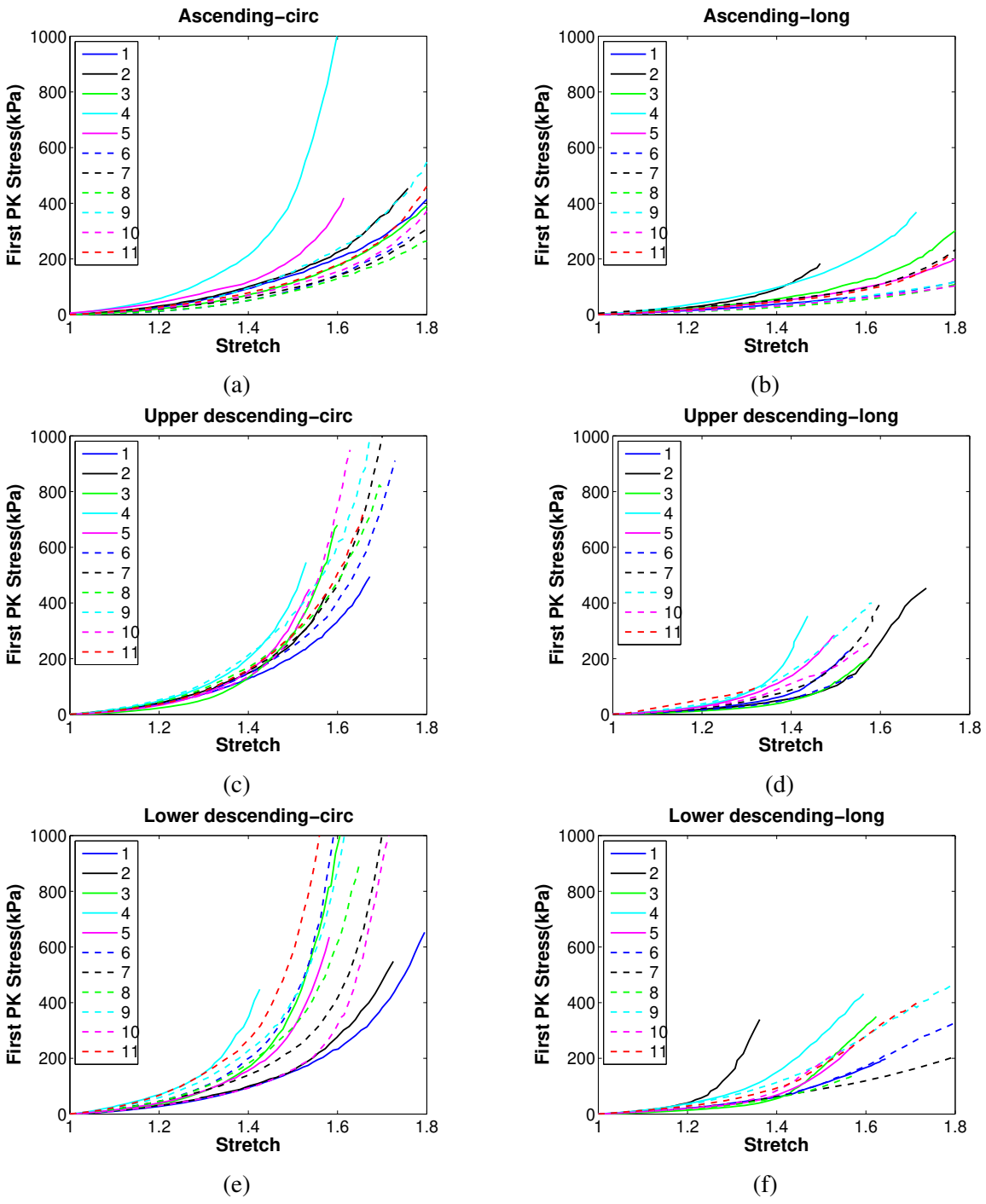

Figure 2.7: First Piola-Kirchhoff stress vs. stretch for different segments of the aorta (a) Ascending aorta-Circumferential (b) Ascending aorta- Longitudinal (c) Upper descending aorta-Circumferential (d) Upper descending aorta- Longitudinal (e) Lower descending aorta-Circumferential (f) Lower descending aorta- Longitudinal

Table 2.5: Fitting parameters α(kPa) and β for the uniaxial tests on circumferential specimens(r^2>0.98)

Sample No.	Ascending		Upper Descending		Lower Descending	
	α (kPa)	β	α (kPa)	β	α (kPa)	β
1	107.68	3.26	110.09	4.51	72.91	4.68
2	98.21	3.86	103.28	5.43	73.03	5.01
3	72.60	3.89	39.50	8.30	42.71	8.82
4	83.17	7.47	95.11	6.92	127.70	7.80
5	91.63	5.11	62.93	7.42	64.09	7.29
6	50.78	4.21	89.48	5.50	41.66	9.10
7	65.99	3.60	65.60	6.58	46.78	7.10
8	60.47	3.50	124.06	5.07	89.69	6.37
9	91.88	4.03	115.39	5.85	67.90	7.78
10	56.55	4.21	34.53	8.72	16.45	8.76
11	33.80	5.51	106.92	5.53	94.45	7.91

Table 2.6: Fitting parameters α(kPa) and β for the uniaxial tests on longitudinal specimens(r^2>0.98)

Sample No.	Ascending		Upper Descending		Lower Descending	
	α (kPa)	β	α (kPa)	β	α (kPa)	β
1	61.03	1.94	30.25	7.69	65.61	4.02
2	59.64	5.84	26.26	6.99	49.50	12.29
3	54.88	3.82	19.00	7.73	31.44	7.17
4	109.02	3.53	31.47	11.03	115.36	5.13
5	58.99	3.02	63.83	7.00	32.65	6.98
6	34.62	3.12	36.99	5.80	89.28	3.26
7	47.45	3.65	36.62	7.26	107.44	1.89
8	28.68	3.28	-	-	52.80	4.44
9	61.41	1.86	122.70	4.95	176.54	2.67
10	48.03	2.19	85.52	4.75	44.80	6.61
11	45.32	3.57	213.59	1.81	106.61	3.96

2.3.2 Peel tests

The stretch response of the peel specimens varies from one specimen to another. Figure 2.8 portrays the typical stretch response (majority of the specimens) observed in the peeled halves of a peel specimen during the experiment (shown here is that of aorta 11). The stretch in the peeled tissue between different marker sets is plotted against the image number. Vertical lines in the figure represent the image number at which the marker set crossed the tear propagation zone. The intimal and the adventitial halves undergo similar stretches during the peel experiment.

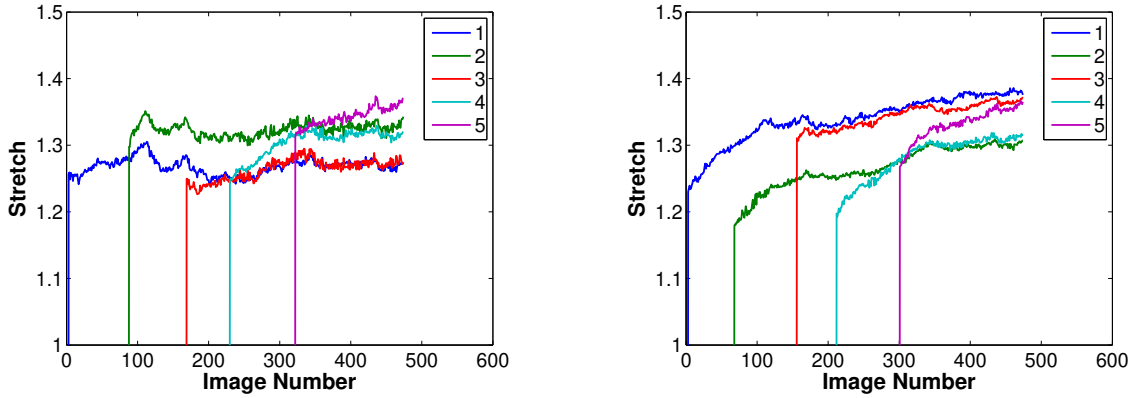

Figure 2.8: Stretch vs. image number for the (a) Intimal half and the (b) Adventitial half of the peeled specimen oriented in the circumferential direction taken from the lower descending segment of aorta sample 11.

There are some specimens that exhibit different response characteristics from the one described previously. Figures 2.9a, 2.9b shows the stretch behaviour of a sample (aorta 7) where the intimal half experiences a significantly different stretch compared to the adventitial half. Figures 2.9c, 2.9d displays the stretch behaviour in a longitudinal sample where the stretch values between adjacent marker sets differ significantly from each other in the adventitial half. In this sample, as the tear propagated, a small portion of the tissue along the tear surface remains attached to both the intimal and the adventitial halves. In order for the tear to propagate further, this portion of the tissue must be severed. Severing of the attached tissue created large increases in the peeling force which can be seen in the peel force per unit width behaviour of the longitudinal specimens depicted in figure 2.10. Figure 2.9e shows the severed tissue loosely hanging during the peel test.

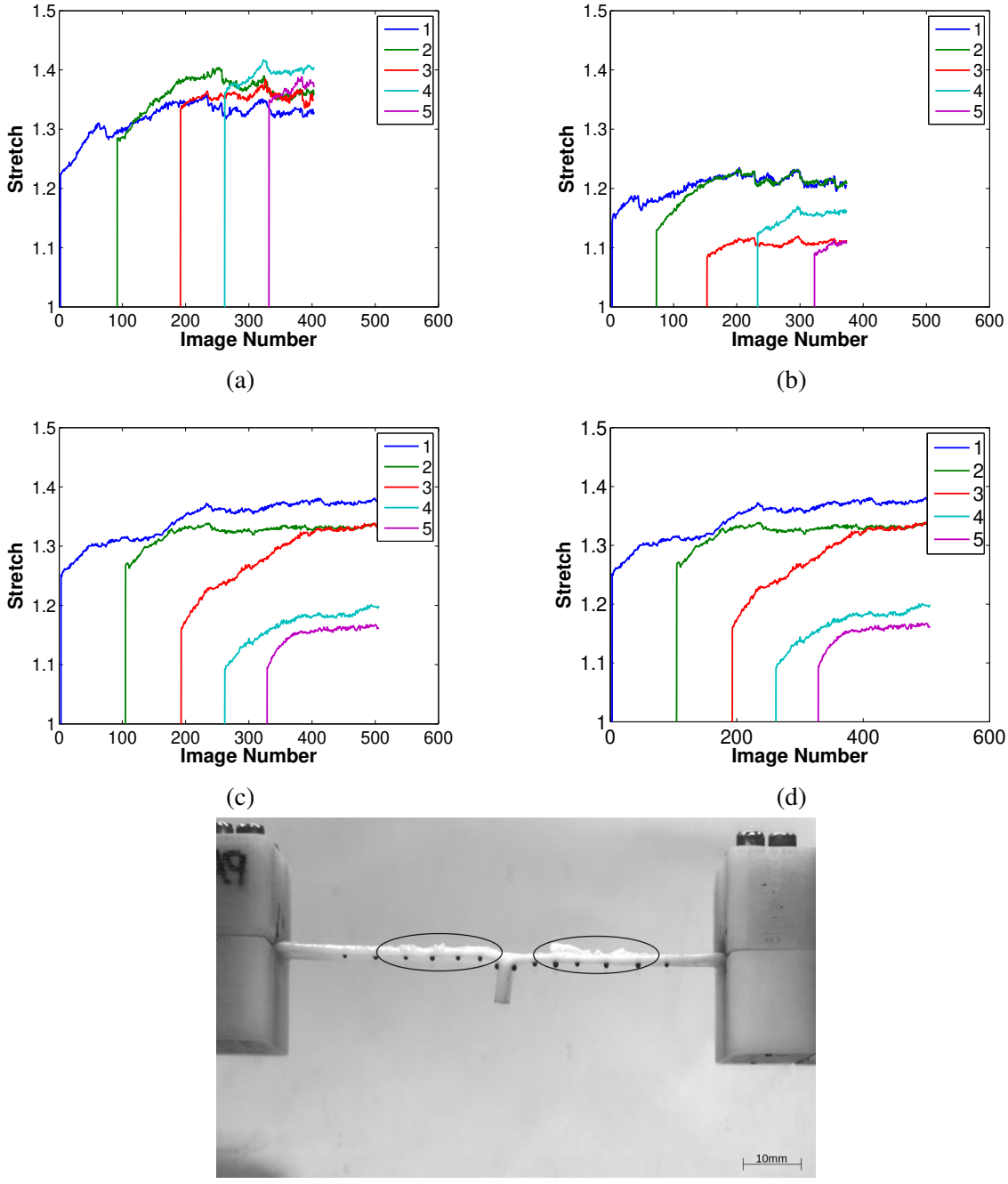

Figure 2.9: (a), (b) show stretch vs. image number for the intimal half and the adventitial half of the peeled specimen oriented in the circumferential direction taken from the upper descending segment of aorta sample 7. (c), (d) show stretch vs. image number for the intimal half and the adventitial half of the peeled specimen oriented in the longitudinal direction taken from the upper descending segment of aorta sample 10. (e) shows the tissue detachment occurred during the peel test.

Tables 2.7 and 2.8 provide the maximum and the average stretch, and the corresponding standard deviations(SD) in the peeled halves for the circumferential and the longitudinal specimens from different segments of the aorta at the end of the peel test. The maximum and average stretches are calculated from the stretch values of the marker sets that have crossed the tear propagation zone. The average of the mean intimal stretch and the mean adventitial stretch is calculated for each of the peel specimens, and a paired student t-test is conducted to evaluate the segmental and directional variation in the stretch behavior. Longitudinal peel specimens experience higher stretches than the circumferential peel specimens ($p<0.01$). While the stretch in the ascending aortic specimens is higher compared to that of the descending aortic specimens ($p<0.01$), no significant difference has been found between the upper descending and the lower descending segments of the aorta in circumferential and longitudinal directions ($p>0.05$). The stretch experienced by the longitudinal peel specimens has a larger standard deviation compared to the circumferential peel specimens in the ascending and the descending segments.

Table 2.7: Maximum and average stretches in the circumferential peel specimens

Sample No.	Ascending				Upper Descending				Lower Descending			
	Intima		Adventitia		Intima		Adventitia		Intima		Adventitia	
	Max	Avg	Max	Avg	Max	Avg	Max	Avg	Max	Avg	Max	Avg
1	1.41	1.37	1.77	1.50	-	-	-	-	1.36	1.32	1.26	1.20
2	1.51	1.41	1.48	1.36	1.32	1.30	1.27	1.24	1.26	1.23	1.14	1.09
3	1.58	1.30	1.25	1.24	1.29	1.15	1.28	1.23	1.31	1.27	1.33	1.17
4	1.39	1.35	1.37	1.24	1.26	1.15	1.21	1.17	1.29	1.25	1.21	1.17
5	1.45	1.39	1.29	1.26	1.36	1.33	1.43	1.29	1.37	1.26	1.13	1.10
6	1.56	1.51	1.39	1.32	1.26	1.25	1.44	1.35	1.40	1.32	1.39	1.30
7	-	-	-	-	1.40	1.36	1.21	1.15	1.38	1.33	1.37	1.31
8	1.38	1.35	1.51	1.35	1.36	1.28	1.22	1.16	1.34	1.30	1.25	1.18
9	1.37	1.31	1.47	1.37	1.32	1.23	1.13	1.10	1.26	1.24	1.20	1.24
10	1.48	1.41	1.30	1.29	1.20	1.19	1.22	1.14	1.31	1.27	1.39	1.30
11	1.38	1.32	1.36	1.32	1.42	1.40	1.23	1.22	1.38	1.32	1.37	1.33
Mean	1.45	1.37	1.42	1.33	1.32	1.26	1.26	1.21	1.33	1.28	1.28	1.22
SD	0.08	0.06	0.15	0.08	0.07	0.09	0.10	0.08	0.05	0.04	0.10	0.08

Table 2.8: Maximum and average stretches in the longitudinal peel specimens

Sample No.	Ascending				Upper Descending				Lower Descending			
	Intima		Adventitia		Intima		Adventitia		Intima		Adventitia	
	Max	Avg	Max	Avg	Max	Avg	Max	Avg	Max	Avg	Max	Avg
1	1.77	1.77	1.47	1.47	1.48	1.43	1.48	1.43	1.49	1.45	1.36	1.30
2	1.63	1.61	1.90	1.82	1.45	1.41	1.34	1.27	1.45	1.41	1.33	1.25
3	1.61	1.56	1.84	1.81	1.46	1.38	1.45	1.36	1.69	1.56	1.50	1.39
4	1.63	1.56	1.49	1.47	1.39	1.36	1.27	1.23	1.38	1.30	1.27	1.21
5	1.69	1.37	2.11	1.73	1.40	1.38	1.26	1.17	-	-	-	-
6	1.42	1.42	2.05	1.83	1.48	1.43	1.28	1.25	1.72	1.66	1.69	1.62
7	1.63	1.60	1.84	1.78	1.48	1.45	2.01	1.61	1.69	1.63	1.61	1.50
8	1.40	1.37	1.76	1.63	1.41	1.38	1.53	1.44	1.48	1.46	1.81	1.70
9	1.46	1.35	2.26	1.83	1.44	1.39	1.30	1.17	1.52	1.46	1.64	1.42
10	1.53	1.49	1.46	1.40	1.44	1.41	1.38	1.28	-	-	-	-
11	1.33	1.30	1.71	1.70	1.52	1.51	1.38	1.21	1.58	1.52	1.31	1.23
Mean	1.55	1.49	1.81	1.68	1.51	1.41	1.43	1.31	1.56	1.49	1.50	1.40
SD	0.14	0.14	0.27	0.16	0.04	0.04	0.21	0.14	0.12	0.11	0.19	0.18

The maximum and the mean stretch undergone by the circumferential peel specimens typically fall in the transition region from the low stiffness and the high stiffness portion of the uniaxial stress-stretch curve in the ascending as well as the descending segments of the aorta. For example, consider the stretch undergone by the intimal half of the circumferential specimen taken from the lower descending segment of the aorta sample 11. Maximum and mean stretch on the intimal half are 1.38 and 1.32 which fall in the transition region of the first Piola-Kirchhoff stress-stretch curve (red dashed line in figure 2.7e). In case of longitudinal specimens, the maximum stretches fall in

the stiffer region while the mean stretches fall in the transition region. This behaviour in longitudinal specimens may be attributed mainly to the severing of the tissue during tear propagation.

Figure 2.10 portrays the peel force per unit width during the experiment for all the specimens from different segments of the aorta. Similar to the stretches in the peel samples, higher standard deviation can be observed in the peel force per unit width in the longitudinal direction compared to the circumferential direction. Table 2.9 shows the mean peel force per unit width for the circumferential samples from different segments of the aorta and the corresponding standard deviations. The average and the standard deviation for each specimen are calculated from the plateau region of the force-displacement data (data shown in figure 2.10 are used for calculating the mean and standard deviation). Mean and standard deviation shown at the bottom of the table are calculated using the mean values across the aortas. Table 2.10 shows the peel per unit width data for the longitudinal specimens. Ascending circumferential specimens have a higher peel force per unit width compared to the descending aortic specimens ($p<0.01$). While no significant difference ($p>0.05$) has been found between the longitudinal specimens from different segments of the aorta, mean peel force per unit width in the ascending segment is higher compared to that for the descending segment. There is no significant difference in the peel force per unit width between upper descending and lower descending segments of the aorta ($p>0.05$) in the circumferential as well as the longitudinal directions.

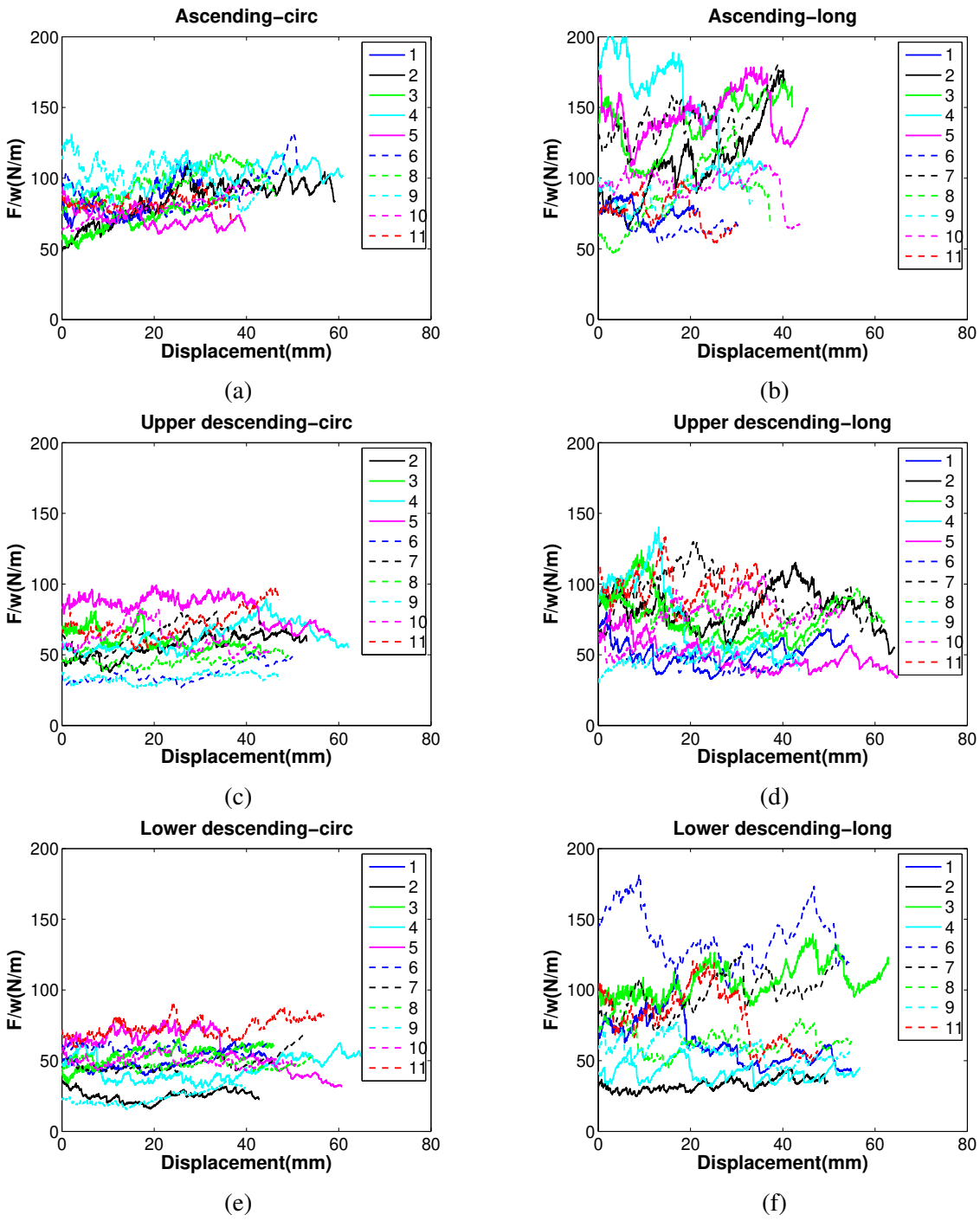

Figure 2.10: Peel force per unit width of the specimens from different segments (a) Ascending aorta-Circumferential (b) Ascending aorta-longitudinal (c) Upper descending aorta-Circumferential (d) Upper descending aorta-longitudinal(e) Lower descending aorta-Circumferential (f) Lower descending aorta-longitudinal

Table 2.9: Peel force per unit width(N/m) in the circumferential specimens

Sample No.	Ascending	Upper Descending	Lower Descending
1	84.5 ± 12.3	-	49.5 ± 6.1
2	84.6 ± 14.0	56.2 ± 7.9	25.2 ± 4.1
3	71.6 ± 9.9	60.2 ± 7.0	53.6 ± 6.8
4	100.9 ± 9.0	62.7 ± 9.7	44.4 ± 8.4
5	71.6 ± 6.3	83.1 ± 9.3	58.2 ± 13.4
6	86.9 ± 13.8	37.1 ± 6.2	57.6 ± 3.5
7	-	64.0 ± 9.4	48.6 ± 6.1
8	96.5 ± 11.0	46.1 ± 3.8	47.9 ± 3.2
9	101.6 ± 11.6	33.4 ± 3.1	24.2 ± 5.2
10	79.9 ± 7.8	61.1 ± 8.7	49.9 ± 3.6
11	82.4 ± 4.7	71.2 ± 10.3	73.3 ± 6.2
Mean $\pm$ SD	86.0 ± 10.8	57.5 ± 15.1	48.4 ± 14.1

Table 2.10: Peel force per unit width(N/m) in the longitudinal specimens

Sample No.	Ascending	Upper Descending	Lower Descending
1	75.8 ± 6.7	51.0 ± 9.2	62.7 ± 16.0
2	109.9 ± 26.5	82.8 ± 13.4	32.9 ± 4.2
3	138.8 ± 19.2	74.4 ± 17.4	105.5 ± 12.0
4	150.6 ± 33.7	73.6 ± 27.2	41.4 ± 6.2
5	144.2 ± 15.5	49.1 ± 10.4	-
6	66.0 ± 6.8	46.7 ± 8.7	137.8 ± 18.3
7	142.5 ± 15.3	90.3 ± 16.1	96.9 ± 12.9
8	88.0 ± 23.2	77.3 ± 9.6	64.3 ± 9.2
9	90.7 ± 11.3	48.8 ± 6.2	56.7 ± 7.7
10	95.2 ± 10.3	76.9 ± 14.6	-
11	75.7 ± 11.4	96.5 ± 12.7	80.5 ± 19.2
Mean $\pm$ SD	107.0 ± 31.6	69.8 ± 17.9	75.4 ± 33.3

Tables 2.11 and 2.12 provide the peeling energy per unit area for the circumferential and the longitudinal specimens from different segments of the aorta calculated using a linear relation(L) between first Piola-Kirchhoff stress and stretch, and the non-linear relation(NL) obtained from the uniaxial experiments. The difference in T is not significant between the two methods. Therefore, using a linear relation between the first Piola-Kirchhoff stress and stretch for the calculation of internal energy during a peel experiment on the porcine aorta gives reasonably accurate values of peeling energy per unit area. Comparing the peeling energy per unit area, calculated using the linear assumption, between different segments of the aorta, ascending aortic circumferential specimens exhibit higher T compared to the descending segments ($p<0.01$). There is no significant difference between the specimens from the upper descending and the lower descending segments ($p>0.05$). The peeling energy per unit area of the longitudinal specimens from the three segments

of the aorta did not show a significant difference ($p>0.05$).

Table 2.11: Peeling energy per unit area(T) in J/m^2 for the circumferential samples

Sample No.	Ascending		Upper Descending		Lower Descending	
	L	NL	L	NL	L	NL
1	200.1	195.8	-	-	111.4	117.4
2	198.9	195.7	126.0	125.8	54.1	55.9
3	150.1	166.7	130.8	137.3	118.1	124.5
4	228.8	233.8	134.4	139.9	97.4	97.8
5	164.7	169.2	190.5	197.2	126.6	133.3
6	207.0	218.9	84.1	82.1	132.0	137.5
7	-	-	142.3	147.5	110.4	116.9
8	222.6	238.3	100.9	98.9	106.3	108.0
9	231.1	240.8	71.5	72.4	51.8	53.4
10	182.2	193.4	129.1	134.9	112.4	122.5
11	187.2	202.7	162.1	159.6	166.6	173.1
Mean	197.3	205.5	127.2	129.6	107.9	112.7
SD	26.9	26.8	35.2	37.2	32.7	34.6

Table 2.12: Peeling energy per unit area(T) in J/m^2 for the longitudinal samples

Sample No.	Ascending		Upper Descending		Lower Descending	
	L	NL	L	NL	L	NL
1	191.2	193.3	121.7	119.7	147.9	150.0
2	289.7	123.0	191.8	209.5	75.8	59.9
3	373.3	312.6	173.5	189.7	257.3	270.7
4	374.2	381.6	166.5	176.7	92.1	94.2
5	343.8	375.3	111.3	113.6	-	-
6	173.0	141.6	107.6	112.6	357.1	356.6
7	367.3	387.6	226.3	212.2	245.5	251.5
8	216.6	231.9	182.8	-	161.4	130.0
9	226.6	240.6	110.2	104.3	138.3	119.8
10	225.4	246.3	179.3	184.7	-	-
11	182.3	187.0	224.7	219.1	187.8	192.0
Mean	269.4	256.4	163.2	164.2	184.8	180.5
SD	81.78	95.36	44.33	46.39	88.88	95.83

2.4 Discussion

To the authors knowledge, none of the previous studies reported the stretch in the peel specimens during a peel test on human or animal aortas. However, some inferences can be drawn from some of the previous studies. Noble et al.[54] conducted peel tests on porcine thoracic aorta. Taking the mean displacement of the clamps at the end of the test (refer to the mean curve in "controls axial" and "controls circ" in figure 8 of [54]), mean stretch in the axial direction can be calculated as 1.36 and mean stretch in the circumferential direction is 1.24. However, Noble et al. have not reported if the tests were done on ascending or descending porcine aorta. These stretch values are similar to the stretches in the descending segment in our study. Som-

mer et al.[39] reported mean dissection energy during peeling experiments on human abdominal aorta media. Calculating the mean length(in m) of the specimens at the end of the test using $l_e = W_{ext}/(2(F/w))$ and the initial length of the specimen using $l_i = l_e - W_{int}/(F/w)$, we get mean stretch in the circumferential direction as $l_e/l_i = 0.037/0.030 = 1.23$ and in the longitudinal direction as $l_e/l_i = 0.029/0.025 = 1.16$. The mean stretch in the circumferential direction of the human abdominal aorta is similar to the stretches in the circumferential direction of the descending porcine aorta, while the stretch in the longitudinal direction is lower than the porcine thoracic aorta. However, note that the displacements at the end of the peel test for the longitudinal specimens in the study by Sommer et al. have a larger standard deviation compared to the circumferential specimens. Tong et al.[40] reported peeling experiments on human carotid arteries. Their stretch values ($\sim$1.10) seem to be lower than that for the porcine thoracic aorta and the human abdominal aorta. Our study as well as these previous studies clearly indicate a segmental variation in the stretches experienced by the peel specimens.

The peel force per unit width is found to be higher in the ascending aorta compared to the descending aorta. Mean peel force per unit width in the longitudinal direction is typically higher than the mean peel force per unit width in the the circumferential direction. This behaviour was previously observed in human and porcine aortas, and human carotid bifurcations ([39], [86], [52], [54], [87]). Resistance caused by the circumferentially oriented smooth muscle cells[39] and a higher number density of the "radially-running" fibers (interlamellar) in the longitudinal direction compared to the circumferential direction[88] of the aorta are reported to be the possible reasons for higher peel force per unit width in the longitudinal direction in the human aortas. Even though we haven't performed any histological analysis on the peeled tissue, the similarities in the lamellar organization of the aorta in porcine and humans[89] and significant local tearing of the tissue in the longitudinal peel specimens reflects the presence a tear propagation mechanism in the porcine aortas analogous to humans. Peel force per unit width in the porcine ascending aorta is lower than the reported values for aged, healthy human aortas[52] but is higher compared to the dissected ascending aortas[90] and the non-dissected ascending thoracic aortic aneurysms[53] from humans.

Significant tearing and severing of the internal tissue was observed during the peeling experiment on the longitudinal specimens (refer to figure 2.9e). As noted in the previous studies by Sommer et al.[39] and Tong et al.[40], tear propagation in the longitudinal specimens crosses the elastic laminae creating a "rougher" dissection surface. In this process some of the internal tissue tears and hangs loose from the peeled halves. Therefore, the peel force per width alone may not be a reasonable parameter for comparison of the directional properties. The thickness of the peeled halves is different from one another (i.e adventitial half versus intimal half) at the end of the experiment.Nevertheless, mean peel stress in the peeled halves can be calculated using the equation $\sigma_{peel} = \frac{2F_{avg}}{wt}$, where w and t are width and thickness of the specimen. In the circumferential direction, mean peel stresses are 54.8 $\pm$ 6.1 kPa, 43.1 $\pm$ 11.9 kPa and 49.5 $\pm$ 16.4 kPa respectively for the ascending, the upper descending and the lower descending segments of the aorta. Mean peel stresses in the longitudinal direction are 68.8 $\pm$ 26.8 kPa, 57.7 $\pm$ 16.8 kPa and 69.5 $\pm$ 26.9 kPa respectively for the the ascending, the upper descending and the lower descending segments of the aorta. In the longitudinal direction, mean peel stresses are highly correlated (p>0.2) in the three segments of the aorta. In fact, mean peel stress in the lower descending aorta is slightly higher than the ascending and the upper descending aorta which is not the case with peel force per unit width. Even in the circumferential direction, mean peel stresses have higher p-values showing a better correlation compared to the peel force per unit width. Using the same methodology for the data reported on human abdominal aortic media by Sommer et al.[39], we obtain mean peel stresses in the circumferential and longitudinal direction to be $\sim$40.8 kPa and $\sim$40.7 kPa respectively which are nearly the same as opposed to peel force per unit width. Mean peel stress appears to be a parameter that is better correlated between different segments and directions of the aorta.

The influence of non-linearity is found to be minor in the estimation of peeling energy per unit area. This can be attributed to two factors: 1) Mean stretch experienced by the peel specimens is in the transition region of the stress-stretch curve where non-linearity is mild, 2) Even though there is a considerable difference in the stored energy per unit volume (ψ) calculated using linear and the non-linear assumptions, total internal energy (ψwtC) stored in the specimen at the end of

the peel test is small ($\sim$10%) compared to the external work done which diminishes the effect of nonlinearity in the estimation of peeling energy per unit area. Peeling energy obtained in this study for the descending aorta ($\sim$129.6 J/m^2 in circ and $\sim$164.2 J/m^2) are lower than the peeling energy values for control specimens reported by Noble et al.[54] ($\sim$151.8 J/m^2 in circ and $\sim$183.3 J/m^2). Tong et al.[51] reported a 28% increase in the peel force per unit width when the displacement rate is changed from 1mm/min (rate used in [39]) to 1mm/sec (rate used in [54]). The higher peel force per unit width and the peeling energy reported by Noble et al.[54] is most likely due to the different displacement rate used in their study. However, the values of peeling energy of the porcine thoracic aorta are much higher compared to the peeling energy in human thoracic aorta [91], abdominal aorta[39], carotid artery [40], abdominal aneurysmal wall[51] and coronary arteries [55].

The effect of freezing on the peel properties has not been addressed here. A study by O'Leary et al.[92] found negligible differences in the biaxial mechanical properties of the fresh and the frozen porcine specimens up to a year from the harvest when stored at -20°C in isotonic saline solution. Therefore, we do not expect a significant difference in the peel properties between the fresh and the frozen porcine specimens.

Some limitations of the current study must be acknowledged. In certain cases of aortic dissection, the tear propagates into the abdominal aorta[93]. Peel properties of the abdominal aorta are not examined here as the main focus of this study has been the thoracic aorta, where aortic dissection typically initiates. Hydration and temperature may have discernible influence on the mechanical properties of the aorta ([94], [95]). The values of the peel properties presented in this study may differ when the specimens are tested in a tissue bath maintained at 37°C. In addition, the peel properties seem to differ with the circumferential region from which the specimens are obtained[53]. We did not distinguish between the regions within each segment when obtaining the specimens. Further, we haven't noticed any significant raise/drop in the peel force per unit width when testing individual circumferential specimens from the ascending aorta. It remains to be seen if porcine aortas also exhibit regional variation as the human aortas. Peel tests conducted

in this study represent mode-I type of tear propagation in either the circumferential directions or the longitudinal directions but not both. Additional tests that account for the in vivo loading conditions and residual stresses are needed to examine the factors influencing tear propagation in human aortas.

Finally, porcine aortas differ in terms of the concentration of the various wall constituents (elastin, collagen, cells etc.) from human aortas. Previous studies have also reported differences in the mechanical behavior of the porcine aortas compared to aged human aortas[96]. Porcine thoracic aorta is very similar to the aorta of young healthy humans (refer to [97], [98], [13]) who often do not experience aortic dissection. Despite these differences between human and porcine aortas, segmental variations in the peel properties observed in the porcine thoracic aorta may be very similar to that of human aortas, even though individual values might differ. We found in our study that the peel force per unit width in the ascending porcine aorta is less than the peel force per unit width in the aged but healthy human aortas. Due to the much stiffer response of the aged human aortas compared to the porcine aortas[96], the stretch values during the peel experiments on human aortas may still be in the transition region thus rendering the linear assumption a reasonable approximation for the estimation of internal energy.

3. EXPERIMENTAL DETERMINATION OF THE ANISOTROPIC MECHANICAL RESPONSE OF THE PORCINE THORACIC AORTA

3.1 Introduction

Understanding the mechanical behavior of the aortic wall in good health and disease may provide fundamental insights into the pathology of diseases affecting the aortic wall, such as aneurysms, dissection, etc. In this chapter, we are interested in understanding the directional dependence of the mechanical properties of the porcine thoracic aorta using uniaxial tensile tests. The data presented in this chapter can inform the development of new constitutive relations for arterial walls and can be used to evaluate the ability of existing constitutive relations in capturing the uniaxial behavior of the porcine thoracic aorta.

Inflation-extension behavior of various arterial segments have been studied extensively, and well documented ([99], [100], [101], [102], [103]). Two early studies that investigated the anisotropy of the arterial wall using such experiments and laid the basis for the choice of the orthotropic constitutive relations[1] for the arterial wall are due to [109] who examined the material symmetry of the canine thoracic aorta and noted that the blood vessel may be treated as a cylindrically orthotropic tube, and [110] who studied the anisotropy of rat carotid arteries and concluded that the arterial wall of large elastic arteries may be regarded as an incrementally isotropic material for the deformations occurring *in-vivo*. However, there are two caveats with regard to these studies. First, material symmetry is defined at a point and not on gross arterial segments. Second, material symmetry is defined with respect to a particular reference configuration, and it changes with choice of the reference configuration. Therefore, material symmetry of the aorta with respect to the tubular configuration may differ from that of a configuration obtained by flattening the arterial segment

[1] It is well known that the arterial wall is a mixture of cells, extracellular matrix constituents, water, and nutrients. It is inhomogeneous, inelastic, anisotropic, and its constituents are continuously replenished and replaced. In fact, arterial elastin, which is generally regarded as a nearly elastic material, was shown to exhibit viscoelastic behavior ([104], [105], [106]). The walls of large arteries like the aorta also contain smaller blood vessels called vasa vasorum ([107]). Modelling such a complex mixture as a homogeneous elastic material is an oversimplification though it might offer some clues about some aspects of its mechanical behavior, it may be insufficient for in vivo arterial modeling (see [108] concerning the inadequacies and complexities of modeling the walls of blood vessels)

after making a longitudinal cut[2]. Despite the limitations of these studies, it has now become common to assume large arteries like the aorta, carotid artery, etc. to have orthotropic symmetry with respect to the radial, the axial, and the circumferential planes in the flattened configuration ([111], [112]).

Uniaxial and biaxial tests on flattened arterial specimens are unavoidable as arterial tissue is not always available in the tubular form. These tests are particularly useful in case of an aneurysm where the tissue is no longer in an axially symmetric shape. Therefore, one has to understand the mechanical properties and the material symmetry of healthy and diseased arteries in the flattened configuration to develop appropriate constitutive relations with this configuration as the reference configuration. In the case of anisotropic materials, uniaxial and biaxial tests along the planes of symmetry do not fully characterize the mechanical response of the material, as they do not investigate the mechanical response under shear deformation. Most of the studies in the literature conduct uniaxial and biaxial experiments with loading along the circumferential and the longitudinal directions ([111] , [112], [11], [4], [113]). Additionally, most of these studies assume orthotropic symmetry in the flattened configuration, and use the uniaxial and the biaxial constitutive response data to determine the material parameters of the constitutive relations. In fact, there are very few studies that concern tests on specimens oriented along the directions that do not coincide with the circumferential and the axial directions. Recent studies by [114] and [59] investigated the uniaxial failure properties of the dogbone shaped samples from the porcine abdominal and thoracic aortas cut at different orientations with respect to the circumferential direction. Another study by [115] evaluated the uniaxial viscoelastic properties of the porcine thoracic aorta on specimens oriented in different directions. However, these papers do not measure the shear strain during the uniaxial test on specimens that are not oriented along the circumferential and the axial directions, which is likely to be non-zero when the loading direction does not coincide with the directions of symmetry. We present the nominal stress and the Green-St. Venant strain data under uniaxial extension of porcine thoracic aortic specimens oriented at 0°, 30°, 45°, 60° and 90° with respect to the circumferential

[2]Arterial specimens typically remain curved even after introducing a longitudinal cut and it is common to flatten them before a uniaxial/biaxial test

direction.

3.2 Materials and methods

3.2.1 Materials

Fresh aortas (n=10) were collected from male hogs from a slaughterhouse on the Texas A&M university campus during meat harvest and transported in ice. The hogs were not killed for the purpose of this study. The hogs from which aortas were obtained weighed about 250-300lbs, and were 6-8 months old at the time of harvest. They originated from various breeds that are typically used for meat in the United States. Loose connective tissue was carefully removed, and the section of the aorta from the end of the aortic arch to the third branching artery (upper descending aorta) was dissected and placed in a centrifuge tube containing 0.01M Phosphate Buffer Saline(PBS) solution. The centrifuge tube was stored in a freezer at -20^{o}C until the day before the experiments[3]. The day before testing, aortas were taken out and thawed overnight at 4^{o}C in a refrigerator. The aortas were cut open longitudinally, and five dumbbell shaped specimens (Total length $\sim$30mm, gauge length $\sim$10mm, gauge width $\sim$3mm, width of the wider portion of the specimen $\sim$6mm) were punched out as shown in figure 3.1b using a custom machined punch. These five specimens were oriented at 0°, 30°, 45°, 60° and 90° with respect to the circumferential direction. A template printed on paper as shown in figure 3.1a was placed on the intimal side and used for cutting the specimens. We shall refer to the X-coordinate direction in figures 3.1a and 3.1b the circumferential direction as this is the orientation corresponding to the circumference of the cross-section when in the flattened shape. The specimens oriented at 30°, 45° and 60° will be referred to as off-axis specimens. Any loose connective tissue left was cleared off of these specimens and the specimens were placed in PBS at room temperature. Images of the specimens were taken before the experiments for measuring their dimensions. Table 3.1 presents the mean and the standard deviation of the dimensions of the specimens.

[3] [92] found negligible change in the biaxial mechanical response of porcine aorta , when stored at -20°C in isotonic saline solution and tested within one year of the harvest.

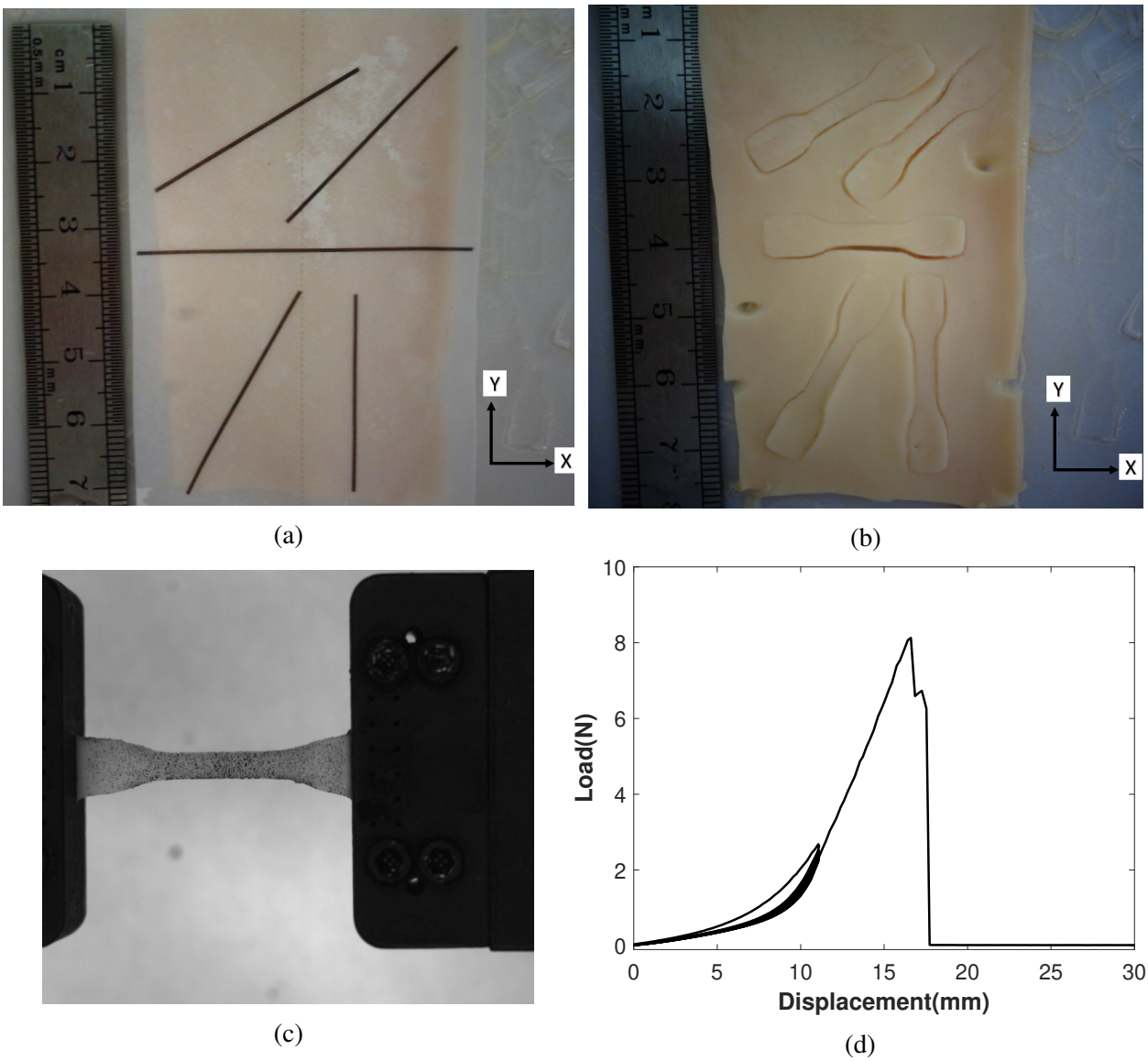

(a) (b) (c) (d)

Figure 3.1: (a) Template used for cutting the samples (b) Porcine aorta with dumbbell-shaped samples cut in different directions. We shall refer to the X-coordinate direction in figures 3.1a and 3.1b the circumferential direction as this is the orientation corresponding to the circumference of the cross-section when in the flattened shape(c) A uniaxial sample during the test with the speckle pattern, (d) Typical load vs. displacement for the preconditioning cycles and the failure test. We shall refer to the X-coordinate direction in figures (a) and (b) the circumferential direction.

Table 3.1: Mean and standard deviation of length between the clamps, width and thickness of the specimens in mm

	0° (circ)	30°	45°	60°	90° (long)
Length between clamps	22.63 ± 0.32	22.77 ± 0.64	22.42 ± 0.46	22.71 ± 0.40	23.07 ± 0.93
Width	2.93 ± 0.17	2.95 ± 0.13	3.07 ± 0.18	3.06 ±0.09	3.01 ± 0.17
Thickness	2.31 ± 0.28	2.14 ± 0.25	2.27 ± 0.17	1.95 ±0.23	2.15 ± 0.18

3.2.2 Methods

The specimens were taken out of the PBS solution before the experiments and fixed to the clamps. Black Rust-Oleum® paint and primer with flat finish was sprayed onto the intimal surface of the specimen to create a random speckle pattern. The speckle pattern for one of the samples is shown in figure 3.1c. The specimen was then transferred to a biaxial machine for testing. For details regarding the biaxial machine, please refer to [116].

3.2.2.1 Experimental protocol

The specimens usually remained curved after placing them in the testing machine. A preload of approximately 0.05 N was applied to straighten the specimens. The length of the specimen between the clamps was measured using a vernier calipers. Preconditioning was carried out by moving one of the clamps to produce a nominal stretch rate of 2%/s up to a nominal stretch of 1.5 (ratio of current length of the specimen between the clamps to the initial length at 0.05N preload) and returning to the initial length at the same stretch rate. Seven preconditioning cycles were performed. The load-displacement data started repeating after 5-6 cycles. The load-displacement data and the images of the specimen were captured every 0.5s. The load-displacement data from one of the experiments is shown in figure 3.1d. After completing 8 cycles, the specimen was immediately stretched until failure at a stretch rate of 2%/s.

3.2.2.2 Data analysis

The load data from the loading part of the 8th cycle and from the failure test was divided by the cross-sectional area of the specimen measured from the images taken before the experiment for calculating the nominal stress. The images were used for extracting the Green-St. Venant strain using Digital Image Correlation (DIC). The DIC analysis was performed using Ncorr ([117]), which is a 2D digital image correlation MATLAB program. The Green-St. Venant strain (**E**) is averaged over the central region of the specimen ($\sim$1.5mm$\times$1.5mm). The X-direction represents the direction along which the clamps were displaced.

3.2.3 Constitutive models and Finite element simulations

To understand the implications of the experimental data obtained in this study, we examined the ability of the constitutive parameters reported in literature to represent the off-axis uniaxial data. We investigated the following two constitutive relations that are commonly used to model the mechanical response of the aortic wall[4]. We reiterate that the constitutive relations discussed refer to purely elastic bodies and as we mentioned earlier, walls of blood vessels are very complex mixtures (see [107]), and thus the constitutive relations considered are very crude approximations for the body under consideration (see [108]). The first constitutive relation considered is a hyperelastic constitutive relation proposed by Baek et al.[67] whose stored energy function is given by

$$W = \frac{c}{2}\left(I_1 - 3\right) + \sum_{i=1}^{4} \frac{k_1^i}{4k_2^i}\left(e^{k_2^i\left(I_4^i-1\right)^2} - 1\right), \tag{3.1}$$

where c is a material parameter, k_1^i and k_2^i are the material parameters associated with the i^{th} fiber family. Invariants I_4^i are given by $I_4^i = \mathbf{M}_i.\mathbf{C}\mathbf{M}_i$, where $\mathbf{M}_i$ is the unit vector along the i^{th} fiber, $\mathbf{C} = \mathbf{F}^{\text{T}}\mathbf{F}$ is the right Cauchy-Green tensor with $\mathbf{F}$ as the deformation gradient. Four fibers are considered in this model with $\mathbf{M}_1$ along the circumferential direction of the aorta, $\mathbf{M}_2$

[4]Most of the constitutive relations used for describing the mechanical response of arteries, including the ones listed here, assume a form of the stored energy that is dependent on a partial set of fiber invariants. While such models demonstrated good ability to capture the biaxial constitutive response of the arteries, they may be ill-equipped to capture the shear behavior of the orthotropic materials ([78]), and may display a behavior that is not typical of fiber reinforced materials under certain deformations ([79], [80]).

along the longitudinal direction, $\mathbf{M}_3$ and $\mathbf{M}_4$ symmetrically oriented at angles $\pm\phi$ with respect to the circumferential direction. The fiber families along $\mathbf{M}_3$ and $\mathbf{M}_4$ are generally regarded as mechanically equivalent, and the material constants associated with these directions are taken to be $k_1^3 = k_1^4$ and $k_2^3 = k_2^4$. Thus, there are 8 parameters associated with this constitutive relation. The first Piola-Kirchhoff stress for this constitutive relation is given by

$$\mathbf{P} = -p\mathbf{F}^{-\mathrm{T}} + c\mathbf{F} + \sum_{i=1}^{4} k_1^i \left(I_4^i - 1\right) \left(e^{k_2^i \left(I_4^i - 1\right)^2}\right) \mathbf{F}\mathbf{M}_i \otimes \mathbf{M}_i, \tag{3.2}$$

and the Cauchy stress associated with this constitutive relation is given by

$$\mathbf{T} = -p\mathbf{I} + c\mathbf{B} + \sum_{i=1}^{4} k_1^i \left(I_4^i - 1\right) \left(e^{k_2^i \left(I_4^i - 1\right)^2}\right) \mathbf{F}\mathbf{M}_i \otimes \mathbf{F}\mathbf{M}_i, \tag{3.3}$$

where $\mathbf{B} = \mathbf{F}\mathbf{F}^{\mathrm{T}}$ is the left Cauchy-Green tensor. This constitutive relation is reported to have a good capability in modeling the uniaxial and the biaxial mechanical response of the arterial wall when compared to other popular constitutive relations and in particular, the mechanical response of the porcine thoracic aorta ([118], [3]) and the human abdominal aorta [119]. Material parameters associated with this constitutive relation for the porcine thoracic aorta are taken from the study by Schroeder et al. [3] (Table A.1). They obtained these parameters by fitting the constitutive relation to the biaxial stress-deformation data on specimens oriented in circumferential-longitudinal direction.

The second constitutive relation is a hyperelastic constitutive relation proposed by Holzapfel et al.[112]. Stored energy function for this constitutive relation is given by

$$W = \frac{c}{2}\left(I_1 - 3\right) + \sum_{i=1}^{2} \frac{k_1}{2k_2} \left(e^{k_2\left[\rho\left(I_4^i - 1\right)^2 + (1-\rho)(I_1 - 3)^2\right]} - 1\right), \tag{3.4}$$

where c is a material parameter, k_1 and k_2 are the material parameters associated with two mechanically equivalent fibers oriented symmetrically at $\pm\phi$ with respect to the circumferential direction, and the invariants I_4^i are given by $I_4^i = \mathbf{M}_i.\mathbf{C}\mathbf{M}_i$. The anisotropic term due to the i^{th}-fiber con-

tributes to the stored energy only when the invariant $I_4^i > 1$. The first Piola-Kirchhoff stress (**P**) and the Cauchy stress (**T**) associated with this constitutive relation are given by

$$\mathbf{P} = -p\mathbf{F}^{-\mathrm{T}} + \left(c + 2(1-\rho) \sum_{i=1}^{2} k_1 \left(e^{k_2 \left[\rho \left(I_4^i - 1 \right)^2 + (1-\rho)(I_1 - 3)^2 \right]} \right) (I_1 - 3) \right) \mathbf{F} + 2\rho \sum_{i=1}^{2} k_1 \left(I_4^i - 1 \right) \left(e^{k_2 \left[\rho \left(I_4^i - 1 \right)^2 + (1-\rho)(I_1 - 3)^2 \right]} \right) \mathbf{F}\mathbf{M}_i \otimes \mathbf{M}_i, \quad (3.5)$$

$$\mathbf{T} = -p\mathbf{I} + \left(c + 2(1-\rho) \sum_{i=1}^{2} k_1 \left(e^{k_2 \left[\rho \left(I_4^i - 1 \right)^2 + (1-\rho)(I_1 - 3)^2 \right]} \right) (I_1 - 3) \right) \mathbf{B} + 2\rho \sum_{i=1}^{2} k_1 \left(I_4^i - 1 \right) \left(e^{k_2 \left[\rho \left(I_4^i - 1 \right)^2 + (1-\rho)(I_1 - 3)^2 \right]} \right) \mathbf{F}\mathbf{M}_i \otimes \mathbf{F}\mathbf{M}_i. \quad (3.6)$$

Contribution of the anisotropic term corresponding to the i^{th}-fiber direction is neglected when $I_4^i < 1$ by replacing all $I_4^i - 1$ and $(I_4^i - 1)^2$ terms with $\mathcal{H}\left(I_4^i - 1\right)\left(I_4^i - 1\right)$ and $\mathcal{H}\left(I_4^i - 1\right)\left(I_4^i - 1\right)^2$ respectively, in equations 3.5 and 3.6, where $\mathcal{H}(x)$ is a step function defined by

$$\mathcal{H}(x) = \begin{cases} 0, & x < 0 \\ 1, & x > 0 \end{cases} \quad (3.7)$$

with a smooth variation from 0 to 1 between $x = -0.0005$ and $x = 0.0005$. Material parameters associated with this constitutive relation for the porcine thoracic aorta are taken from Peña et al.[4] (Table 2 in [4]).

3.2.3.1 Finite element simulations

A dumbbell shaped geometry shown in figure 3.8a was used for simulations (all dimensions in millimeters). Plane stress conditions were assumed, and a deformation gradient of the form given

by

$$\mathbf{F} = \begin{bmatrix} 1 + \frac{\partial u}{\partial \mathrm{X}} & \frac{\partial u}{\partial \mathrm{Y}} & 0 \\ \frac{\partial v}{\partial \mathrm{X}} & 1 + \frac{\partial v}{\partial \mathrm{Y}} & 0 \\ 0 & 0 & \frac{1}{\left(1+\frac{\partial u}{\partial \mathrm{X}}\right)\left(1+\frac{\partial v}{\partial \mathrm{Y}}\right) - \frac{\partial u}{\partial \mathrm{Y}}\frac{\partial v}{\partial \mathrm{X}}} \end{bmatrix}, \tag{3.8}$$

was assumed, where $u = u(\mathrm{X}, \mathrm{Y})$ and $v = v(\mathrm{X}, \mathrm{Y})$ are the displacements along X-axis and Y-axis respectively. $\{\mathrm{X}, \mathrm{Y}\}$ are the coordinates of a particle in the undeformed configuration, which was assumed to be the stress-free. Incompressibility of the material is assumed in calculating the deformation gradient. To simulate the clamping of the specimen at the left and the right ends, the following boundary conditions were applied: 1) The left edge of the specimen was held fixed by specifying the boundary condition, $u = 0$ and $v = 0$, 2) The right edge was allowed to move only in the X-direction by applying a displacement u_0 in the X-direction ($u = u_0$) and holding $v = 0$. A traction free boundary condition was applied to the remaining edges through $\mathbf{PN} = \mathbf{0}$, where $\mathbf{N}$ is the unit normal to the edge in the reference configuration. The deformation gradient given by equation 3.8 is substituted in equations 3.2, 3.5 to obtain the first Piola-Kirchhoff stress, and the Lagrange multiplier p is eliminated from the equations using the plane stress condition, $\mathrm{T}_{33} = 0$. The governing equations are given by

$$\frac{\partial \mathrm{P}_{\mathrm{XX}}}{\partial \mathrm{X}} + \frac{\partial \mathrm{P}_{\mathrm{XY}}}{\partial \mathrm{Y}} = 0 \tag{3.9}$$

$$\frac{\partial \mathrm{P}_{\mathrm{YX}}}{\partial \mathrm{X}} + \frac{\partial \mathrm{P}_{\mathrm{YY}}}{\partial \mathrm{Y}} = 0 \tag{3.10}$$

The displacement u_0 is varied from 0mm to 11mm such that the nominal stretch varies from 1 to 1.5. The governing equations were solved in COMSOL Multiphysics (Mathematics module) using quadratic triangular elements. The relative tolerance was set to 10^{-6} for the simulations. The mean value of each component of the Green-St. Venant strain ($\mathbf{E}$) is computed over a square region at

the center of the specimen, highlighted in figure 3.8a using the equation

$$E_{ij}^{mean} = \frac{\int_A E_{ij} dA}{\int_A dA} = \frac{\frac{1}{2}\int_A (C_{ij} - \delta_{ij})\, dA}{\int_A dA} \tag{3.11}$$

where δ_{ij} is the Kronecker delta.

3.3 Results

The legend in all figures indicate the aorta from which the specimen was obtained. Figure 3.2 shows the mean curves for the variation of the nominal stress, E_{XX}, E_{YY}, and E_{XY} with nominal stretch for the loading part of the 8^{th}-cycle for all specimens. Data for individual specimens is given in Appendix A. Figure 3.3 shows the variation of the nominal stress with nominal stretch, and figures 3.4, 3.5 and 3.6 show the dependence of E_{XX}, E_{YY} and E_{XY}, respectively on nominal stretch for the failure test. Response characteristics during the last cycle are very similar to that of the failure test. Anisotropy of the aorta is evident even at stretches close to 1.1, where the mean response curves from different orientations shown in figure 3.2 do not overlap one another. For the specimens from all orientations, the nominal stress and E_{XX} increases with stretch, while E_{YY} decreases with nominal stretch due to Poisson effect. As shown in figure 3.3, specimens from all orientations display a nonlinear nominal stress-nominal stretch response with toe, heel and stiff (often called the "linear" region in the literature) regions that is characteristic of the soft tissues, with an appreciable change in the slope occurring in the stretch range of 1.35-1.45. This stiffening response is generally attributed to the increased fraction of collagen fibers straightening with stretch, and resisting the deformation ([120]). Within the same stretch range, a corresponding change in the slope can be noticed in the E_{XX}-nominal stretch and the E_{YY}-nominal stretch curves. The slope of the E_{XX}-nominal stretch curve decreases slightly (see figure 3.4) after a stretch of 1.35-1.45 due to faster stiffening of the narrower gauge region of the specimen, which is subjected to a higher nominal stress at a given value of nominal stretch, compared to the wider region of the specimen. Further, the rate at which the specimen contracts ($-d(E_{YY})/d(\text{Nominal stretch})$) due to Poisson effect, in the direction perpendicular to the loading also increases beyond the nominal

stretch of 1.35 for all the specimens (see figure 3.4) due to increased stiffness of the specimen in the loading direction owing to the straightening and reorientation of the collagen fibers.

The qualitative features of the E_{XY}-nominal stretch response strongly depend on the orientation of the specimen (figures 3.2d and 3.6). For specimens oriented at 30° with the circumferential direction, E_{XY} monotonically decreases with nominal stretch. Interestingly, specimens oriented at 45° and 60° exhibit a non-monotonic crescent-shaped relation between E_{XY} and nominal stretch, with a minimum in E_{XY} occurring between nominal stretches of 1.35 and 1.45. The slope of the E_{XY}-nominal stretch curve is negative at smaller stretch and becomes positive at larger nominal stretch. This leads to the specimens undergoing a negative shear strain at smaller values of the nominal stretch. At larger nominal stretches, shear strain becomes positive as seen in figures 3.6c and 3.6d.

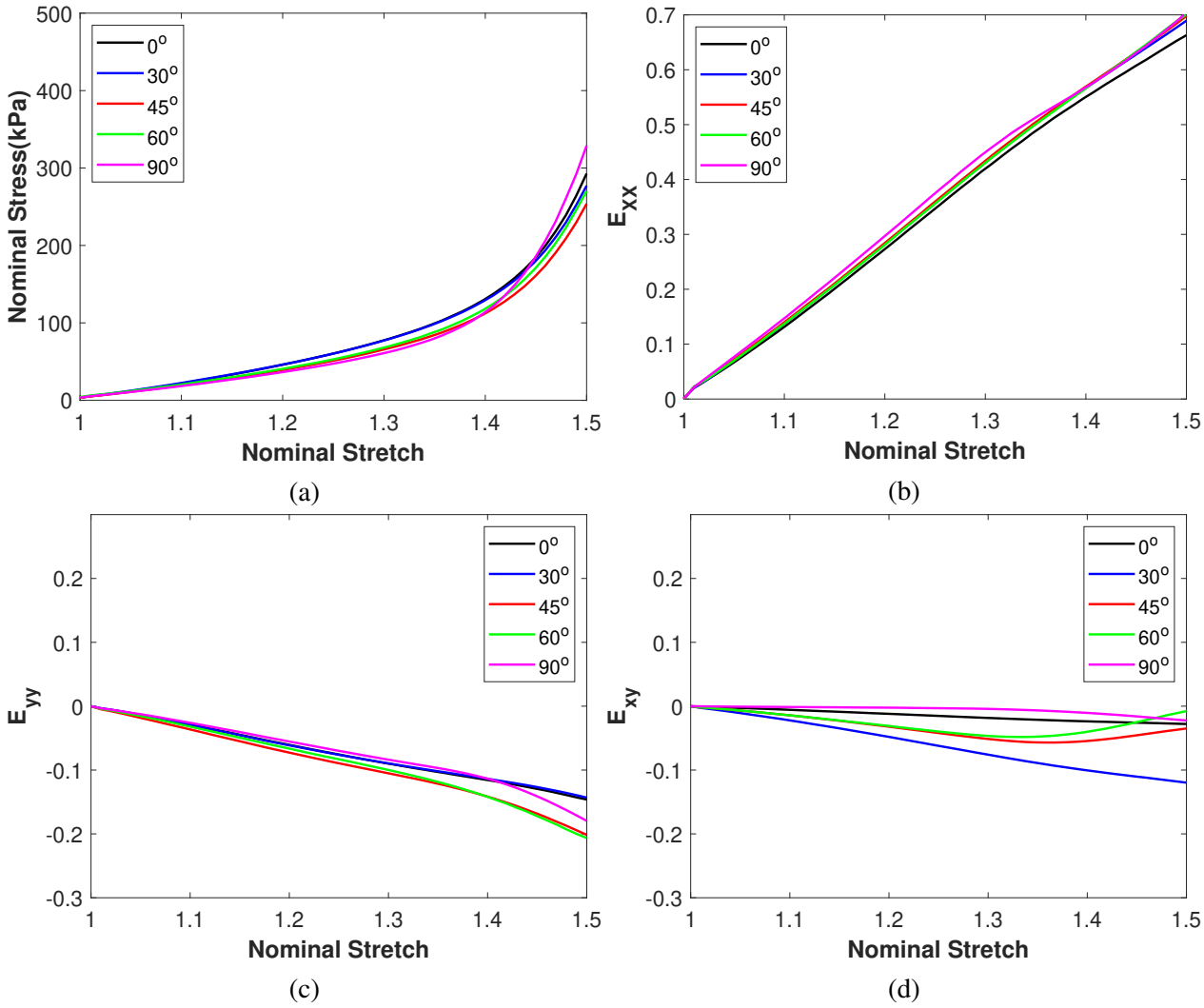

Figure 3.2: Variation of the mean values of (a) nominal stress, (b) E_{XX}, (c) E_{YY} , (d) E_{XY} with nominal stretch for the loading part of the 8^{th}-cycle.

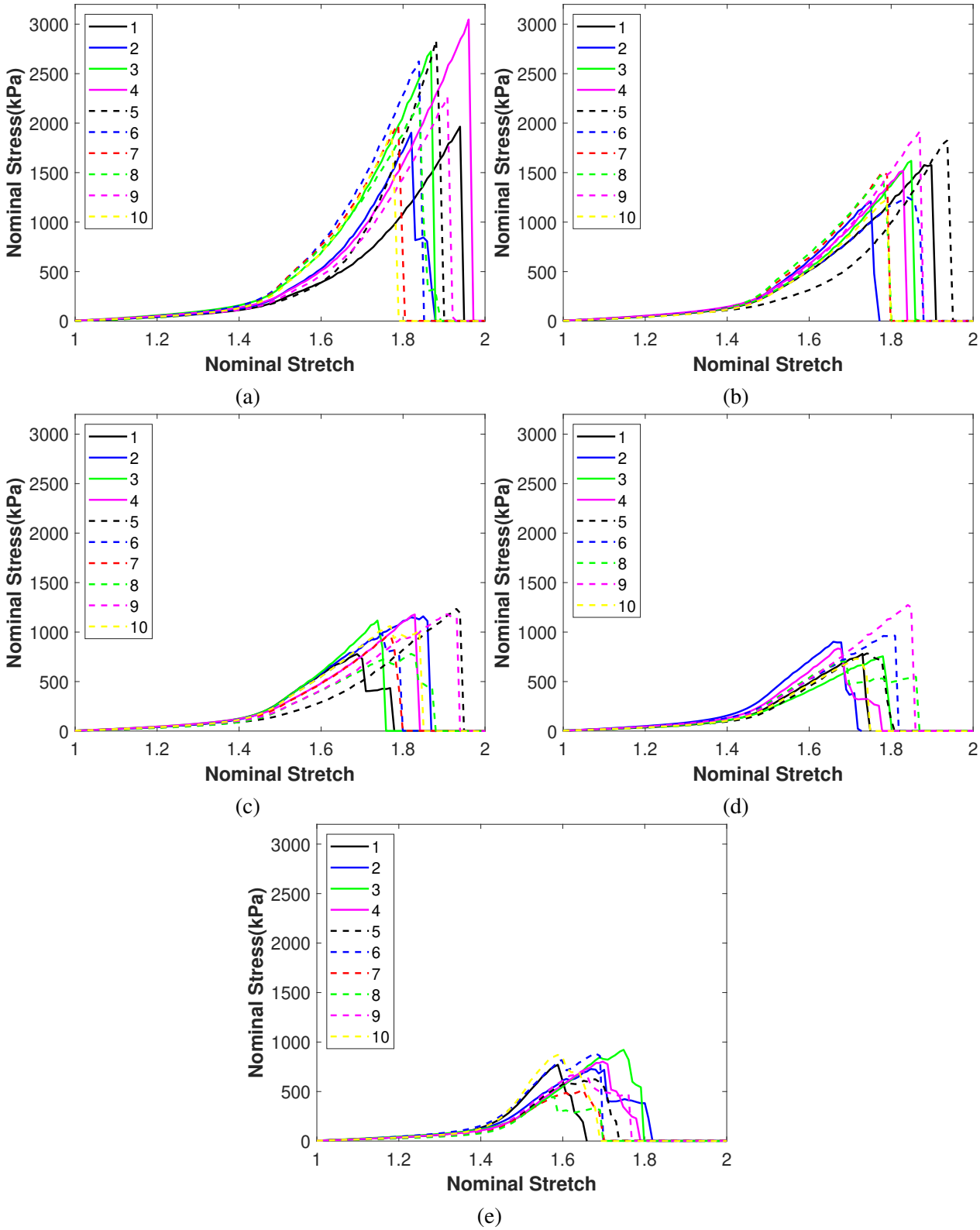

Figure 3.3: Variation of nominal stress with nominal stretch for the samples oriented at (a)0^o (circ), (b) 30^o, (c) 45^o, (d) 60^o, (e) 90^o (long) with the circumferential direction for the failure test. The legend in the figure indicates the aorta from which the specimen is obtained.

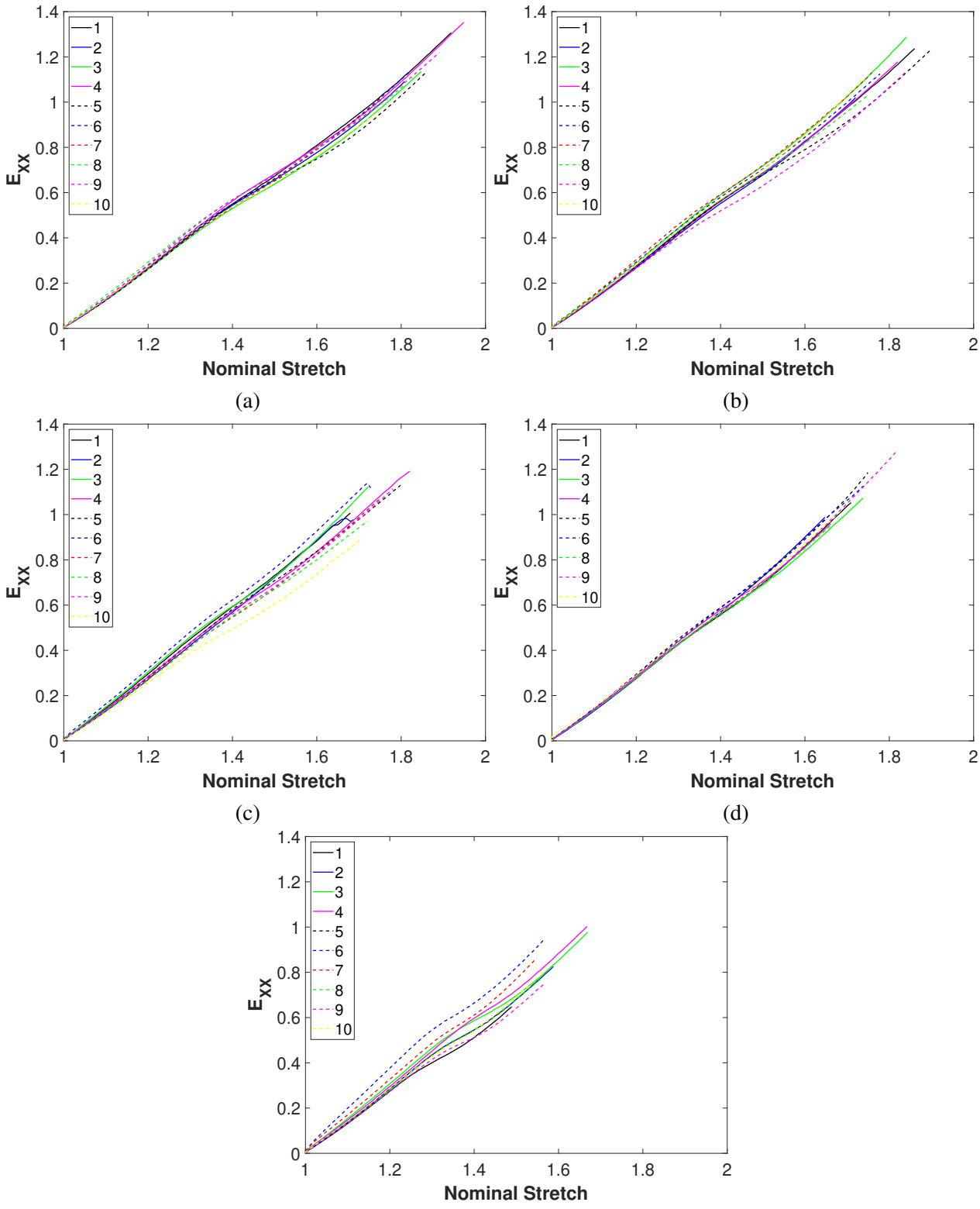

Figure 3.4: Variation of E_{XX} with nominal stretch for samples oriented at (a)0^o (circ), (b) 30^o, (c) 45^o, (d) 60^o, (e) 90^o (long) with the circumferential direction for the failure test. The legend in the figures indicates the aorta from which the specimen is obtained.

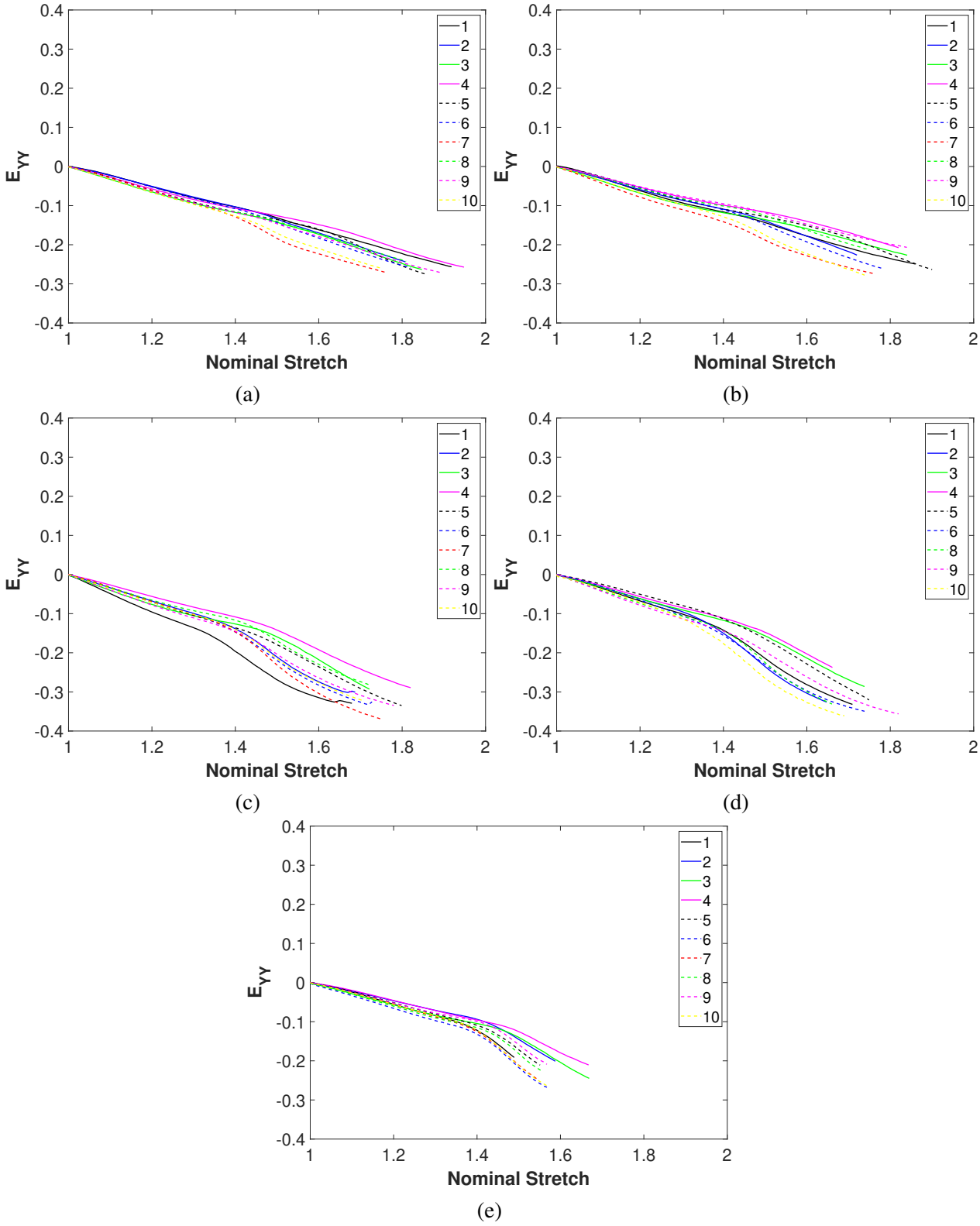

Figure 3.5: Variation of E_{YY} with nominal stretch for samples oriented at (a)0^o (circ), (b) 30^o, (c) 45^o, (d) 60^o, (e) 90^o (long) with the circumferential direction for the failure test. The legend in the figures indicates the aorta from which the specimen is obtained.

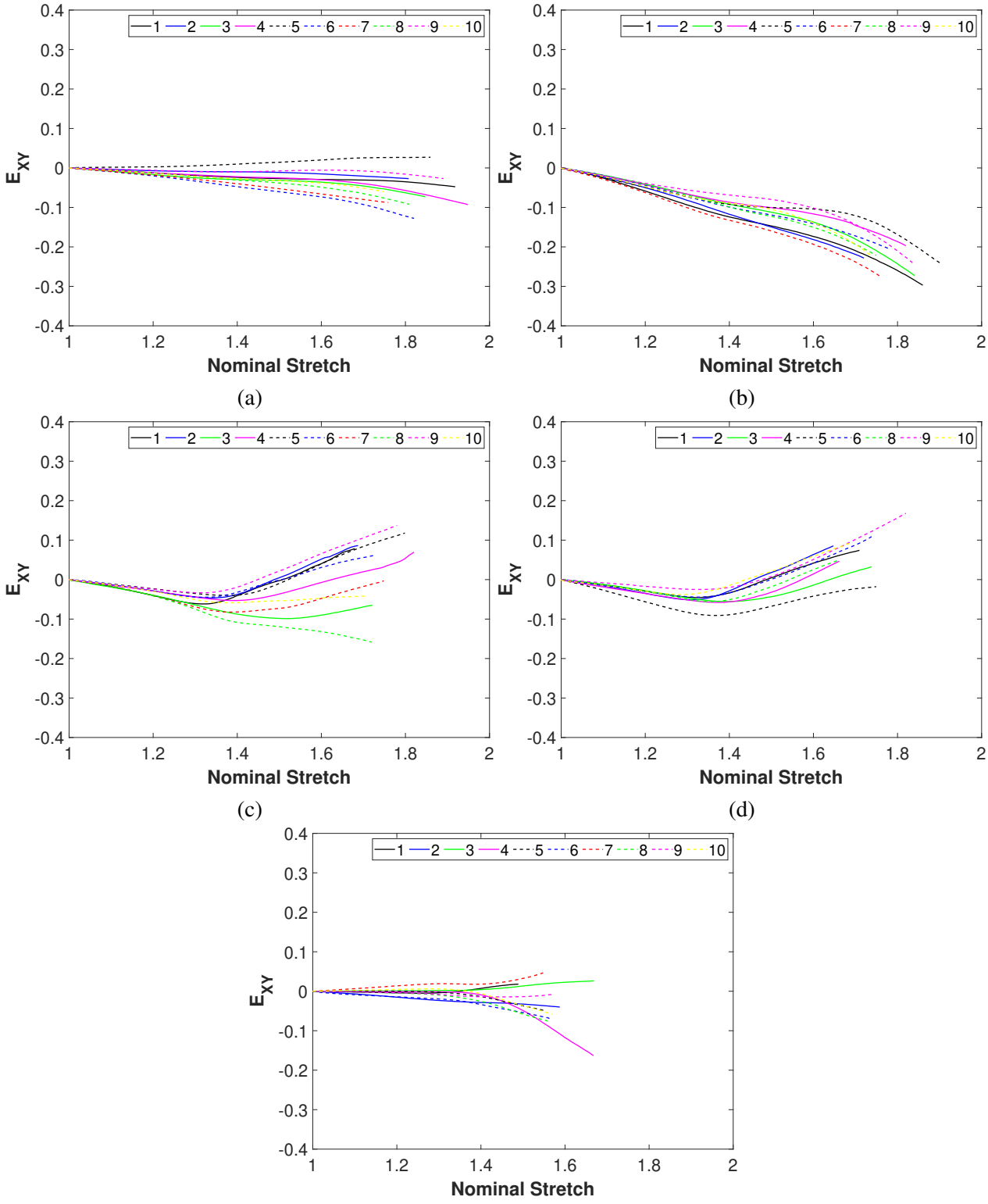

Figure 3.6: Variation of E_{XY} with nominal stretch for samples oriented at (a)0^o (circ), (b) 30^o, (c) 45^o, (d) 60^o, (e) 90^o (long) with the circumferential direction for the failure test. The legend in the figure indicates the aorta from which the specimen is obtained.

Table 3.2 presents the mean and the standard deviation of the nominal stress at failure (complete rupture) for specimens from different orientations. The failure stress decreases with the increased orientation angle of the specimen with the circumferential direction. However, no significant difference (p>0.3 in a paired t-test) in the failure stress was found between the 60° and the longitudinal specimens.

Table 3.2: Mean and standard deviation of the failure stress in MPa.

0° (circ) (n=10)	30° (n=9)	45° (n=9)	60° (n=9)	90° (long) (n=9)
2.35 ± 0.40	1.54 ± 0.22	1.03 ± 0.16	0.86 ± 0.17	0.76 ± 0.12

Important features of the failure of the specimens from different orientations are shown in figure 3.7. Except for four specimens, rupture always occurred in the narrow (gauge) region. However, the location where the cleavage occurs varies along the thickness direction of the specimen. As shown in figures 3.7a-3.7d, the location of cleavage differs between the intimal side (the surface with the speckle pattern) and the adventitial side resulting in a shearing type delamination, which can be seen in figures 3.7a and 3.7b. All the longitudinal samples had cleavage initiation from the intimal side. For the circumferential specimens, the cleavage was either abrupt or initiated from the intimal side. However, there was no consistent pattern for the off-axis specimens. Cleavage initiation was almost equally likely from both the intimal and the adventitial sides, and many 30° specimens failed abruptly. A large delamination region can be observed in circumferential specimens (an example is shown in figures 3.7a and 3.7b). Specimens from other orientations also display this delamination phenomenon with a smaller delamination region (see smaller delamination regions for 45° and 60° specimens in figures 3.7d and 3.7f, respectively). It can be further observed in figures 3.7d and 3.7f that the rupture plane is not always orthogonal to the direction of uniaxial extension. This is especially true for the rupture in off-axis specimens, where the rupture

plane is almost always angled with respect to the direction of uniaxial extension.

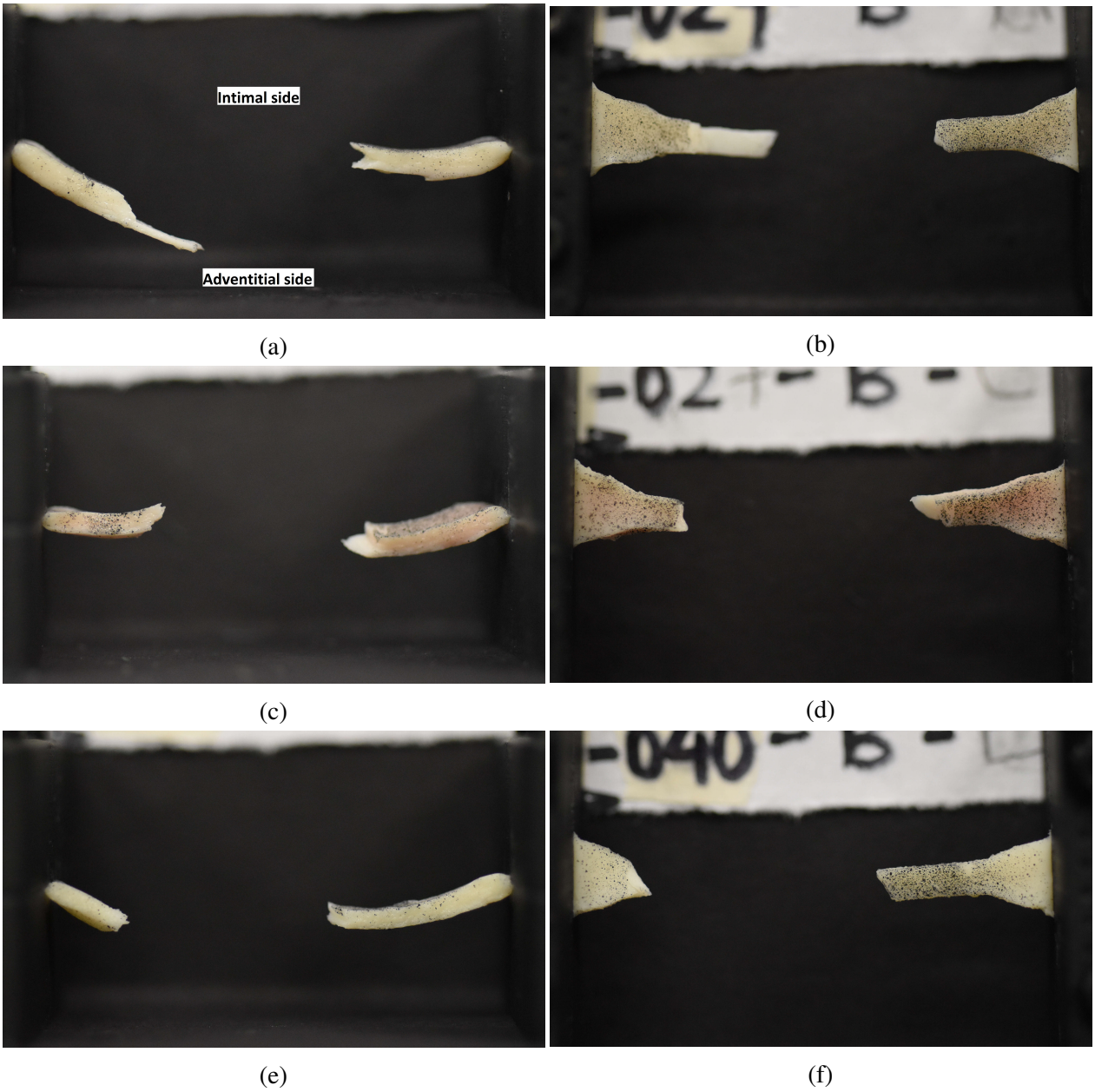

(a) (b)

(c) (d)

(e) (f)

Figure 3.7: Figures (a), (b) show failure in the circumferential specimen cut from aorta 8, Figures (c), (d) show failure in the 45° specimen cut from aorta 3, Figures (e), (f) show failure in the 60° specimen cut from aorta 6. In figures (a), (c) and (e), the intimal surface is facing the top of the image and the adventitial surface is facing the bottom of the image. Images in figures (b), (d) and (f) were taken with the camera facing the intimal surface.

3.4 Discussion

In this chapter, we have presented the data on the uniaxial mechanical response of the porcine thoracic aorta using dumbbell specimens oriented along 0°, 30° , 45°, 60°, and 90° with the circumferential direction. Very few studies in literature examine the mechanical properties of the aorta along non-circumferential and non-longitudinal directions ([115], [114], [59]). The studies by [114] and [59] presented the constitutive response of the specimens under the assumption that the grips prevented the off-axis samples from shearing. The assumption that the grips prevent the off-axis samples from shearing, as shown in our study, does not seem to be appropriate as the off-axis specimens undergo significant shearing. Therefore, it is important to account for the shear strain in the off-axis tests. It must be noted that the circumferential and the longitudinal specimens also undergo a small amount of shear (E_{XY}), which may be attributed to a small error associated with the specimen orientation when punching out. Even though it is very difficult to cut the specimens to align with circumferential and longitudinal directions perfectly, and one commonly expects them to undergo a small amount of shear during uniaxial extension, the shear strain data for the circumferential and the longitudinal specimens are often not reported in the literature. In fact, many studies do not even report E_{YY} or λ_Y, and use only the nominal stress- nominal stretch data for finding the material parameters of the constitutive relations. Measuring full-field deformation may enable better estimation of material parameters that appear in the constitutive relations used to describe blood vessel walls using techniques like inverse numerical analysis.

The simulation results for the four-fiber family constitutive relation are shown in figure 3.8, and the results for the two-fiber constitutive relation are shown in figure 3.9. While material parameters for both the constitutive relations obtained from biaxial tests are able to qualitatively represent the nominal stress-nominal stretch response of the specimens from different orientations to an extent (compare these results with figure 3.2a), they are unable to capture the variation of E_{YY} and E_{XY} with nominal stretch. Such discrepancy further points to the important and useful information provided by the tests along non-circumferential and non-longitudinal directions.

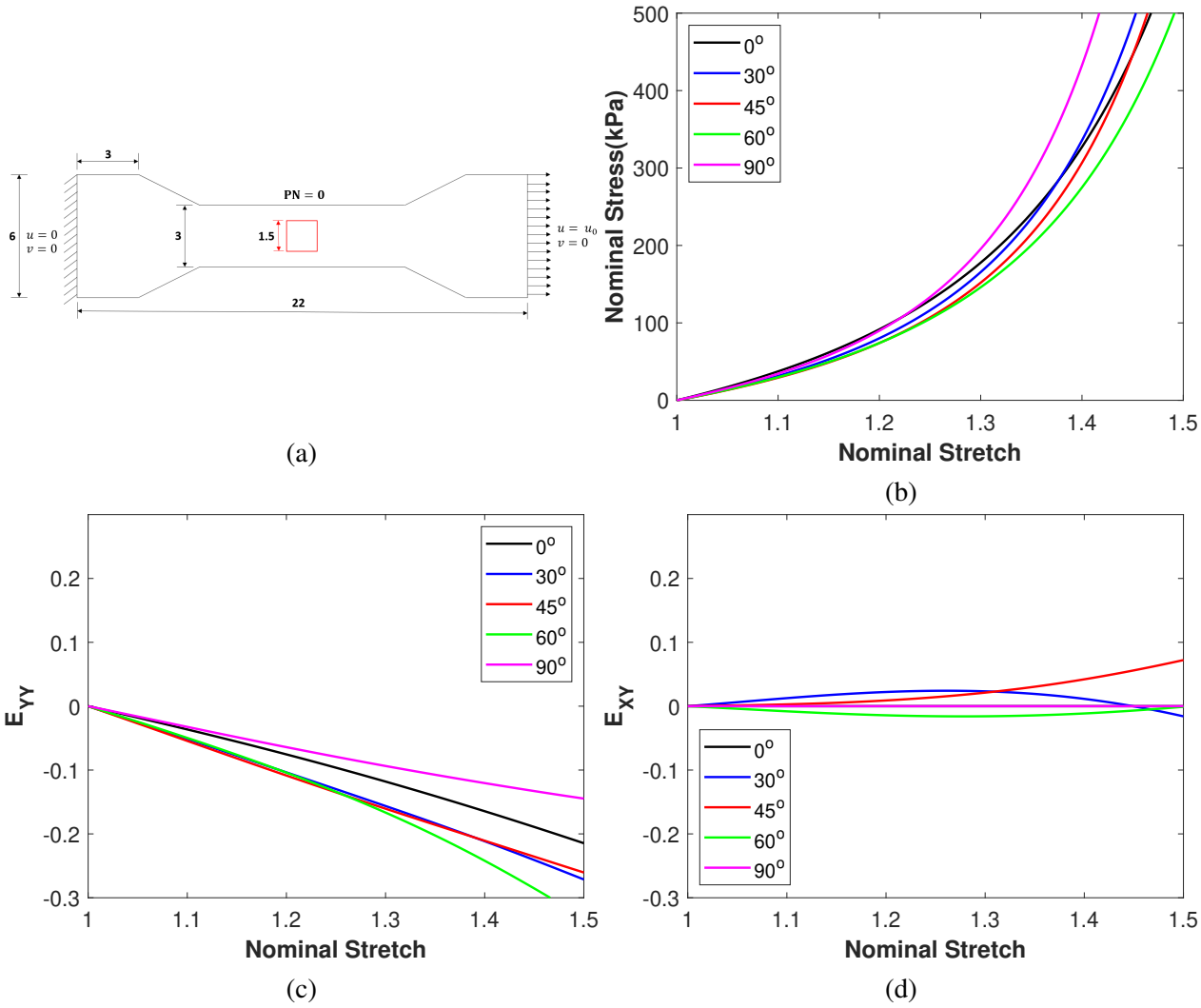

Figure 3.8: (a) Dumbbell geometry used for simulations. All dimensions are shown in mm. The square region used for calculating the mean values of the Green- St. Venant strain is shown using the red line. Figures (b), (c), (d) are numerical results obtained using material parameters $c = 3.82$, $k_1^1 = 77.84$, $k_2^1 = 0.55$, $k_1^2 = 98.42$, $k_2^2 = 0.99$, $k_1^3 = k_1^3 = 68.78$, $k_2^3 = k_2^4 = 0.89$, $\phi = 37.82$ reported by [3]. c, k_1^i are expressed in kPa, ϕ is expressed in degrees, and k_2^i are dimensionless.

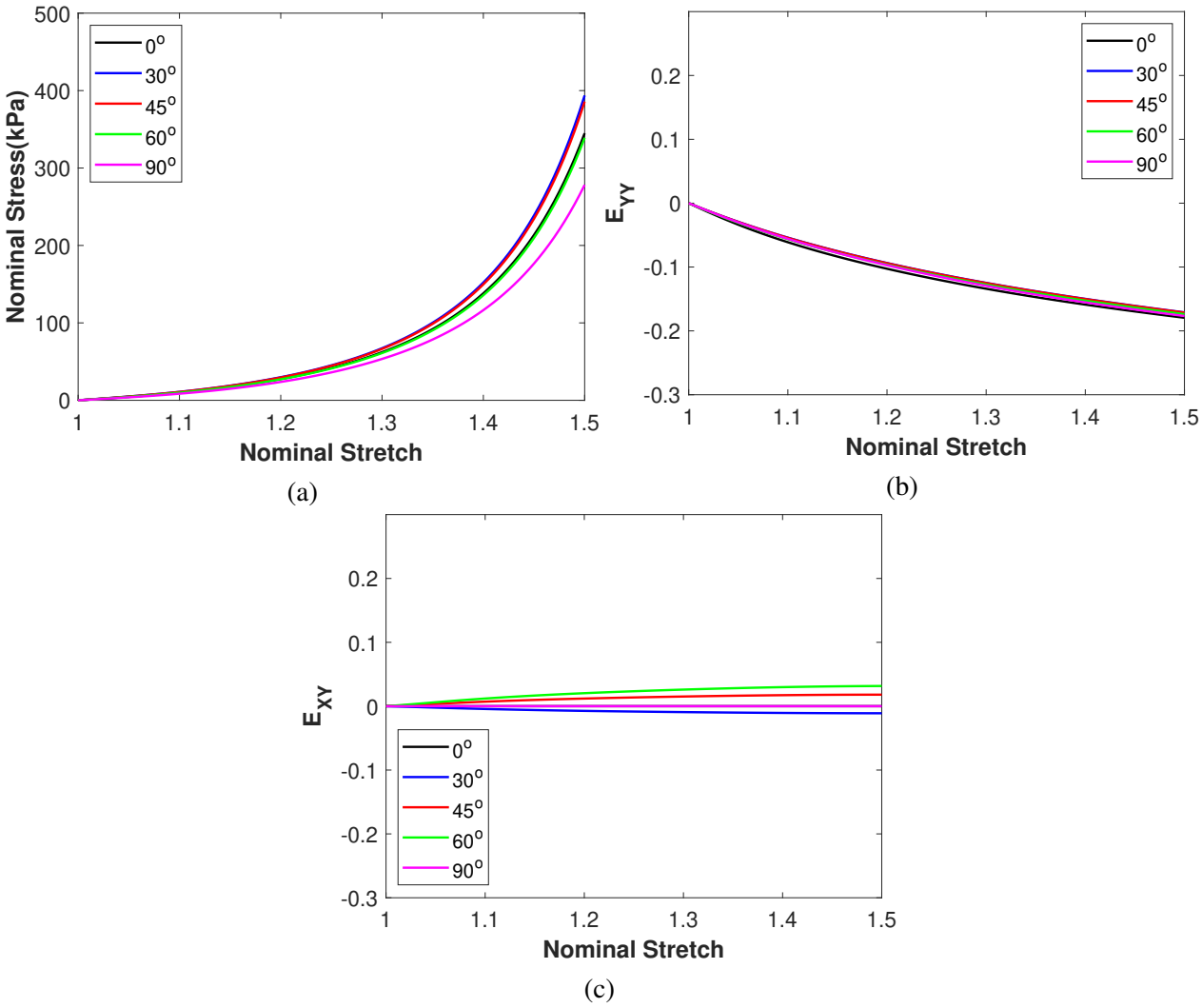

Figure 3.9: Figures (a), (b), (c) are numerical results obtained using material parameters $c = 20.0$, $k_1 = 40.0$, $k_2 = 2.4$, $\rho = 0.112$, $\phi = 35.5$ reported by [4]. c, k_1 are expressed in kPa, ϕ is expressed in degrees, and k_2 and ρ are dimensionless.

As pointed out in the results section, the porcine aorta exhibits anisotropic response even at small stretches where the mechanical behavior is thought to be elastin dominant. Previous studies by [121], and [122] showed the arterial elastin to be anisotropic, and the data presented here indicate the same. In addition to elastin, the aorta is a mixture of several extracellular matrix constituents (collagen, glycosaminoglycans, water, etc.), smooth muscle cells and fibroblasts. Different constituents of the arterial wall may have different natural configurations and may have been

deposited in the aortic wall at a different pre-stress/pre-stretch ([123]) . The concept of multiple natural configurations was used to model phenomena like plasticity, viscoelasticity, phase transition ([124], [125]), and to describe the growth and remodeling in biological tissues ([126]). The slope change that occurs in nominal stress-nominal stretch, **E**-nominal stretch curves at a nominal stretch between 1.35-1.45 is a possible indication of a need for using more than one natural configuration for modeling the mechanical response of the aorta even in the absence of growth and remodeling. Further, it is beyond the stretch of 1.3, where collagen contributes to the mechanical response, the differences between aortas from different animals, and specimens from different orientations become prominent. Using multiple natural configurations to model the mechanical response of the arterial wall may assist in better quantification of the contribution of individual constituents to the overall arterial behavior.

Damage and failure in thoracic and abdominal aorta have been studied extensively in the past ([14], [11], [114], [59], [24], [25], [127], [60], [12], [128], [10]). [114] and [59] reported a decreasing tensile strength of the aorta from the circumferential direction to the longitudinal direction in the porcine thoracic and abdominal aortas, and the human ascending thoracic aortic aneurysms. Although actual values of the failure strength are different in our study, we observed a similar trend in the failure strength. However, stress at failure is clearly insufficient to characterize rupture in the porcine aorta as evident from differences in the cleavage initiation and the location of rupture between the layers of the aorta. Further, it indicates the tensile strength of the individual layers of the aorta to be different. Previous studies by [14], [128] reported a similar phenomenon, where failure initiation occurs in one of the wall layers. Constitutive relations for describing the failure of the arterial wall must therefore account for layer-specific differences in the mechanical and the failure properties. Examining the directional dependence of the layer-specific mechanical properties will provide additional data for evaluating the constitutive relations that are used to model the layer-specific mechanical response, and the data provided here can be used to assess the ability of such constitutive relations to simulate the response of the whole aortic wall.

Some limitations to our experiments must be pointed out. We conducted our experiments at

room temperature without a tissue bath. Temperature and hydration of the tissue may produce certain differences in the mechanical properties ([94], [95]) compared to the data reported here. We do not, however, expect this to have a significant effect on the overall qualitative features of the mechanical response of the aorta. For the aorta inside the human body, there is a continuous supply of blood to the outer third of the media through vasa vasorum, which is absent in ex-vivo experiments. It is unknown how this might affect the mechanical properties of the aorta. We chose a specimen size that ensured rupture to occur in the gauge region of the dumbbell, and the strain data to be nearly uniform in the central region of the specimen. We conducted some preliminary tests on longer and wider rectangular specimens from different orientations, where we observed similar mechanical response. Further investigation is needed to evaluate the influence of sample size on the mechanical properties, as there is no standard shape or size suggested for testing the aorta ([129]).

In conclusion, the mechanical response data presented here pointed to the need for off-axis tests on arterial walls and indicated the importance of measuring the full 2D deformation undergone by the specimen during a uniaxial test.

4. STRESS CONCENTRATION FACTORS AROUND A CIRCULAR HOLE IN TWO FIBER REINFORCED MATERIALS UNDER LARGE DEFORMATIONS

In this chapter, we study the deformation and the stress concentration factor due to a small circular hole in a thin nonlinearly elastic large sheet reinforced by two families of fibers under a state of plane stress undergoing large deformations. We restrict our attention to the class of materials wherein the fibers are mechanically equivalent, rendering the body orthotropically symmetric with respect to the planes whose normals are along the angular bisectors of the angles between the fibers. Such a body is assumed to be relevant to biological tissues, though, as we explain below, it is a rather crude first approximation for tissues. Furthermore, we limit ourselves to the problems of equibiaxial, uniaxial and pure shear deformations of the body whose fibers are symmetrically oriented with respect to the Cartesian coordinate axes. We compare the stress concentration factor distribution around a circular hole when using a constitutive relation based on a partial set of invariants (I_4, I_6) versus an extended constitutive relation that incorporates the full set of invariants $(I_4, ..., I_8)$ and reduces appropriately to the orthotropic linearized elastic case.

4.1 Introduction

Most fiber reinforced composites and, in particular, human and animal tissues are not elastic, isotropic, or homogeneous ([108]). In fact, they are not merely solids but a mixture of a solid and a fluid (each cell has nearly 70% fluid content). However, modeling tissues as mixtures presents formidable difficulties as we have to consider the various constituents comprising the tissue and specifying boundary and initial conditions associated with each constituent. Hence as a first step, one often models tissues as hyperelastic bodies ([130]), wherein one starts with the assumption of the existence of a stored energy function. Finding the form of the stored energy function (or the response functions, which are the derivatives of the stored energy with respect to the invariants) for the material under consideration is not an easy task. The paucity of experimental data in the case of tissues prompts one to guess/choose a form for the stored energy rather than determine

the response functions based on experimental data. Various forms for the stored energy function have been used for different tissues[1] ([71]). Some of these constitutive relations have become extremely popular to the extent that they are now available in commercial finite element softwares like Abaqus, COMSOL, etc.

Most of these constitutive relations are based on a form for the stored energy function that is dependent only on a partial set of fiber invariants. For example, one of the popular constitutive relations for the arterial walls proposed by [72] assumes the isochoric part of their stored energy function to be dependent only on two fiber invariants rather than the full set containing five fiber invariants. While such assumptions reduce the number of response functions in a constitutive relation, as pointed out by Murphy ([76], [77]), the constitutive relations that are based on a partial set of fiber invariants do not reduce to the constitutive expression corresponding to the linearized theory of elasticity of a body reinforced by one or several families of fibers. [79]. [80] further showed that bodies described by using a partial set of fiber invariants exhibit a response that is not typically observed in uniaxial experiments on fiber reinforced materials. In this paper, we consider two constitutive relations: the first one often referred to in the literature as the "standard fiber-reinforcing" model ([131]), which does not reduce to the constitutive equation for a linearized elastic body composed of two families of fibers ([77]), and the second constitutive relation that is compatible upon linearization with the linearized theory for a body composed of two families of fibers.

While analytical solutions are available for stress distribution around circular and elliptic holes in anisotropic linearized elastic bodies under plane stress and plane strain ([132]), there is very limited literature on the stress distribution around holes in infinite plates/sheets of anisotropic materials undergoing large deformations. To the authors' knowledge, the study of stress distribution around holes in transversely isotropic and orthotropic elastic materials is limited to the problem of a hole in a plate/sheet of material under radial deformation ([133]).

The organization of this chapter is as follows: In section 4.2, we introduce the kinematics

[1] We reiterate that modeling tissues as elastic solids is a drastic simplification, but it can provide useful information in a gross sense concerning the deformation of the tissues.

associated with the deformation of a body, the balance laws, and the constitutive equations. We then describe the boundary values problems studied in this chapter. In section 4.3, we discuss the results, and in section 4.4, we present the conclusions of our study.

4.2 Preliminaries

4.2.1 Kinematics and constitutive equations

Let $\kappa_R(\mathcal{B})$ be the reference configuration associated with the body $\mathcal{B}$. We shall assume that the body is undeformed and stress-free in the reference configuration. Let $\mathbf{X} \in \kappa_R(\mathcal{B})$ be the position of a particle in the reference configuration. A one-to-one mapping $\boldsymbol{\chi}$ referred to as the motion of the body, relates the position of a particle in the deformed configuration, $\mathbf{x}$ to its position in the reference configuration, $\mathbf{X}$ through

$$\mathbf{x} = \boldsymbol{\chi}(\mathbf{X}). \tag{4.1}$$

The displacement is defined by

$$\mathbf{u} = \mathbf{x} - \mathbf{X}, \tag{4.2}$$

and the deformation gradient associated with the motion is defined as

$$\mathbf{F} = \frac{\partial \mathbf{x}}{\partial \mathbf{X}} = \mathbf{I} + \frac{\partial \mathbf{u}}{\partial \mathbf{X}}. \tag{4.3}$$

The left and the right Cauchy-Green tensors are defined through

$$\mathbf{B} = \mathbf{F}\mathbf{F}^{\mathrm{T}}, \tag{4.4}$$

$$\mathbf{C} = \mathbf{F}^{\mathrm{T}}\mathbf{F}, \tag{4.5}$$

and the Green-St. Venant strain is defined as

$$\mathbf{E} = \frac{1}{2}\left(\mathbf{C} - \mathbf{I}\right). \tag{4.6}$$

If $\max_{\forall \mathbf{X}} || \frac{\partial \mathbf{u}}{\partial \mathbf{X}} || = \mathcal{O}(\delta), \ \ \delta << 1$, the linearized strain $\boldsymbol{\epsilon} \approx \mathbf{E}$ is defined as

$$\boldsymbol{\epsilon} = \frac{1}{2} \left(\frac{\partial \mathbf{u}}{\partial \mathbf{x}} + \left(\frac{\partial \mathbf{u}}{\partial \mathbf{x}} \right)^{\mathrm{T}} \right). \tag{4.7}$$

Let the body be comprised of an elastic material reinforced by two families of fibers whose directions in the reference configuration are given by the unit vectors $\mathbf{M}_1$ and $\mathbf{M}_2$. Let 2ϕ denote the angle between the two families of fibers in the reference configuration. For such a material, stored energy function W can be defined as a function of the following form ([134])

$$W = W(I_1, I_2, I_3, I_4, I_5, I_6, I_7, I_8, cos^2(2\phi)), \tag{4.8}$$

where $I_1 = tr(\mathbf{C})$,$I_2 = \frac{1}{2}(I_1^2 - tr(\mathbf{C}^2))$, $I_3 = det(\mathbf{C})$, $I_4 = \mathbf{M}_1.\mathbf{C}\mathbf{M}_1$, $I_5 = \mathbf{M}_1.\mathbf{C}^2\mathbf{M}_1$, $I_6 = \mathbf{M}_2.\mathbf{C}\mathbf{M}_2$, $I_7 = \mathbf{M}_2.\mathbf{C}^2\mathbf{M}_2$ and $I_8 = (\mathbf{M}_1.\mathbf{M}_2)\mathbf{M}_1.\mathbf{C}\mathbf{M}_2$. $\mathbf{A}.\mathbf{H}$ represents the inner product between $\mathbf{A}$ and $\mathbf{H}$. If the fibers are mechanically equivalent, the material will exhibit orthotropic symmetry with respect to the planes whose normals are the angular bisectors of the angles between $\mathbf{M}_1$ and $\mathbf{M}_2$, and the stored energy function must be symmetric with respect to the invariant pairs I_4 and I_6, and I_5 and I_7. We shall consider a material that is orthotropic and incompressible[2] ($\det(\mathbf{F}) = 1$), and drop the dependence of the stored energy on I_3. The Cauchy stress is now given by

$$\mathbf{T} = -p\mathbf{I} + 2\mathbf{F}\frac{\partial W}{\partial \mathbf{C}}\mathbf{F}^{\mathrm{T}}, \tag{4.9}$$

where p is the Lagrange multiplier introduced to account for the incompressibility of the material. The first Piola-Kirchhoff stress is defined as

$$\mathbf{P} = \det(\mathbf{F})\mathbf{T}\mathbf{F}^{-\mathrm{T}} = \mathbf{T}\mathbf{F}^{-\mathrm{T}}. \tag{4.10}$$

In order to reduce the complexity of the form of the stored energy function, a simplified form given

[2]Most polymeric materials and biological tissues are often assumed to be incompressible, but there is evidence that implies that these materials are compressible ([135], [136], [137]).

by the following equation is often assumed ([138], [131])

$$W = W(I_1, I_4, I_6). \tag{4.11}$$

A further simplification is made by splitting the stored energy function into isotropic and anisotropic parts such that

$$W = W_{iso}(I_1) + W_{ani}(I_4, I_6). \tag{4.12}$$

The first constitutive relation we consider for analysis in this paper is based on a stored energy function of the form given by

$$W = c_1 (I_1 - 3) + c_2 \left((I_4 - 1)^2 + (I_6 - 1)^2 \right). \tag{4.13}$$

This constitutive relation which is based on a partial set of invariants is often referred to as the "standard fiber-reinforcing" model ([131]). In this paper, we shall refer to this constitutive relation as the "abridged" orthotropic (AO) constitutive relation. [77] showed that the linearization of this constitutive relation leads to a constitutive expression that does not correspond to the linearized theory of elasticity for a body reinforced by two families of fibers. The popular constitutive relation due to [72] suffers from the same shortcoming and, thus, is not really suitable for modeling the nonlinear response of orthotropic elastic bodies. Of course, a proper constitutive relation to describe the response of orthotropic linearized elastic bodies requires knowledge of nine material moduli. One has to navigate the delicate choice of picking a sufficiently simple constitutive relation that can yet capture the response characteristics exhibited by the body being modeled. [79] further showed that such a simplification leads to constitutive relations that display a counter-intuitive stiffer response in the out-of-plane direction compared to directions in the plane of the fibers. Figure 4.1a shows the Young's moduli for the linearized version of the abridged constitutive relation along the directions that are normal to the planes of symmetry, where XY-plane is the plane con-

taining the fibers. We can observe the out-of-plane Young's modulus (E_z) to be higher than at least one of the in-plane moduli for most of the fiber angles. In addition, it was shown by [77] that the inclusion of all fiber related invariants is necessary to represent an orthotropic material. Therefore, we consider a modification of the abridged orthotropic constitutive relation that is compatible with the linear theory (see [80]), whose stored energy function is given by

$$\begin{aligned} W =& c_1 (I_1 - 3) + c_2 \left((I_4 - 1)^2 + (I_6 - 1)^2 \right) + c_3 \left(I_8 - I_8^0 \right)^2 \\ &+ c_4 (I_4 + I_6 - 2) \left(I_8 - I_8^0 \right) + c_5 (I_4 I_6 - I_4 - I_6 + 1) \\ &+ c_6 (I_5 + I_7 - 2I_4 - 2I_6 + 2), \end{aligned} \tag{4.14}$$

where $I_8^0 = (\mathbf{M}_1.\mathbf{M}_2)^2$. We refer to this relation as the "Extended"[3] orthotropic (EO) constitutive relation[4]. Figure 4.1b shows the Young's moduli for this constitutive relation along the normals to the planes of symmetry.

[3]This constitutive relation reduces to the constitutive equation corresponding to the linearized elastic orthotropic material ([80]). In no way do we mean this to be the only possible constitutive relation that agrees with linearized elasticity.

[4]The invariant I_2 is not included in the stored energy function in this paper as its inclusion is not necessary to produce a constitutive relation that agrees with linearized elasticity. Secondly, we wanted to keep the number of material constants to a minimum. However, inclusion of I_2 may be important to represent the experimentally observed stress-strain response of a material ([139]).

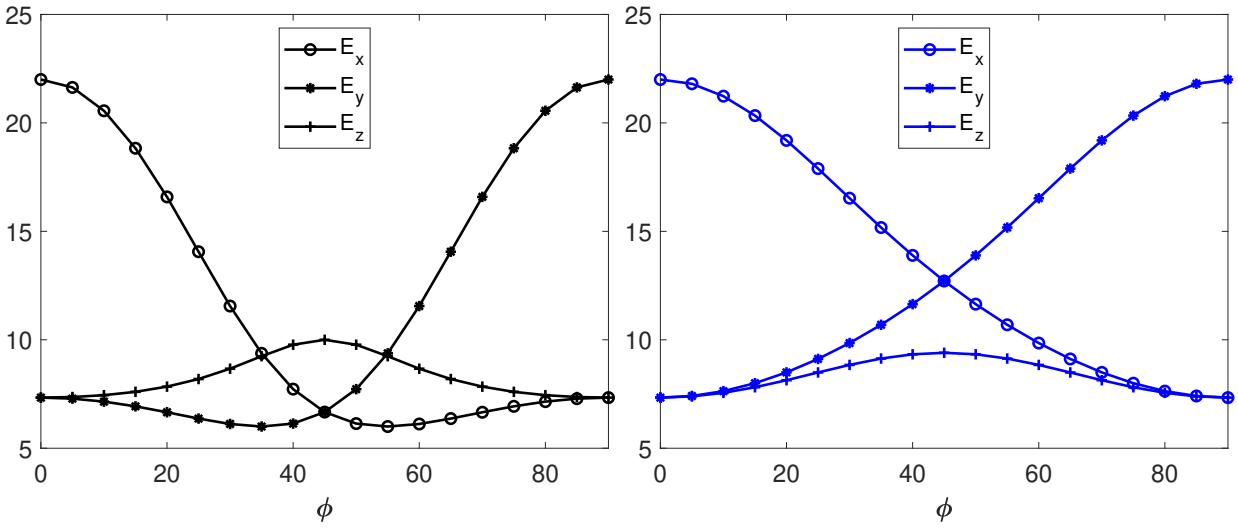

Figure 4.1: Young's modulus vs. fiber angle under small deformations for the (a) AO constitutive relation with $c_2 = 1$, (b) EO constitutive relation with $(c_2, c_3, c_4, c_5, c_6) = (0.1, 0.1, 0.1, 0.1, 0.7)$ when the angular bisectors of the fibers are along the X and the Y axes. We notice that E_y (or E_x) is qualitatively different in that it is non-monotone for the AO constitutive relation and monotone for the EO constitutive relation.

In order to compare the results for orthotropic materials with that of isotropic materials, we shall consider the incompressible neoHookean (neo) form given by

$$W = c_1(I_1 - 3). \tag{4.15}$$

To recapitulate, the Cauchy stress associated with the above constitutive relations is given by

$$\mathbf{T}_{\text{AO}} = -p\mathbf{I} + 2c_1\mathbf{B} + 4c_2(I_4 - 1)\mathbf{FM}_1 \otimes \mathbf{FM}_1 + 4c_2(I_6 - 1)\mathbf{FM}_2 \otimes \mathbf{FM}_2, \tag{4.16}$$

$$\begin{aligned}\mathbf{T}_{\text{EO}} = -p\mathbf{I} + 2c_1\mathbf{B} + \left(4c_2(I_4 - 1) + 2c_4\left(I_8 - I_8^0\right) + 2c_5\left(I_6 - 1\right) - 4c_6\right)\mathbf{FM}_1 \otimes \mathbf{FM}_1 \\ + \left(4c_2(I_6 - 1) + 2c_4\left(I_8 - I_8^0\right) + 2c_5\left(I_4 - 1\right) - 4c_6\right)\mathbf{FM}_2 \otimes \mathbf{FM}_2 \\ +2c_6\left(\mathbf{BFM}_1 \otimes \mathbf{FM}_1 + \mathbf{FM}_1 \otimes \mathbf{BFM}_1 + \mathbf{BFM}_2 \otimes \mathbf{FM}_2 + \mathbf{FM}_2 \otimes \mathbf{BFM}_2\right), \\ +\cos(2\phi)\left(c_4\left(I_4 + I_6 - 2\right) + 2c_3\left(I_8 - I_8^0\right)\right)\left(\mathbf{FM}_1 \otimes \mathbf{FM}_2 + \mathbf{FM}_2 \otimes \mathbf{FM}_1\right)\end{aligned} \tag{4.17}$$

$$\mathbf{T}_{\text{neo}} = -p\mathbf{I} + 2c_1\mathbf{B}. \tag{4.18}$$

4.2.2 Boundary value problems studied

Consider a thin square sheet of side $2L$ under a state of plane stress in the XY-plane with a small circular hole of radius r at its center. In this paper, we confine our attention to a problem where the bisectors of the fibers are aligned with the X and the Y axes. Under this restriction, the material has reflectional symmetry with respect to XY, YZ and XZ planes. Let $u = u(X, Y)$ and $v = v(X, Y)$ be the components of the displacement field along the X-axis and the Y-axis, respectively. The following form of the deformation gradient is considered

$$\mathbf{F} = \begin{bmatrix} 1 + \frac{\partial u}{\partial X} & \frac{\partial u}{\partial Y} & 0 \\ \frac{\partial v}{\partial X} & 1 + \frac{\partial v}{\partial Y} & 0 \\ 0 & 0 & \frac{1}{\left(1+\frac{\partial u}{\partial X}\right)\left(1+\frac{\partial v}{\partial Y}\right) - \frac{\partial u}{\partial Y}\frac{\partial v}{\partial X}} \end{bmatrix}, \tag{4.19}$$

which accounts for the incompressibility ($det(\mathbf{F}) = 1$) of the material. The Cauchy stress is obtained by substituting equation 4.19 in equations 4.16, 4.17 and 4.18. The Lagrange multiplier p is eliminated from the Cauchy stress using the condition that $\text{T}_{\text{zz}} = 0$. The first Piola-Kirchhoff stress is calculated using equation 4.10.

4.2.2.1 Boundary conditions

Three problems are considered for analysis in this paper. In the first problem, an equibiaxial displacement is applied to the square sheet with a hole. The boundary conditions are given by

$$\{u(L,Y) = u_0 = -u(-L,Y)\} \text{ and } P_{YX}(\pm L, Y) = 0, \tag{4.20}$$

$$\{v(X,L) = u_0 = -v(X,-L)\} \text{ and } P_{XY}(X, \pm L) = 0, \tag{4.21}$$

where the center of the sheet coincides with the origin of the coordinate system. In the second problem, a uniaxial displacement/traction along the X-axis is applied at the right and the left edge of the square sheet. This is given by

$$\{u(L,Y) = u_0 \quad \text{or } P_{XX}(L,Y) = P_0\} \text{ and } P_{YX}(L,Y) = 0, \tag{4.22}$$

$$\{u(-L,Y) = -u_0 \quad \text{or } P_{XX}(-L,Y) = -P_0\} \text{ and } P_{YX}(-L,Y) = 0, \tag{4.23}$$

The top and the bottom surfaces of the sheet whose normals are in the Y-direction are assumed to be traction free for the uniaxial problem. This boundary condition is given by

$$\mathbf{PN} = \mathbf{0} \text{ at } Y = \pm L, \quad \forall X, \tag{4.24}$$

where $\mathbf{N}$ is the undeformed unit normal to the surface. In the third problem, the sheet is fixed at the top and the bottom surfaces given by

$$v(X, \pm L) = 0 \text{ and } P_{XY}(X, \pm L) = 0, \tag{4.25}$$

and the left and the right edge are displaced according to the boundary conditions in equations 4.22, 4.23. This is a pure shear deformation problem. In all the three problems, a traction free boundary condition is assumed at the boundary of the hole. The geometry, the boundary conditions and

the material orientations described above allows one to consider only a quarter of the sheet for analysis. The following boundary conditions are applied for the quarter sheet considered

$$\{u(0,Y)=0 \text{ and } P_{YX}(0,Y)=0\} \quad \text{and} \quad \{v(X,0)=0 \text{ and } P_{XY}(X,0)=0\}. \tag{4.26}$$

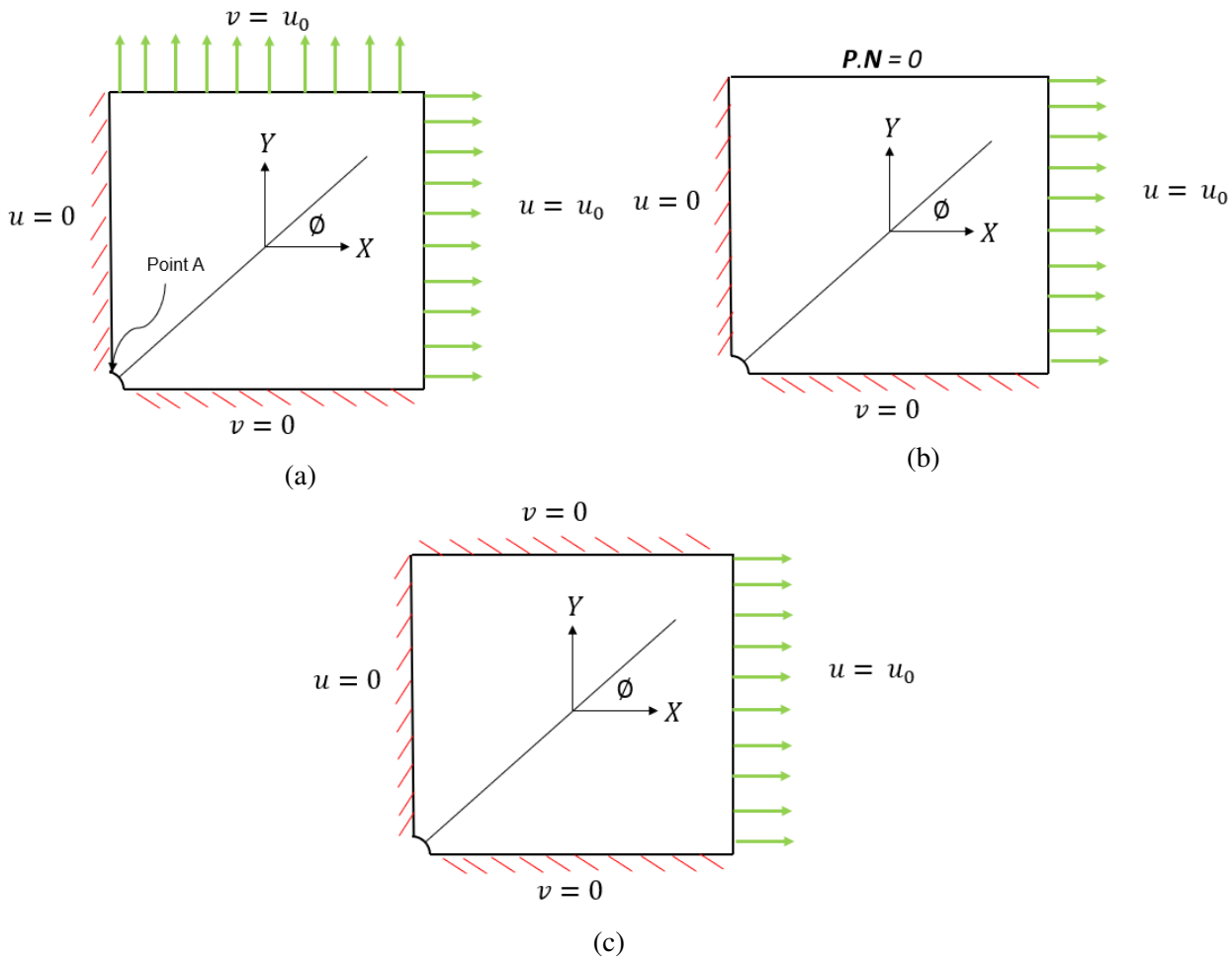

Figure 4.2: Schematic showing the three boundary value problems studied (a) equibiaxial extension, (b) uniaxial extension (c) pure shear deformation. ϕ represents the angle between the fiber (diagonal line) and the X-axis in the reference configuration.

4.2.2.2 *Non-dimensionalization and governing equations*

The equations are non-dimensionalized using the following definitions

$$\overline{X} = \frac{X}{L}, \quad \overline{Y} = \frac{Y}{L}, \quad \overline{u} = \frac{u}{L}, \quad \overline{v} = \frac{v}{L}, \quad \overline{\mathbf{T}} = \frac{\mathbf{T}}{c_1}. \tag{4.27}$$

The non-dimensionalized form of the governing equations are now given by

$$\overline{\text{Div}}(\overline{\mathbf{P}}) = 0. \tag{4.28}$$

which in the component form is

$$\frac{\partial \overline{P}_{XX}}{\partial \overline{X}} + \frac{\partial \overline{P}_{XY}}{\partial \overline{Y}} = 0, \tag{4.29}$$

$$\frac{\partial \overline{P}_{YX}}{\partial \overline{X}} + \frac{\partial \overline{P}_{YY}}{\partial \overline{Y}} = 0. \tag{4.30}$$

We will drop the bar in the previous equations for convenience. The governing equations are solved using the finite element method in COMSOL Multiphysics (Mathematics module). The relative tolerance is set to 10^{-6} for the simulations. Quadratic triangular elements are used with a very high refinement of the mesh close to the hole. The stress concentration factor (SCF) at the hole is defined as the ratio of the hoop stress along the hole to the nominal[5] T_{xx}. The hoop stress is calculated as follows: The unit vector along the tangent to the deformed edge of the hole is computed using the following equation

$$\mathbf{t}_d = \frac{\mathbf{F}\mathbf{t}_u}{\sqrt{\mathbf{t}_u.\mathbf{C}\mathbf{t}_u}}, \tag{4.31}$$

where $\mathbf{t}_u$ is the unit vector along the tangent to the edge of the hole in the reference configuration and is given by

$$\mathbf{t}_u = -\frac{Y}{\sqrt{(X^2+Y^2)}}\mathbf{E}_X + \frac{X}{\sqrt{(X^2+Y^2)}}\mathbf{E}_Y, \tag{4.32}$$

[5]By "nominal", we refer to the values at a point far from the hole.

where $\mathbf{E}_X$ and $\mathbf{E}_Y$ are the unit vectors along the X and Y axes respectively. The hoop stress is computed using the equation below

$$\mathrm{T_{tt}} = \mathbf{t}_d.\mathbf{T}\mathbf{t}_d. \tag{4.33}$$

Finally, we define an angle Θ along the hole to be $\Theta = \tan^{-1}(Y/X)$. To verify the accuracy of the numerical results, we compared the numerical solution for the abridged constitutive relation with the analytical solution for its linearized form with a central circular hole in an infinite sheet loaded uniaxially. This is shown in Figure 4.3. The analytical solution under uniaxial tension for an anisotropic sheet with a circular hole is given by [140]. For the numerical simulation, a non-dimensionalized hole radius of 0.002 is used. We can see that the stress concentration factor at $X = 0, Y = 0.002$ (we call this point 'A'. we use 'B' for representing a point far away from the hole) can be higher or lower than the stress concentration factor in an isotropic linear elastic material (which is 3). Unlike the case of an isotropic material, the maximum stress, which depends on the fiber angle, does not always occur at point A. We will show later that such a phenomenon occurs under large deformations as well.

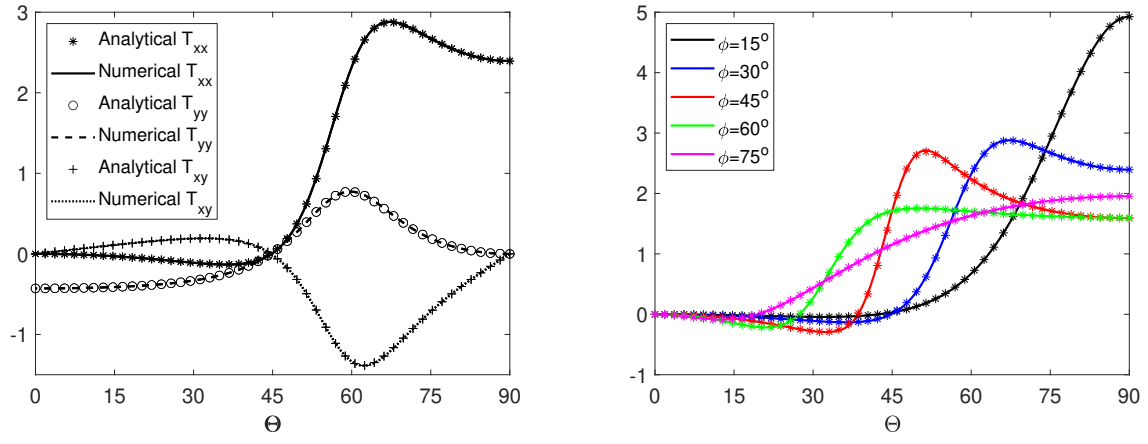

(a) (b)

Figure 4.3: Figure (a) shows the ratio of the components of $\mathbf{T}$ at the hole to nominal $\mathrm{T_{xx}}$ for $\phi = 30^o$ for $\lambda = 1 + 10^{-6}$. Figure (b) shows the comparison of the ratio of $\mathrm{T_{xx}}$ at hole to $\mathrm{T_{xx}}$ at B for different fiber angles for $\lambda = 1 + 10^{-6}$. Solid line represents the numerical solution and asterisk represents the analytical solution. Parameter used for the AO constitutive relation is $c_2 = 10$. λ is the nominal stretch.

Figure 4.4 shows the stress concentration factor for different material parameters for the linearized version of the abridged constitutive relation. As the value of c_2 increases, the stress concentration factor differs from the isotropic linearized elastic case. Additionally, we can observe that the peak stress concentration factor does not always occur at point A as c_2 increases. This effect is more pronounced at larger values of c_2 for certain fiber angles (see Figure 4.4b, Figure 4.4c). It can be seen in Figure 4.4d that for the fiber angles between 30^o and 80^o, the stress concentration factor at point A decreases with an increase in parameter c_2.

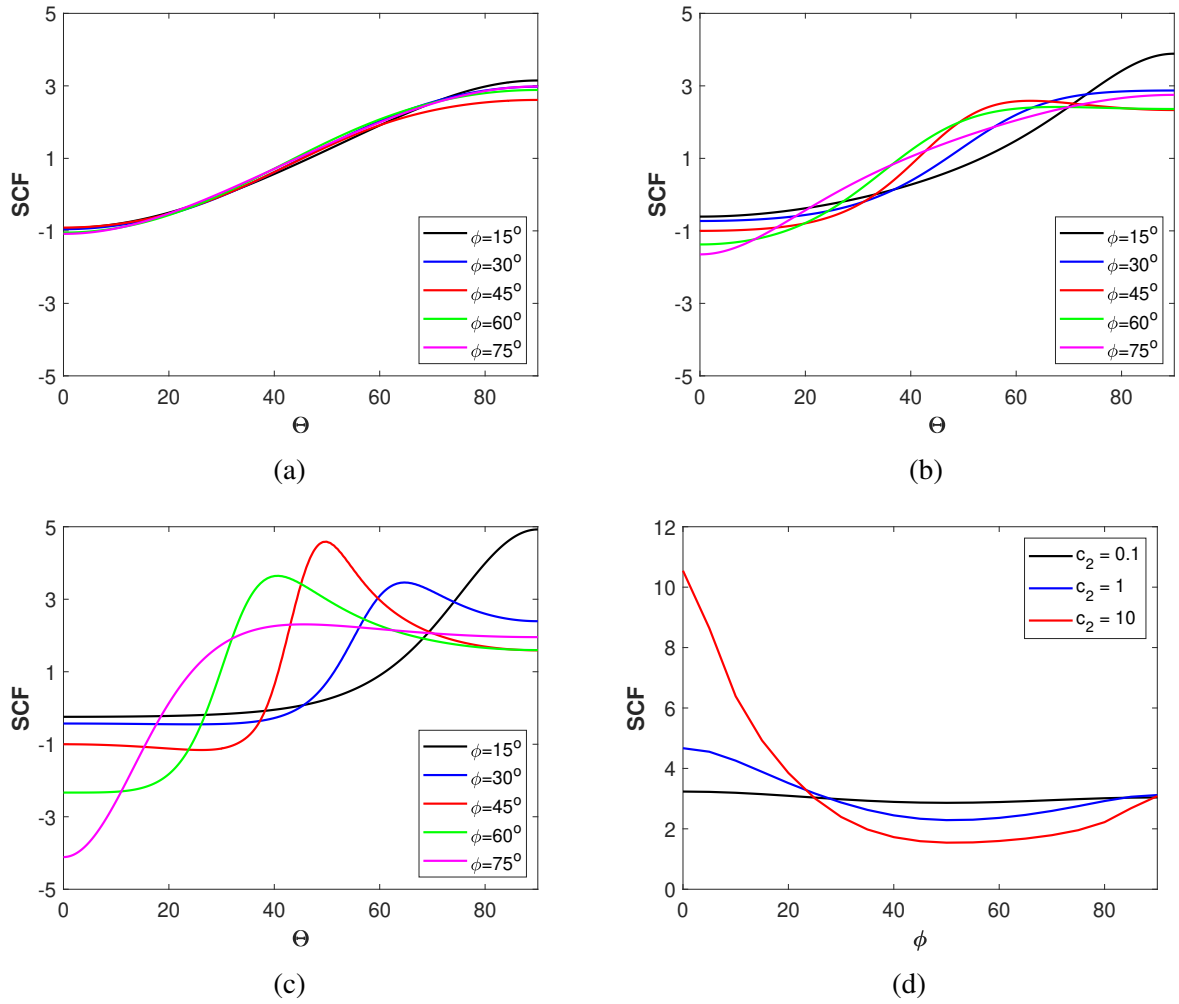

Figure 4.4: SCF at hole for (a) $c_2 = 0.1$, (b) $c_2 = 1$, (c) $c_2 = 10$. Figure (d) shows SCF at A for different fiber angles and $c_2 = 0.1, 1, 10$ for the abridged orthotropic constitutive relation.

Mesh size for the simulations is chosen after preforming a mesh convergence study. The smallest element size is of the order of 10^{-8} while the largest element size is 0.1. Figure 4.5 shows a mesh convergence plot for the stress concentration factor at point A and along the hole for different number of elements for the abridged constitutive relation with a fiber angle of 0^o and $c_2 = 1$ under uniaxial extension. It can be seen that as the nominal stretch along the X-direction increases a larger number of elements are needed for a converged solution. This is due to an increase in the gradient of the stress near the hole.

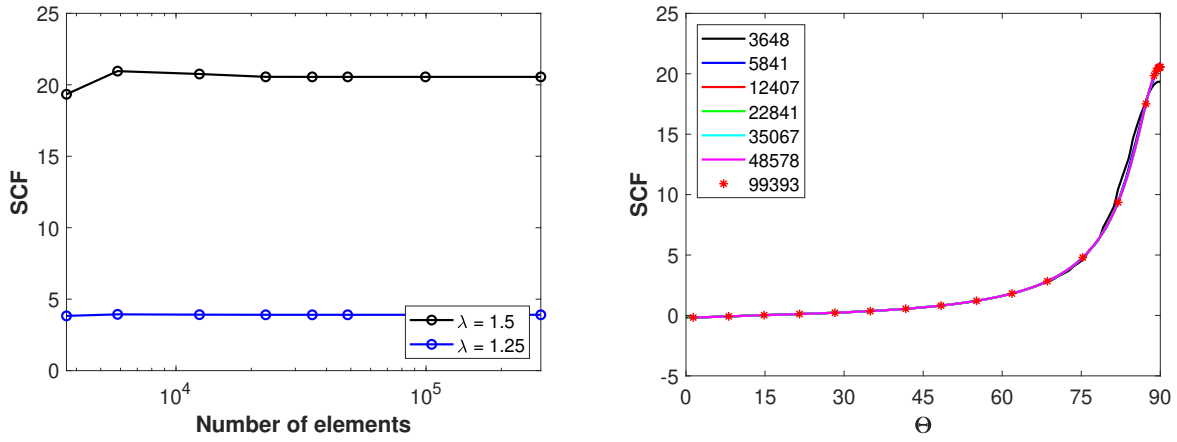

(a) (b)

Figure 4.5: Mesh convergence plot for uniaxial extension, (a) Stress concentration factor at point A and (b) SCF at hole for different number of elements. Parameters used for the AO constitutive relation are $c_2 = 1$ and $\phi = 0^o$.

Finally in Figure 4.6 we show the stress concentration factor for the neoHookean model at point A and along the hole at various nominal stretches (λ) for equibiaxial, uniaxial and pure shear problems. The maximum of the stress concentration factor occurs at point A under uniaxial and pure shear deformations. The stress concentration factor is a constant along the boundary of the hole under equibiaxial extension for the neoHookean model, which is the expected behavior of an isotropic constitutive relation.

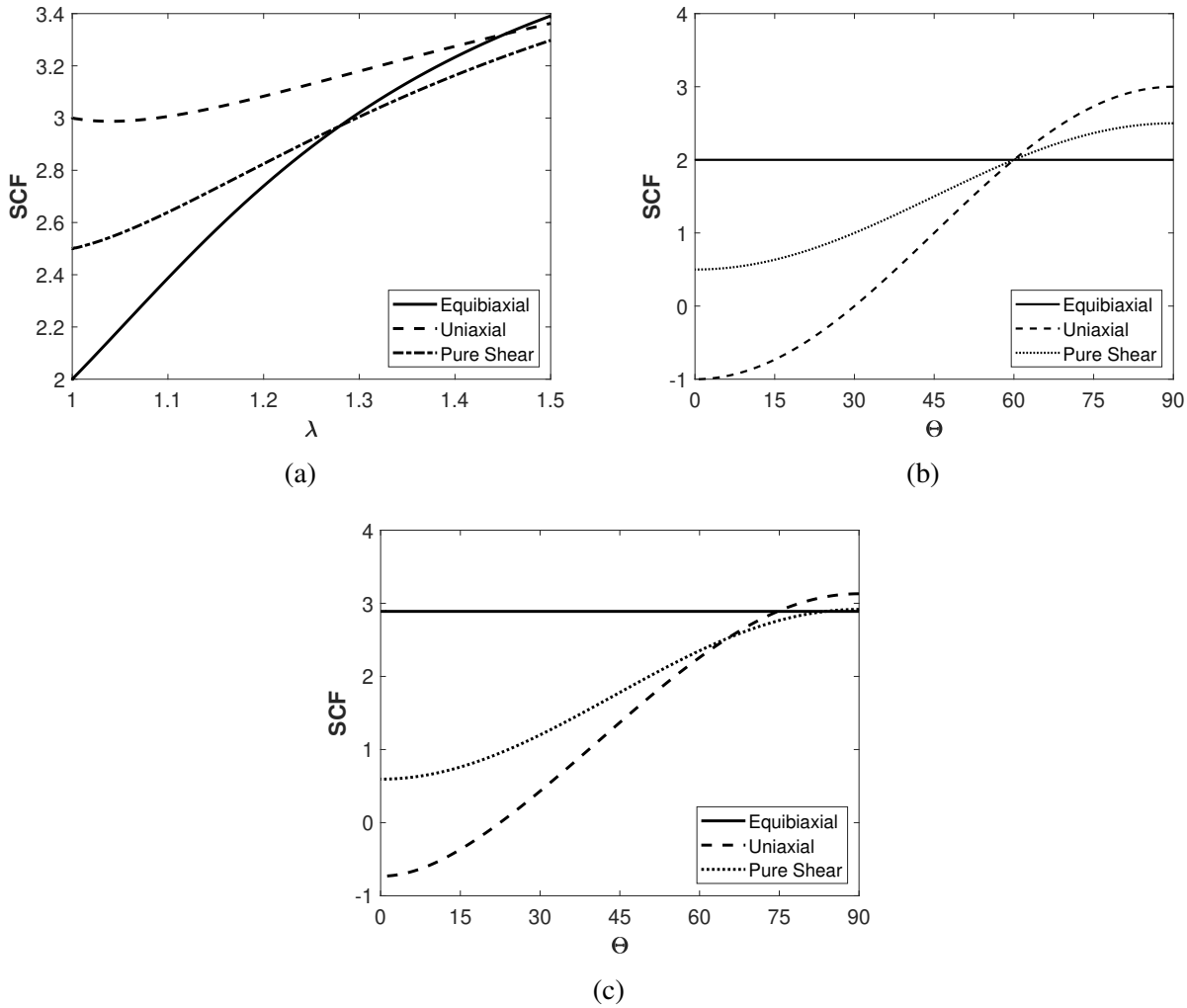

Figure 4.6: Figure (a) shows the variation of the stress concentration factor at A with stretch, Figures (b) and (c) show the SCF along the hole at $\lambda = 1 + 10^{-6}$ and $\lambda = 1.25$ for the neoHookean model under equibiaxial, uniaxial and pure shear deformations.

4.3 Results and discussion

For a given value of the parameter c_2 (= c_2^{AO}) of the abridged orthotropic constitutive relation, the material parameters of the extended orthotropic constitutive relation are chosen as follows: $c_2, c_3, c_4, c_5 = 0.1c_2^{\text{AO}}$ and $c_6 = 0.7c_2^{\text{AO}}$. The two constitutive relations produce a similar biaxial stress-stretch response when the material parameters are varied in the above manner. In sections 3.1-3.3, we discuss the results for the abridged orthotropic constitutive relation with $c_2 = 1$

and the extended orthotropic constitutive relation with $(c_2, c_3, c_4, c_5, c_6) = (0.1, 0.1, 0.1, 0.1, 0.7)$, $(0.2, 0.2, 0.2, 0.2, 0.8)$. As shown in Figure 4.7, the two constitutive relations have a comparable biaxial stress-deformation response in the absence of a hole.

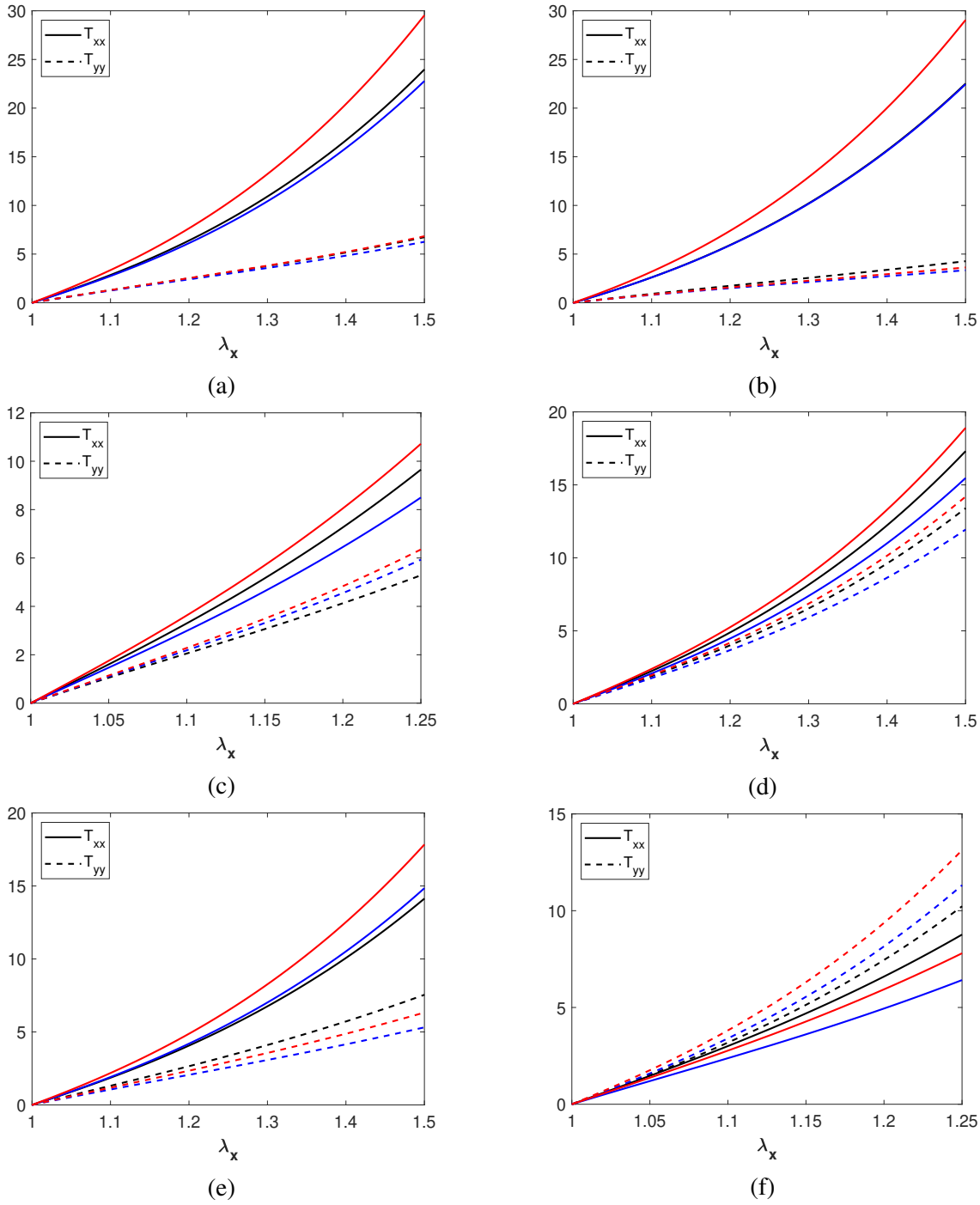

Figure 4.7: Biaxial extension behavior of the AO and the EO constitutive relations without a hole. Cauchy stress vs stretch for (a) equibiaxial extension, $\phi = 20^o$, (b) biaxial extension with the ratio of boundary displacements u:v = 2:1, $\phi = 20^o$ (c) biaxial extension with the ratio of boundary displacement u:v = 1:2, $\phi = 20^o$ (d) equibiaxial extension, $\phi = 40^o$, (e) biaxial extension with the ratio of boundary displacements u:v = 2:1, $\phi = 40^o$ (f) biaxial extension with the ratio of boundary displacements u:v = 1:2, $\phi = 40^o$. Black lines show the response of the abridged orthotropic constitutive relation with $c_2 = 1$. Red and blue lines show the response of the extended orthotropic constitutive relation with $(c_2, c_3, c_4, c_5, c_6) = (0.2, 0.2, 0.2, 0.2, 0.8)$ and $(c_2, c_3, c_4, c_5, c_6) = (0.1, 0.1, 0.1, 0.1, 0.7)$, respectively.

4.3.1 Influence of hole size on stress concentration

The influence of the radius of the hole on the stress concentration factor under uniaxial extension for the abridged orthotropic constitutive relation is shown in Figure 4.8. As shown in Figure 4.8a, the stress concentration factor at the point A remains constant for sufficiently small holes with the radius of the hole below 0.006 for a nominal stretch up to 1.5. As the hole radius increases, the stress concentration factor decreases with the effect of the hole radius being more prominent at larger nominal stretches. In case of the neoHookean material, the stress concentration factor is unaffected until a hole radius of 0.2 for the nominal stretch up to 1.5. Addition of anisotropic terms results in larger stresses and stress gradients near the hole causing a more pronounced effect of the discontinuities, which in this case is a circular hole. This effect is more noticeable at fiber angles where the stress concentration factor is high near the hole as shown in Figure 4.8c compared to the fiber angles at which the SCF is lower. Similar results were obtained for the extended orthotropic constitutive relation as shown in Figure 4.8b and Figure 4.8d. Following this analysis, we consider a hole of radius 0.002 for the rest of the paper.

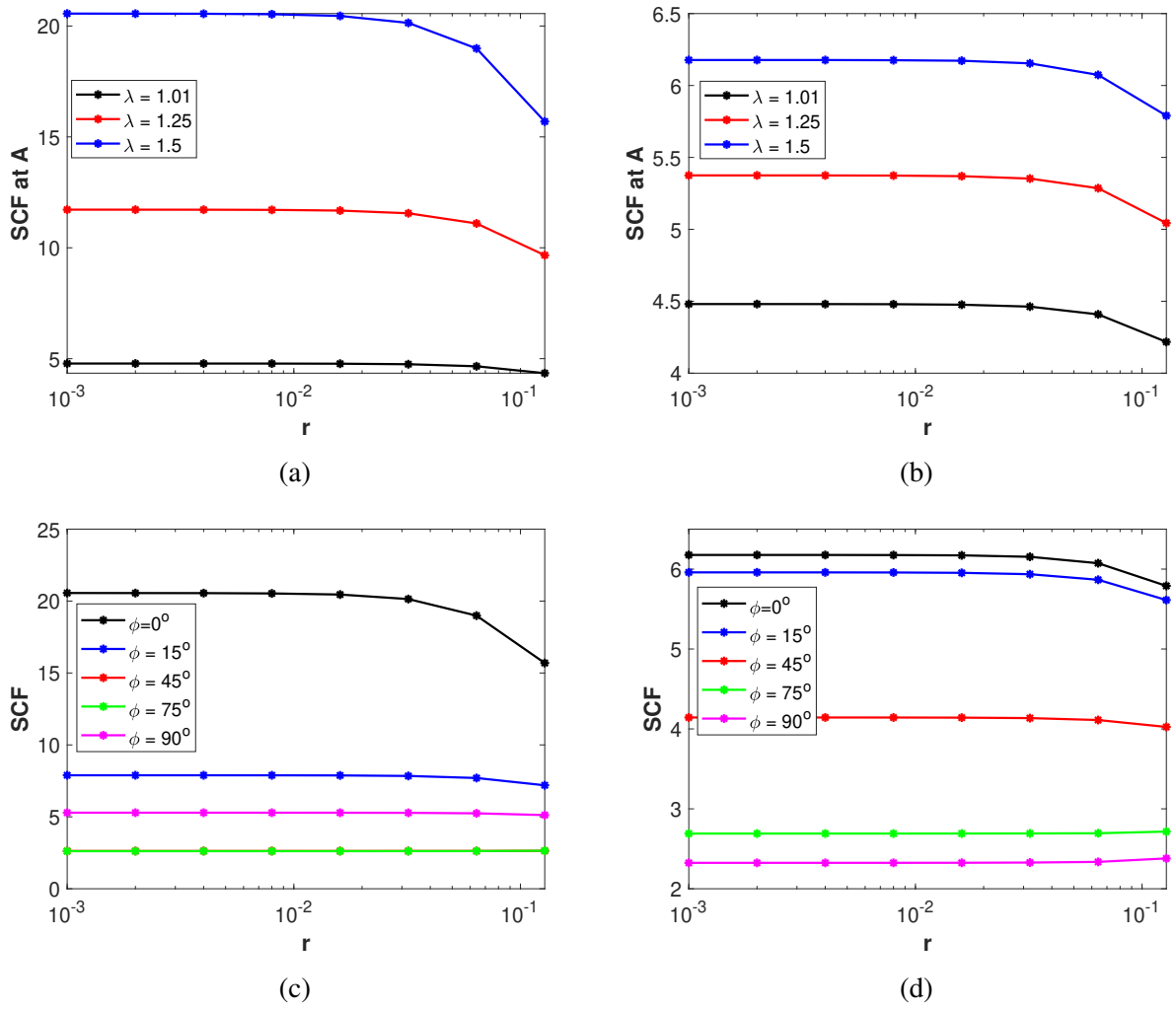

Figure 4.8: (a) SCF vs. hole radius at different nominal stretches for the AO constitutive relation, (b) SCF vs. hole radius at different nominal stretches for the EO constitutive relation with $(c_2, c_3, c_4, c_5, c_6) = (0.1, 0.1, 0.1, 0.1, 0.7)$, (c) SCF vs. hole radius for different fiber angles at $\lambda = 1.5$ for the AO constitutive relation, (d) SCF vs. hole radius for different fiber angles at $\lambda = 1.5$ for the EO constitutive relation.

4.3.2 Stress distribution at the hole for the abridged and the extended orthotropic constitutive relations

Figure 4.9 shows the variation of the SCF at point A with stretch for two different fiber angles under equibiaxial extension. For both the fiber angles and the constitutive relations, the stress concentration factor increases with increasing nominal stretch. Small strain SCF differs between the

two constitutive relations with the extended orthotropic constitutive relation showing higher stress concentration factors at both the fiber angles while the abridged orthotropic constitutive relation showing higher and lower SCFs at fiber angles 20^o and 40^o, respectively when compared to the SCF of the neoHookean model. We can observe from Figure 4.7 that under equibiaxial extension without a hole, the stress-stretch curve of the abridged constitutive relation is enveloped by that of the extended orthotropic constitutive relation with two different sets of material parameters studied here. Stress concentration factors, however, differ significantly between the two constitutive relations and the difference being dependent on the fiber angle.

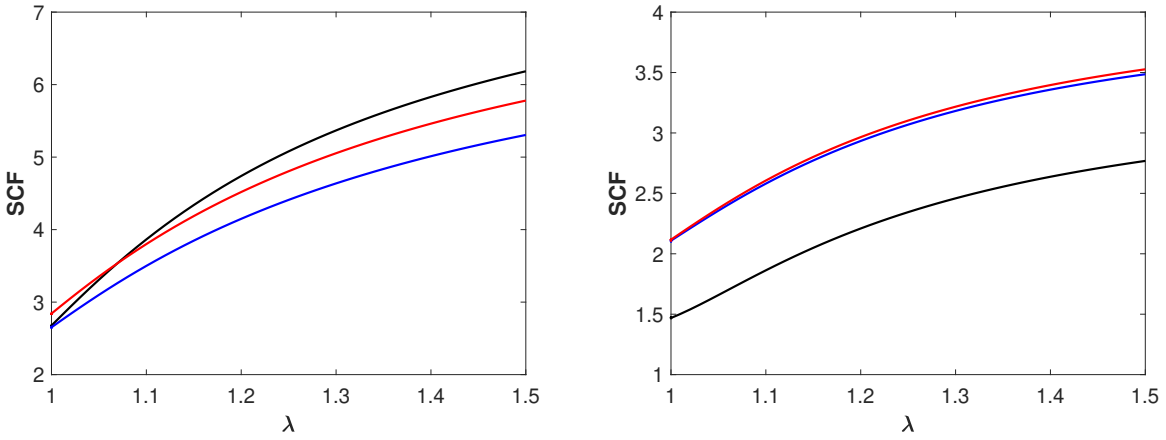

(a) (b)

Figure 4.9: Variation of the stress concentration factor at point A with stretch under equibiaxial extension for (a) ϕ = 20^o, (b) ϕ = 40^o. Black lines show the response of the abridged constitutive relation with $c_2 = 1$. Red and blue lines show the response of the extended orthotropic constitutive relation with $(c_2, c_3, c_4, c_5, c_6) = (0.2, 0.2, 0.2, 0.2, 0.8)$ and $(c_2, c_3, c_4, c_5, c_6) = (0.1, 0.1, 0.1, 0.1, 0.7)$, respectively.

A more noticeable difference between the two constitutive relations can be observed when considering the distribution of SCFs along the hole as shown in Figure 4.10. At 20^o fiber angle, both the constitutive relations show a peak stress concentration factor occurring at point A. In stark contrast, the abridged constitutive relation shows remarkably larger stress at a point other than point A

at fiber angle of 40^o. Such a difference becomes acutely important when one wants to study the initiation of the failure and, in particular, the location of possible failure initiation depending greatly on the choice of the constitutive relation. Uniaxial extension problem further demonstrates the differences between the abridged orthotropic and the extended orthotropic constitutive relations.

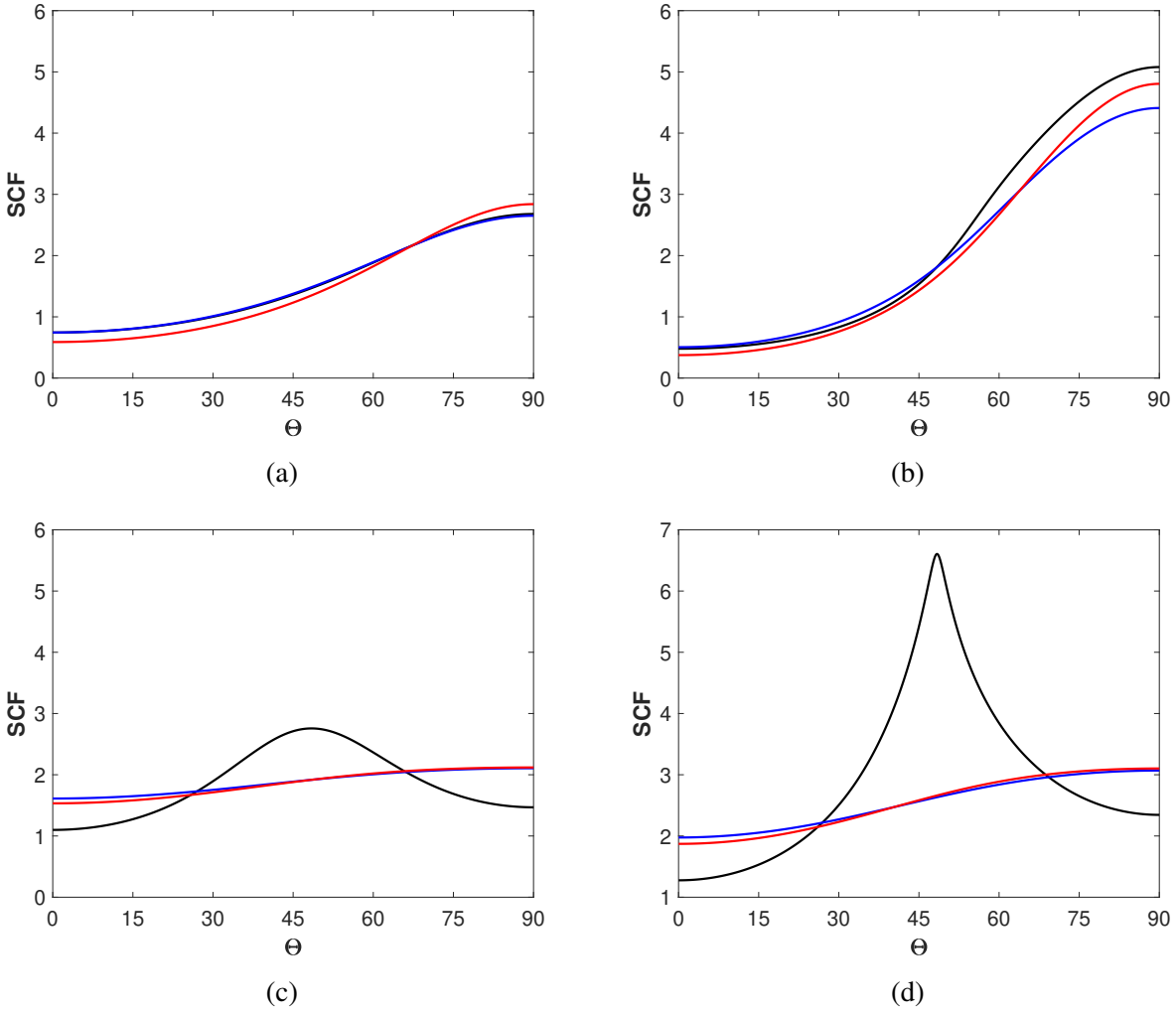

Figure 4.10: Stress concentration factor versus Θ at the hole for different constitutive relations. Figures (a), (b) show results for ϕ = 20^o and λ = 1+10^{-6} and 1.25, respectively. Figures (c), (d) show results for ϕ = 40^o and λ = 1+10^{-6} and 1.25, respectively. Black lines show the response of the abridged constitutive relation with $c_2 = 1$. Red and blue lines show the response of the extended orthotropic constitutive relation with $(c_2, c_3, c_4, c_5, c_6) = (0.2, 0.2, 0.2, 0.2, 0.8)$ and $(c_2, c_3, c_4, c_5, c_6) = (0.1, 0.1, 0.1, 0.1, 0.7)$, respectively.

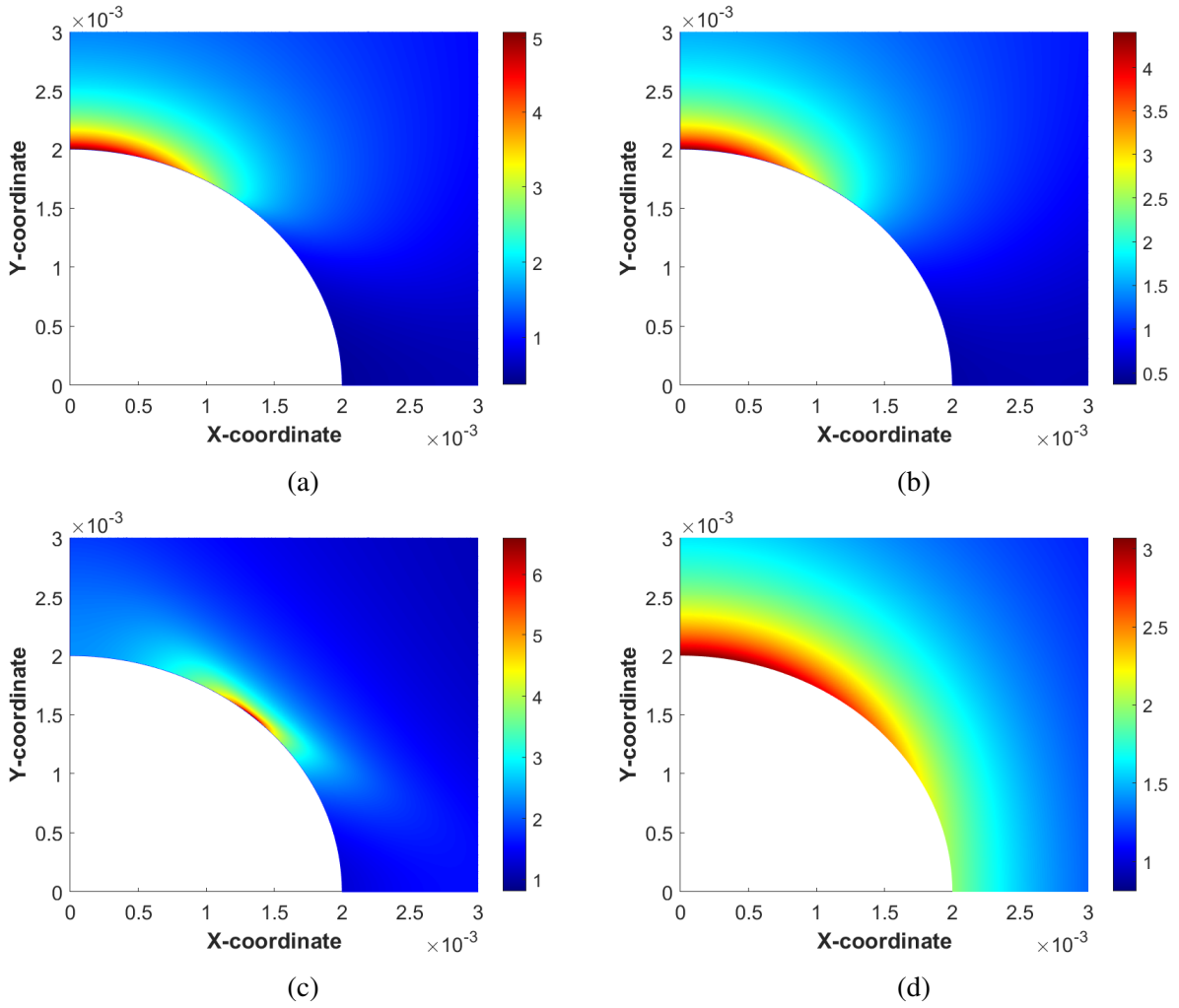

Figure 4.11: Ratio of hoop stress to nominal T_{xx} for (a) AO constitutive relation with $c_2 = 1$, $\phi = 20^o$, (b) EO constitutive relation with $(c_2, c_3, c_4, c_5, c_6) = (0.1, 0.1, 0.1, 0.1, 0.7)$, $\phi = 20^o$, (c) AO constitutive relation with $c_2 = 1$, $\phi = 40^o$, (d) EO constitutive relation with $(c_2, c_3, c_4, c_5, c_6) = (0.1, 0.1, 0.1, 0.1, 0.7)$, $\phi = 40^o$ at $\lambda = 1.25$ under equibiaxial extension.

Figure 4.12 shows the stress concentration factor at point A for the material with fiber angles 20^o and 70^o. We chose these two angles, one above 45^o and one below to show the differences between the constitutive relations under uniaxial extension. Both the constitutive relations show an increasing stress concentration factor with increasing nominal stretch for 20^o fiber angle. Unlike equibiaxial extension where both the constitutive relations show an increasing stress concentration factor at point A, the SCF decreases with nominal stretch for the abridged orthotropic constitutive

relation at a fiber angle of 70^o. The extended orthotropic constitutive relation on the other hand, shows an increasing SCF with increasing nominal stretch. One possible reason for this difference between the two constitutive relations is the marked difference in the stiffening behaviour of the two constitutive relations at different fiber angles. The extended orthotropic constitutive relation provides a much larger increase in the nominal stress with increasing nominal stretch for almost all fiber angles as shown in Figure 4.14 compared to the abridged orthotropic constitutive relation. These two constitutive relations that demonstrate a similar stress-stretch behavior under biaxial extension (refer to Figure 4.7) show notably different behavior under uniaxial extension. Such differences are only magnified when studying stress concentrations around discontinuities like holes. Finally, unlike the equibiaxial extension problem, the SCF distribution around the hole is somewhat similar for both the constitutive relations under uniaxial extension.

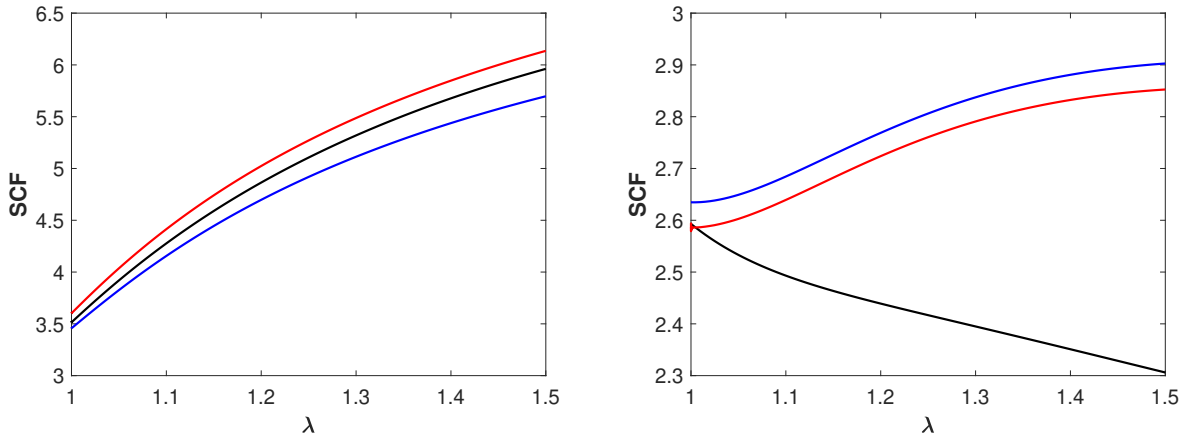

(a)

(b)

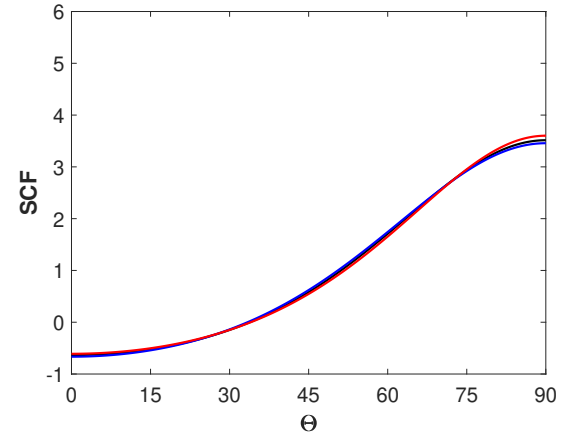

(c)

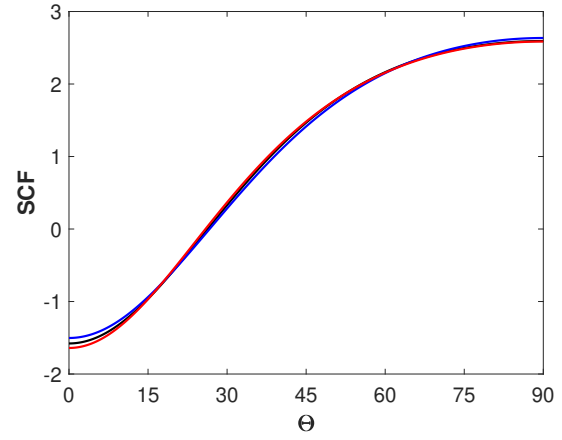

(d)

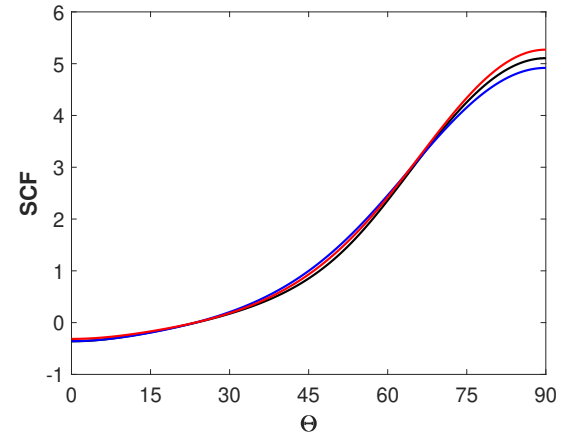

(e)

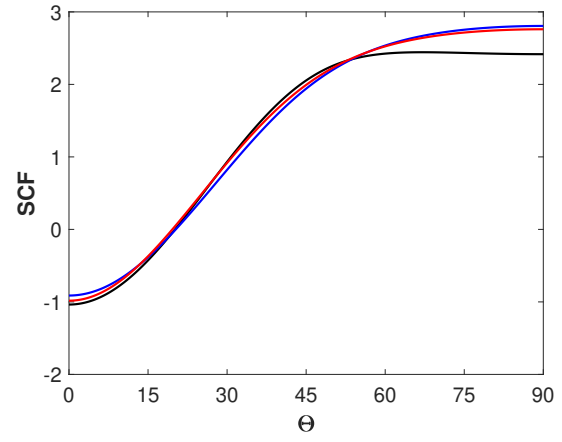

(f)

Figure 4.12: Figures (a), (b) show the variation of the stress concentration factor at point A with stretch under uniaxial extension for ϕ = 20^o and ϕ = 70^o, respectively. Figures (c), (d) show the variation of SCF along the hole at λ = 1+10^{-6} for ϕ = 20^o and ϕ = 70^o, respectively. Figures (e), (f) show the same at λ = 1.25. Black lines show the response of the abridged constitutive relation with $c_2 = 1$. Red and blue lines show the response of the extended orthotropic constitutive relation with $(c_2, c_3, c_4, c_5, c_6) = (0.2, 0.2, 0.2, 0.2, 0.8)$ and $(c_2, c_3, c_4, c_5, c_6) = (0.1, 0.1, 0.1, 0.1, 0.7)$, respectively.

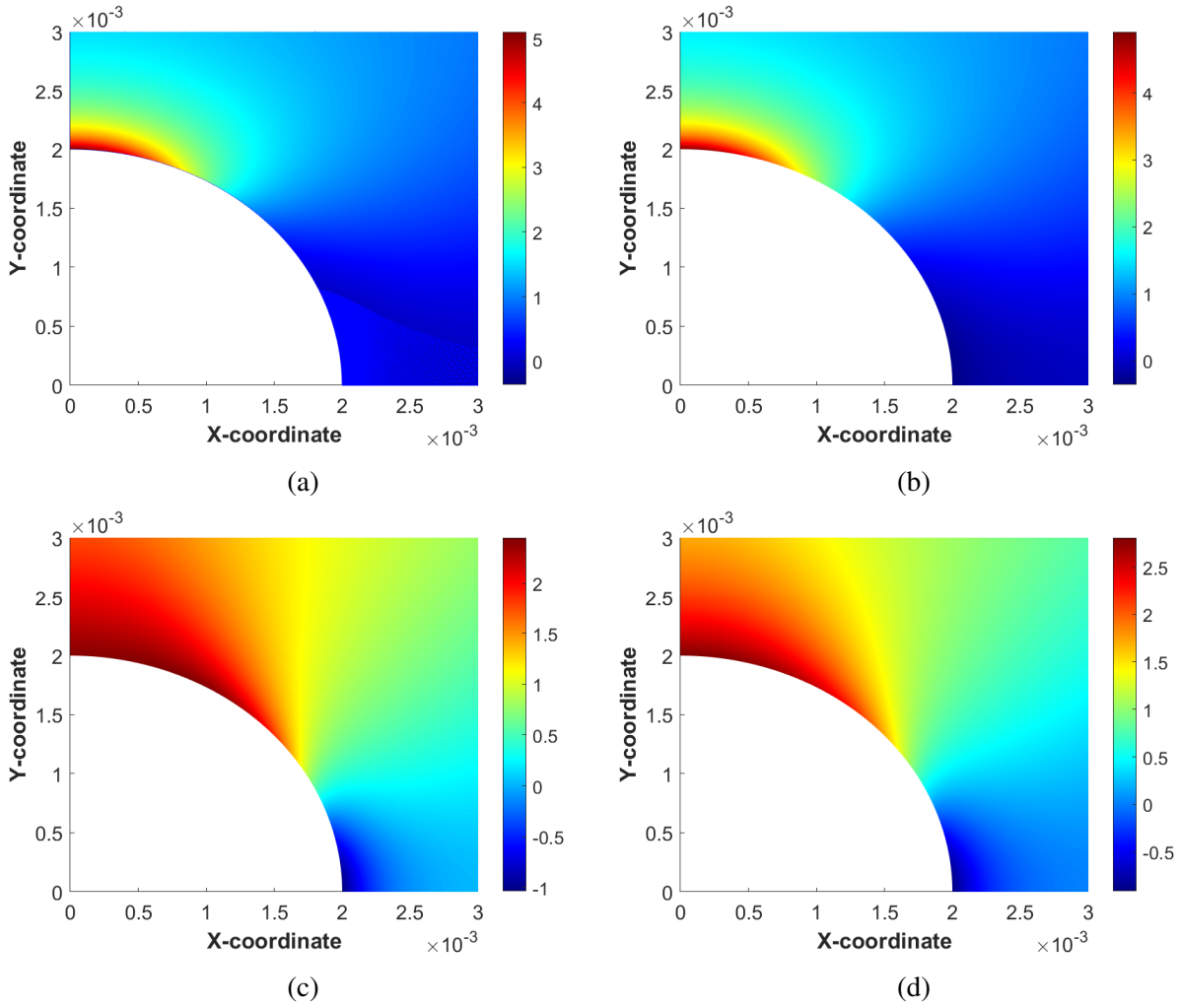

Figure 4.13: Ratio of hoop stress to nominal T_{xx} for (a) AO constitutive relation with $c_2 = 1$, $\phi = 20^o$, (b) EO constitutive relation with $(c_2, c_3, c_4, c_5, c_6) = (0.1, 0.1, 0.1, 0.1, 0.7)$, $\phi = 20^o$, (c) AO constitutive relation with $c_2 = 1$, $\phi = 70^o$, (d) EO constitutive relation with $(c_2, c_3, c_4, c_5, c_6) = (0.1, 0.1, 0.1, 0.1, 0.7)$, $\phi = 70^o$ at $\lambda = 1.25$ under uniaxial extension.

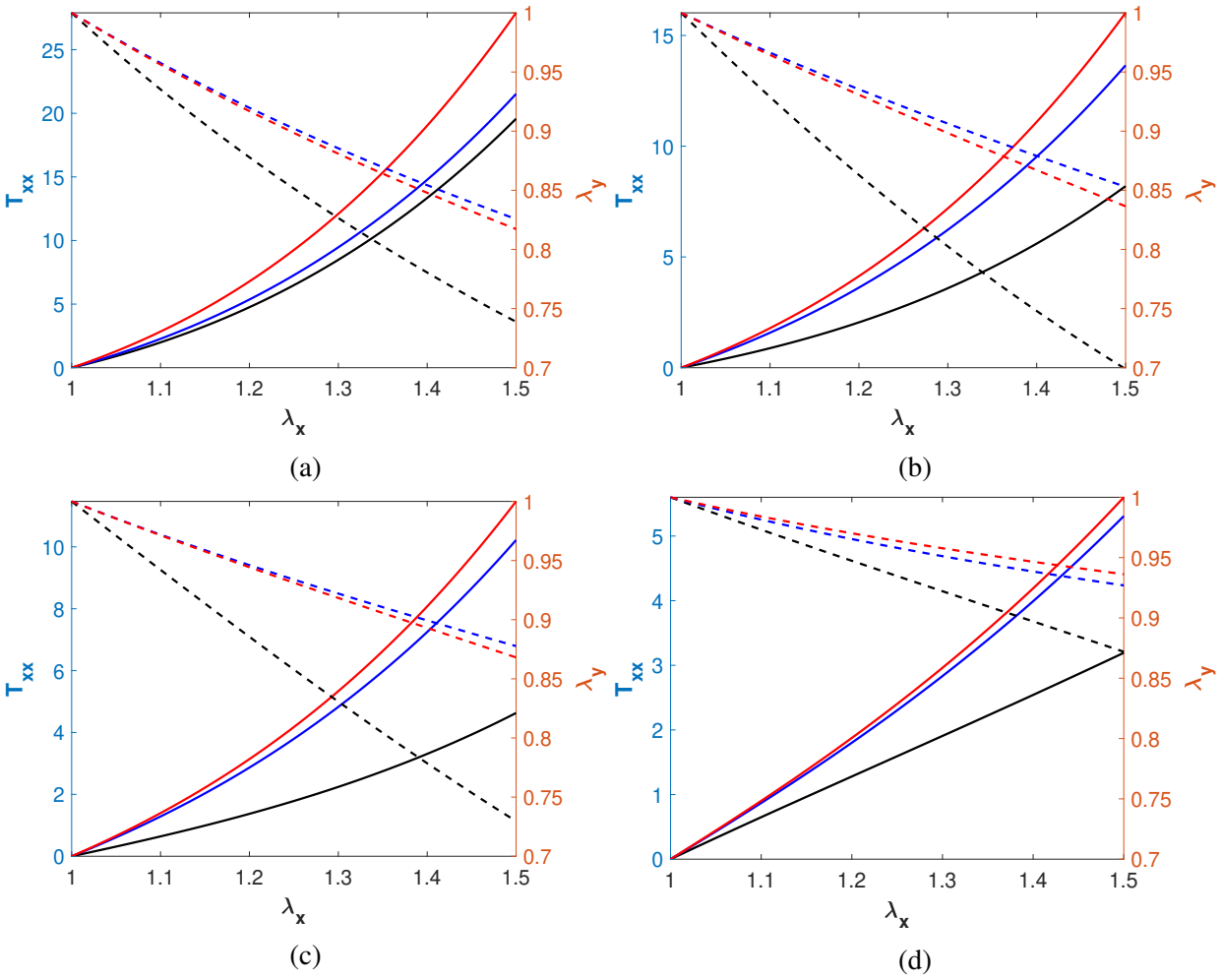

Figure 4.14: Uniaxial extension behavior of the AO and the EO constitutive relations without a hole. Cauchy stress vs stretch under uniaxial extension for (a) $\phi = 20^o$, (b) $\phi = 40^o$, (c) $\phi = 50^o$, (d) $\phi = 70^o$. T_{xx} and λ_y are shown using continuous and dashed lines, respectively . Black lines show the response of the abridged constitutive relation with $c_2 = 1$. Red and blue lines show the response of the extended orthotropic constitutive relation with $(c_2, c_3, c_4, c_5, c_6) = (0.2, 0.2, 0.2, 0.2, 0.8)$ and $(c_2, c_3, c_4, c_5, c_6) = (0.1, 0.1, 0.1, 0.1, 0.7)$, respectively.

Under pure shear deformation, the SCF variation with nominal stretch is similar to that of the uniaxial extension problem (SCF increasing with stretch for 20^o fiber angle and decreasing with stretch for 70^o fiber angle for the abridged orthotropic constitutive relation), and a stress distribution around the hole that is similar to equibiaxial extension (peak SCF not occurring at point A for the abridged orthotropic constitutive relation). This is expected as the boundary conditions in the pure shear problem partially resemble both the equibiaxial and uniaxial extension problems.

Results for the pure shear problem are presented in Figure 4.15 for the fiber angles 20^o and 70^o.

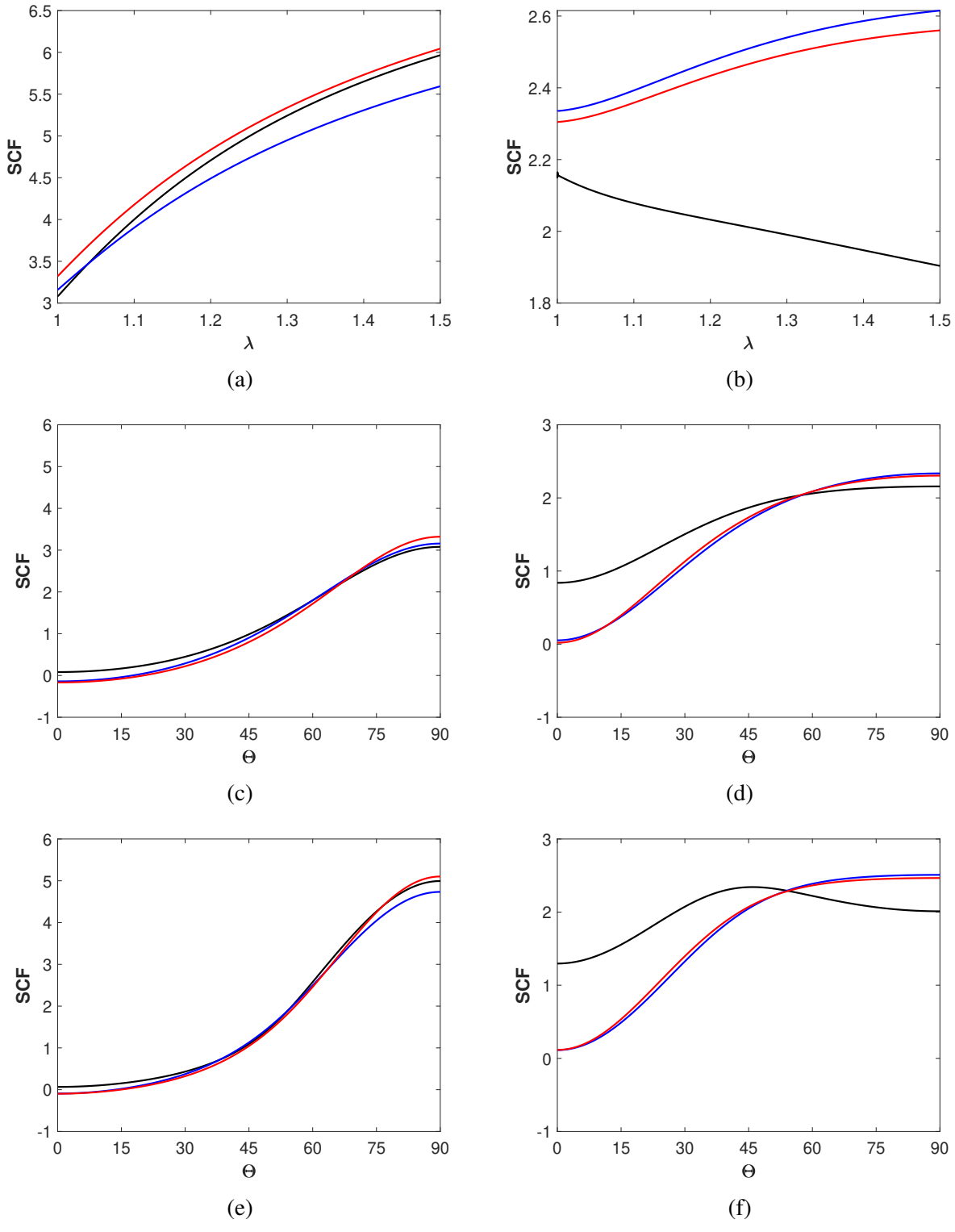

Figure 4.15: Figures (a), (b) show the variation of the stress concentration factor at point A with stretch under pure shear deformation for $\phi = 20^o$ and $\phi = 70^o$, respectively. Figures (c), (d) show the variation of SCF along the hole at $\lambda = 1+10^{-6}$ for $\phi = 20^o$ and $\phi = 70^o$, respectively. Figures (e), (f) show the same at $\lambda = 1.25$. Black lines show the response of the abridged constitutive relation with $c_2 = 1$. Red and blue lines show the response of the extended orthotropic constitutive relation with $(c_2, c_3, c_4, c_5, c_6) = (0.2, 0.2, 0.2, 0.2, 0.8)$ and $(c_2, c_3, c_4, c_5, c_6) = (0.1, 0.1, 0.1, 0.1, 0.7)$, respectively.

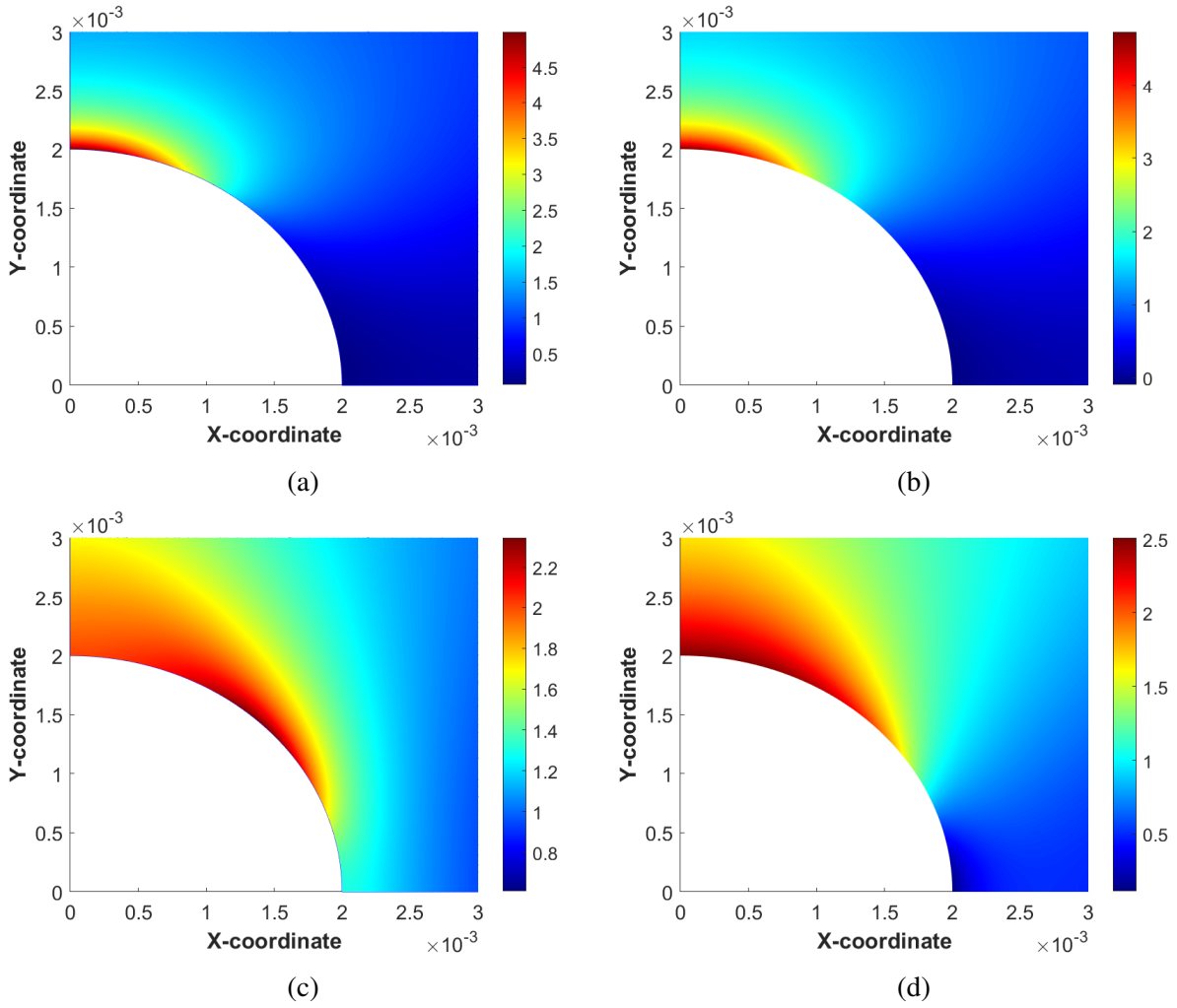

Figure 4.16: Ratio of hoop stress to nominal T_{xx} for (a) AO constitutive relation with $c_2 = 1$, $\phi = 20^o$, (b) EO constitutive relation with $(c_2, c_3, c_4, c_5, c_6) = (0.1, 0.1, 0.1, 0.1, 0.7)$, $\phi = 20^o$, (c) AO constitutive relation with $c_2 = 1$, $\phi = 70^o$, (d) EO constitutive relation with $(c_2, c_3, c_4, c_5, c_6) = (0.1, 0.1, 0.1, 0.1, 0.7)$, $\phi = 70^o$ at $\lambda = 1.25$ under pure shear deformation.

We highlighted the major differences observed in the stress concentration factor distribution between the two constitutive relations. These differences remain valid when the material parameter c_2^{AO} is varied from 0.1 (mildly anisotropic) to 10 (strongly anisotropic) and the material parameters for the EO model are varied according to the ratios discussed earlier. Surface plots of the ratio of hoop stress to nominal T_{xx} at $\lambda = 1.25$ near the hole boundary are given in figures 4.11, 4.13 and 4.16 for the fiber angles discussed above.

4.3.3 Influence of fiber angle on the stress concentration

We shall now turn our attention to the influence of fiber direction on the stress concentration factor. Fiber direction plays an important role in the mechanical and failure properties of the fiber reinforced materials. Figure 4.17 shows the dependence of the stress concentration factor at points A and C ($X = 0.002, Y = 0$) on the fiber angle with increasing nominal stretch under equibiaxial deformation. The stress concentration factor at point C under equibiaxial extension is defined to be $(\mathrm{T_{tt}}$ at C$)/(\mathrm{T_{yy}}$ at B$)$. For all the fiber angles, both the constitutive relations show an increasing stress concentration factor at point A with stretch and the SCF at a particular nominal stretch decreases with increasing fiber angle. Also, both the constitutive relations display a stress concentration factor that plateaus with increasing stretch. The abridged constitutive relation, however, shows a stress concentration factor that increases almost linearly with stretch for fiber angle of 0^o. Such an anomaly can be observed under uniaxial and pure shear deformations as well. Further differences in the behavior of constitutive relations can be seen when the stress concentration factor at point C is considered, particularly for fiber angles below 10^o as shown in Figure 4.17b, Figure 4.17d.

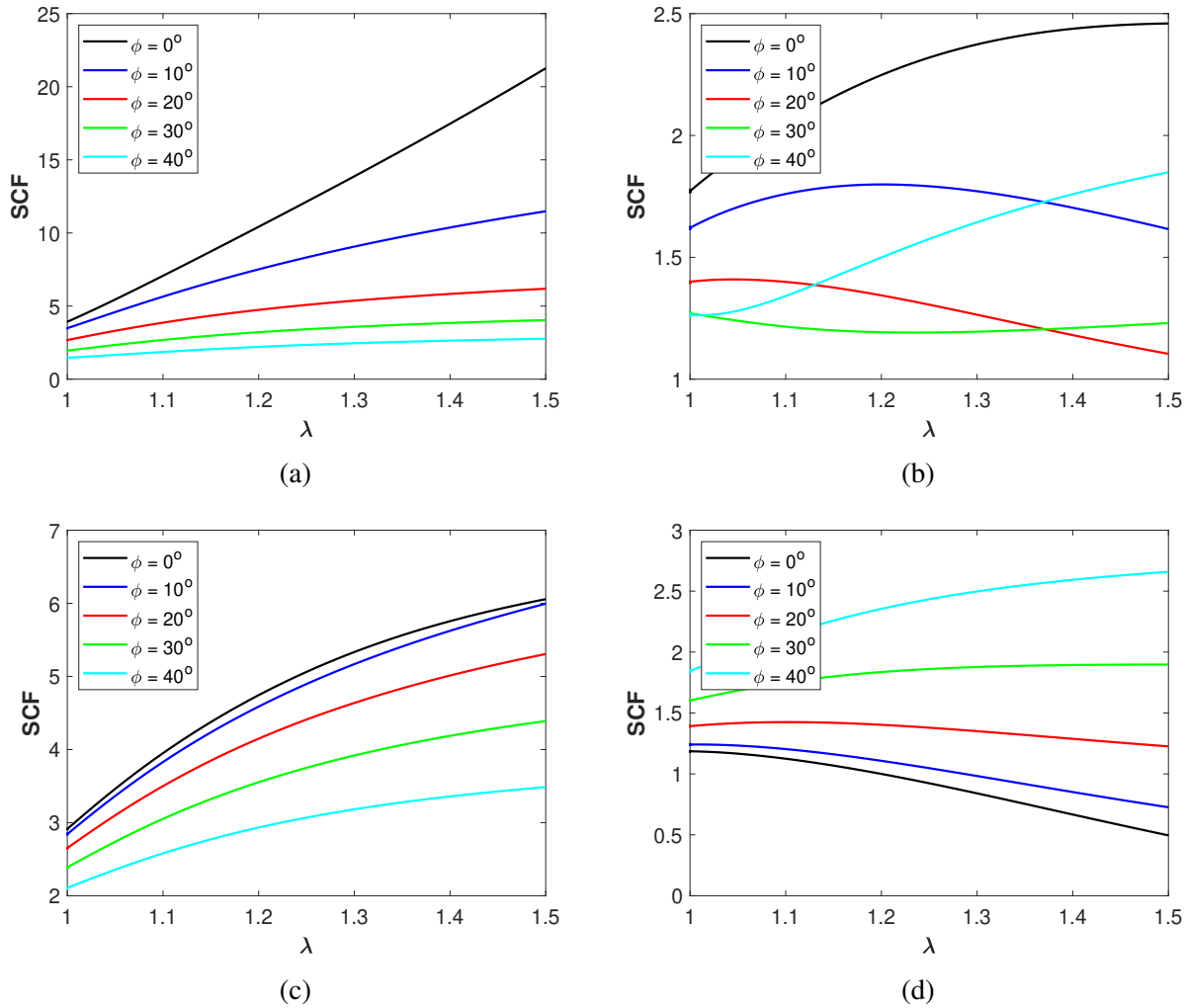

Figure 4.17: Variation of the stress concentration factor with stretch under equibiaxial extension for different fiber angles (a) at point A and (b) at point C for the abridged constitutive relation with $c_2 = 1$. (c) at point A and (d) at point C for the extended orthotropic constitutive relation with $(c_2, c_3, c_4, c_5, c_6) = (0.1, 0.1, 0.1, 0.1, 0.7)$ respectively.

A behavior similar to that of equibiaxial extension can be observed under uniaxial extension for fiber angles below 45^o, where the stress concentration factor at point A increases and plateaus with nominal stretch (except for fiber angle 0^o), as shown in Figure 4.18a and Figure 4.18c . The differences between the predictions of the two constitutive relations can be clearly seen in Figure 4.18b and Figure 4.18d for fiber angles greater than 45^o. Particularly, for the fiber angle of 90^o, while the abridged constitutive relation displays an increasing stress concentration factor

with stretch, the extended orthotropic constitutive relation shows a decreasing stress concentration factor with stretch.

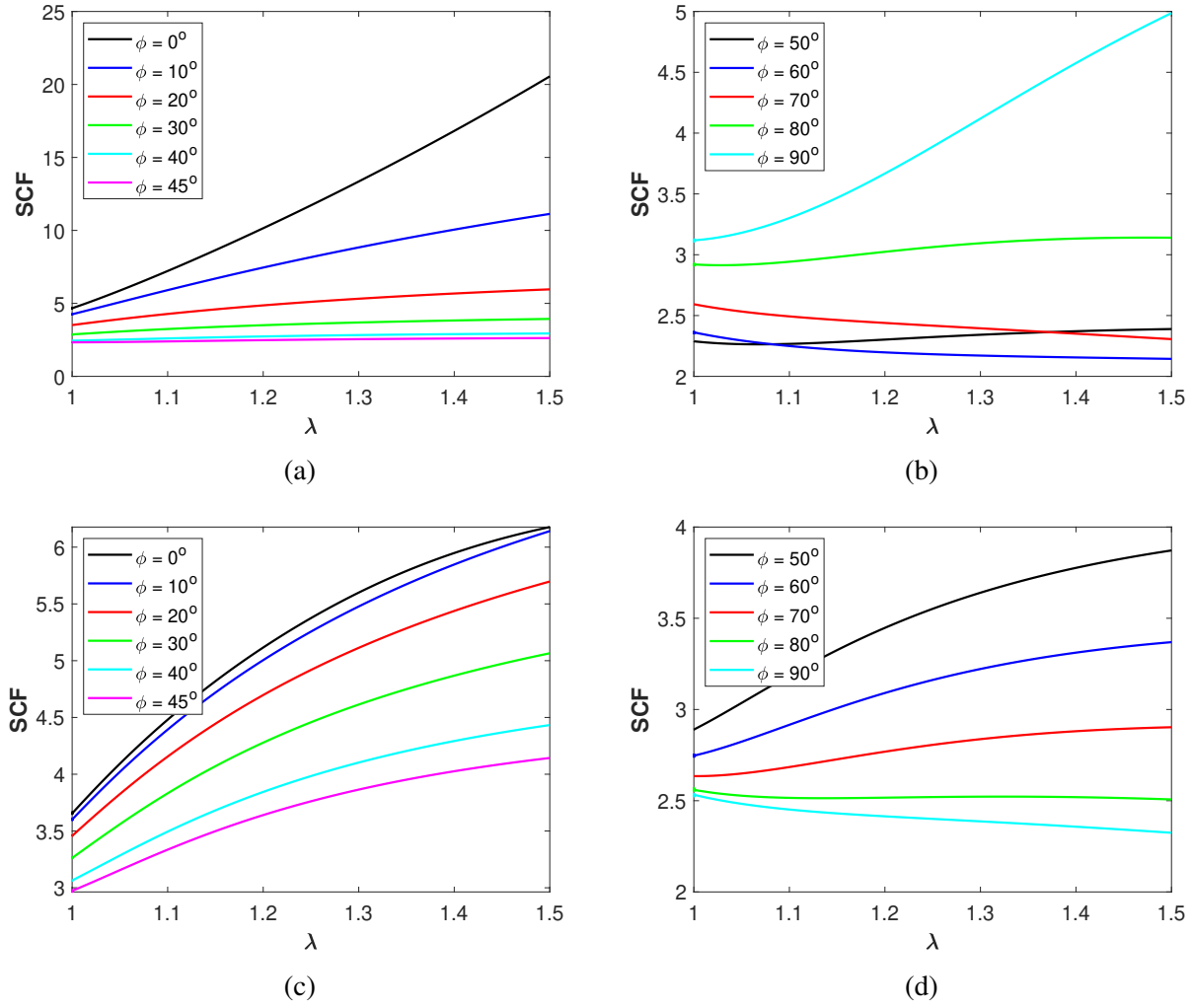

Figure 4.18: Variation of the stress concentration factor at point A with stretch under uniaxial extension for different fiber angles. Figures (a), (b) show results for the abridged constitutive relation with $c_2 = 1$. Figures (c), (d) show results for the extended orthotropic constitutive relation with $(c_2, c_3, c_4, c_5, c_6) = (0.1, 0.1, 0.1, 0.1, 0.7)$, respectively.

As discussed earlier, the variation of the stress concentration factor with stretch under pure shear is similar to uniaxial extension for all the fiber angles (refer to Figure 4.18 and Figure 4.19). Under pure shear, the stress concentration factor at point A is lower than the stress concentration

factor under uniaxial extension for both the constitutive relations.

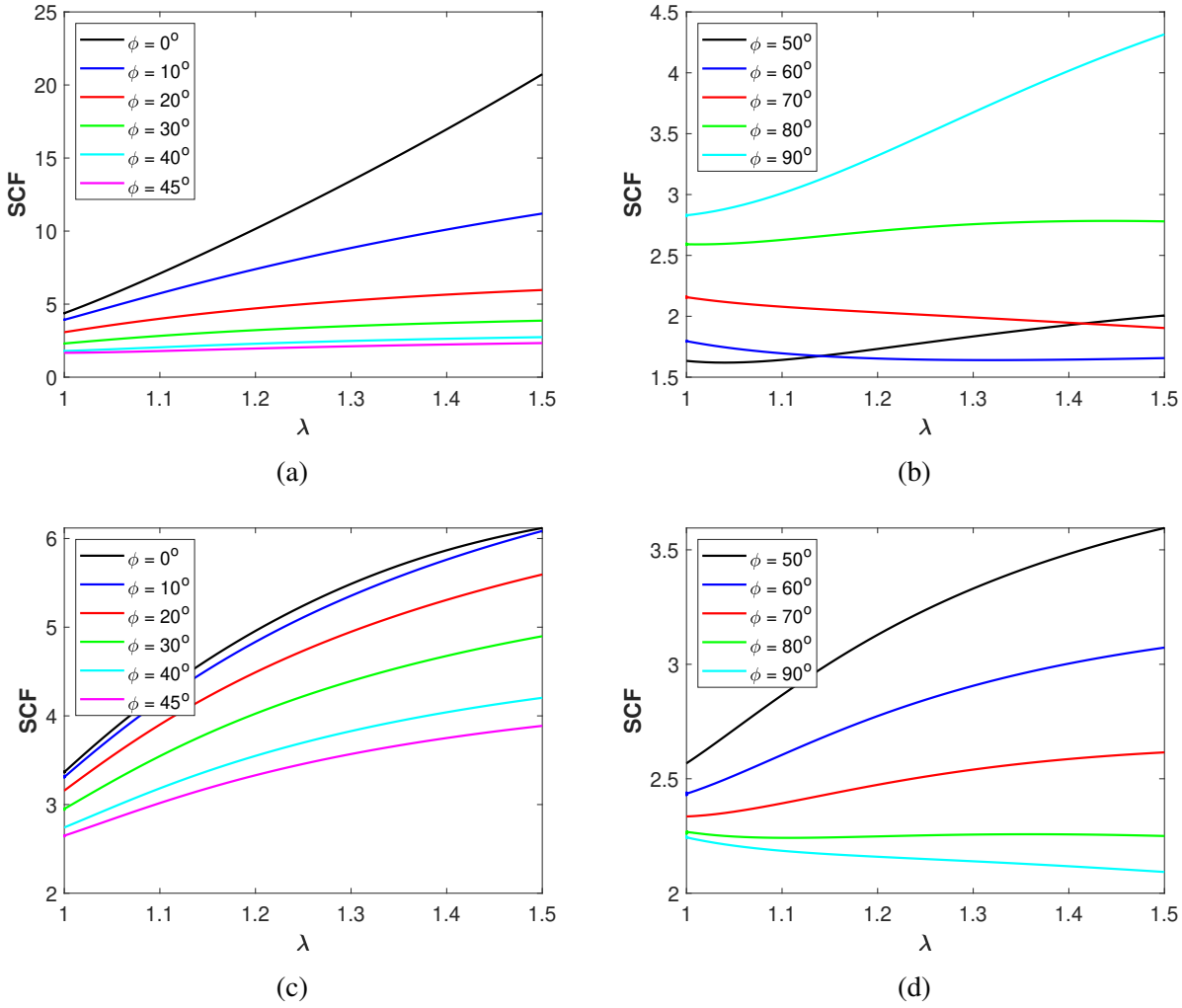

Figure 4.19: Variation of the stress concentration factor at point A with stretch under pure shear deformation for different fiber angles. Figures (a), (b) show results for the abridged constitutive relation with $c_2 = 1$. Figures (c), (d) show results for the extended orthotropic constitutive relation with $(c_2, c_3, c_4, c_5, c_6) = (0.1, 0.1, 0.1, 0.1, 0.7)$, respectively.

4.3.4 Influence of material parameters on stress concentration

In this section, we compare the influence of material parameters on the stress concentration factor at a constant applied load (constant first Piola-Kirchhoff stress). We use constant load instead of a constant nominal stretch because stresses become dramatically different with an increase in

the value of the anisotropic parameters (c_2 for the abridged constitutive relation, and c_2 to c_6 for the extended orthotropic constitutive relation). Secondly, in design, one is often interested in making a component carry a certain load. Figure 4.20 shows the variation of the stress concentration factor with the material parameter c_2 for different values of the first Piola-Kirchhoff stress at fiber angles 20^o and 70^o under uniaxial extension. The parameter c_2 is varied from 0.1-10 for the abridged constitutive relation. For the extended orthotropic constitutive relation, c_2 is varied from 0.01-1 with the remaining parameters defined as follows: $c_3, c_4, c_5 = c_2$ and $c_6 = 7c_2$. As stated earlier, these values are chosen so that the biaxial behaviour of the extended orthotropic constitutive relation with this ratio of material parameters is similar to that of the biaxial behavior of the abridged constitutive relation. An increase in the value of c_2 for the abridged constitutive relation and c_2 to c_6 for the extended orthotropic constitutive relation represents an increase in the reinforcement provided by the fibers. P_{max} is the value of the first Piola-Kirchhoff stress at a nominal stretch of 1.5 for the abridged constitutive relation with $c_2 = 0.1$ and for the extended orthotropic constitutive relation with $c_2 = 0.01$. Some similarities between the two constitutive relations can be observed here. At 20^o fiber angle, both the constitutive relations show an increasing SCF with c_2 at smaller first Piola-Kirchhoff stress. At larger values of the first Piola-Kirchhoff stress, the dependence of SCF on c_2 becomes non-monotonic as shown in Figure 4.20a and Figure 4.20b. At 70^o fiber angle, both the constitutive relations show a decreasing stress concentration factor with increasing c_2 at a constant first Piola-Kirchhoff stress.

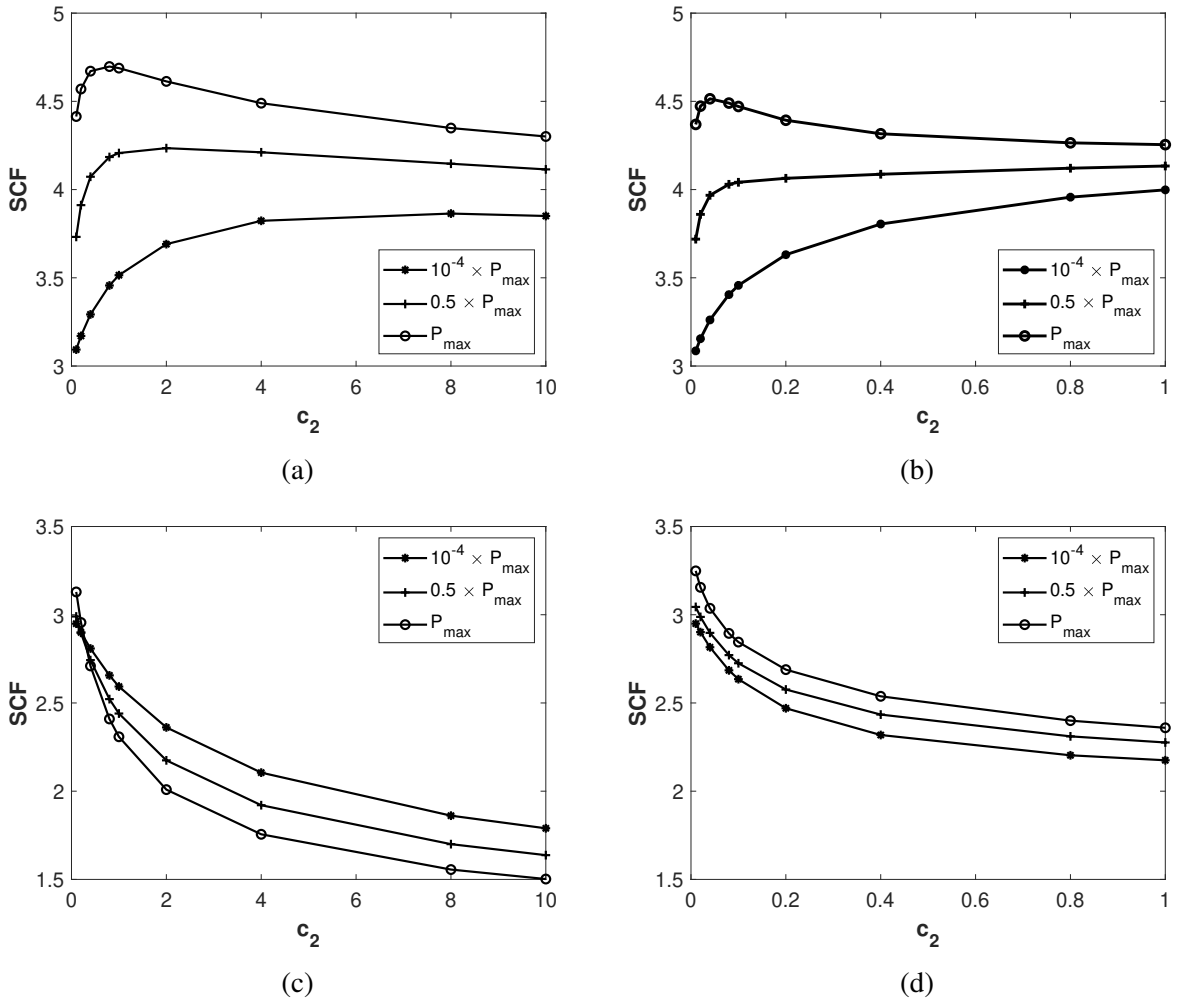

Figure 4.20: Variation of the stress concentration factor at point A with material parameters for a varying load. (a) abridged constitutive relation with fiber angle 20^o, (b) extended orthotropic constitutive relation with fiber angle 20^o, (c) abridged constitutive relation with fiber angle 70^o, (d) extended orthotropic constitutive relation with fiber angle 70^o.

4.3.4.1 A peculiar feature of the abridged orthotropic constitutive relation

The stress concentration factor at the hole for the abridged orthotropic constitutive relation shows a distinct peak for higher values of the parameter c_2 for fiber angles below 45^o under uniaxial extension. This is shown in Figure 4.21a for the material with 20^o fiber angle. Such a peak is absent in case of the extended orthotropic constitutive relation even at very large values of c_2. For the abridged constitutive relation, the maximum stress concentration factor occurs at an angle close

to $90^o - \phi$ with the X-axis for a material with fiber angle $\phi < 45^o$. This maximum occurs not only at large nominal stretches but also at small strains when the parameter c_2 is very high (see Figure 4.21b). Figure 4.21c and Figure 4.21d shows the local SCF variation for the abridged and the extended orthotropic constitutive relations. It can be seen that the spike in the stress concentration factor for the abridged constitutive relation is localized to a narrow region close to the edge of the hole (enclosed in the circle in Figure 4.21c). The spike in SCF is so high for large values of c_2, that one invariably expects the failure to occur close to $90^o - \phi$ under uniaxial extension, provided the material can be described by the abridged constitutive relation. This could possibly serve as an indication as to whether the choice of the abridged orthotropic constitutive relation is suitable for the description of a material having orthotropic symmetry when studying the initiation of failure.

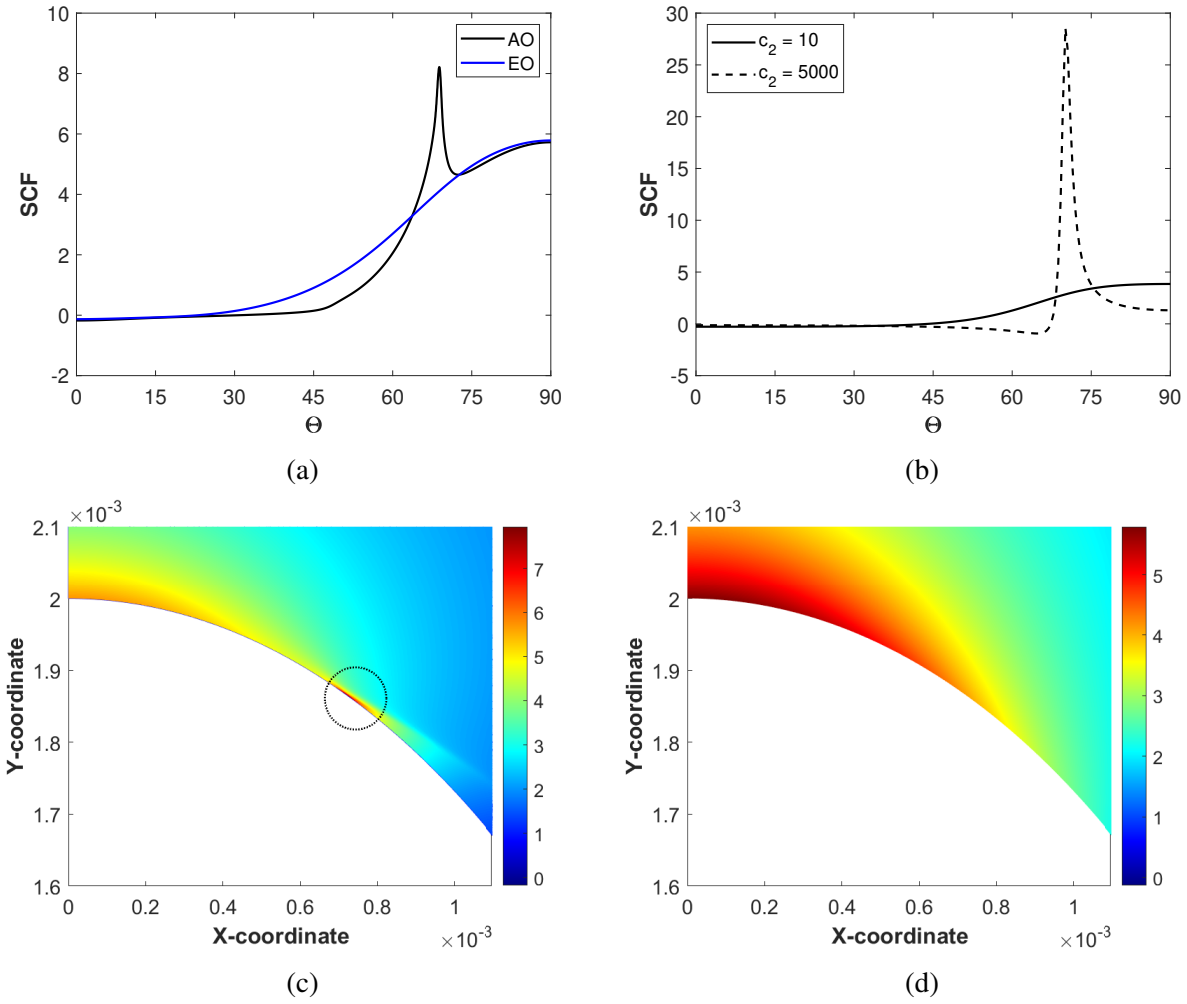

Figure 4.21: (a) SCF along the hole for the AO constitutive relation with $c_2 = 10$ and the EO constitutive relation with $(c_2, c_3, c_4, c_5, c_6) = (1, 1, 1, 1, 7)$ at $\lambda = 1.3$, (b) Theoretical SCF along the hole at small strain for the linearized version of the AO constitutive relation with $c_2 = 10$ and $c_2 = 5000$, (c) Ratio of hoop stress to nominal T_{xx} for the AO constitutive relation with $c_2 = 10$, (d) Ratio of hoop stress to nominal T_{xx} for the EO constitutive relation with $(c_2, c_3, c_4, c_5, c_6) = (1, 1, 1, 1, 7)$. These results are for the uniaxial extension problem for a material with $\phi = 20^o$.

4.4 Conclusions

We have studied the stress concentration factor around a circular hole in a square sheet reinforced by two families of fibers using two constitutive relations, one that upon linearization agrees with orthotropic linearized elasticity and another that is commonly used but does not reduce to the orthotropic linearized elastic constitutive relation. Biaxial tests with loads applied along the planes

of symmetry are often used to estimate the material parameters of the constitutive relations intended to describe the mechanical response of orthotropic materials. The material parameters considered in our study render the two constitutive relations displaying a similar stress-deformation behavior under biaxial extension in the absence of a hole. However, the two constitutive relations show significant differences in the stress concentration factor distribution under equibiaxial, uniaxial and pure shear deformations in the presence of a circular hole. One can expect such differences to be amplified in the presence of elliptic holes and cracks. Further, the abridged orthotropic constitutive relation based on a partial set of fiber invariants displays a spike in the stress concentration factor at an angle $90 - \phi$ under uniaxial extension (where ϕ is the fiber angle). In contrast, such a spike in SCF is absent in the extended orthotropic constitutive relation that agrees with linear elastic orthotropic constitutive relation. Unlike the case of isotropic materials, the location of the maximum stress concentration factor along the hole boundary depends on the nominal stretch, the fiber angle and the choice of the constitutive relation. Interestingly, certain fiber angles even show a decreasing stress concentration factor with nominal stretch.

Due to the number of invariants involved in describing the orthotropic material, choosing a form of the stored energy function becomes exceedingly complicated. Even with reasonably simple constitutive equations like the ones discussed here, multiple sets of constitutive parameters may produce the same nominal biaxial or uniaxial response. It must be recognized that, while demonstrating a comparable biaxial stress-deformation response in the absence of discontinuities or inhomogeneities, significant differences may exist in the local stress distributions predicted by the constitutive models that do and do not agree with anisotropic linear elasticity in the presence of discontinuities or inhomogeneities. Therefore, a prudent choice of the constitutive relation is important when one is interested in studying stress distribution near discontinuities like a hole or a crack.

5. SUMMARY

A patient harboring a thoracic aortic aneurysm or sustained an aortic dissection is typically old with one or more concomitant risk factors like hypertension, atherosclerosis, bicuspid aortic valve, smoking, history of familial aortic aneurysm/dissection, etc ([19], [20]). In younger patients, dilatation of the aorta or aortic dissection is invariably associated with connective tissue disorders like Marfan syndrome, Loeys-Dietz syndrome, Turner's syndrome, etc ([141], [20]). Accurate prognosis of the thoracic aortic disease requires

- Identifying the alterations in the mechanical properties of the thoracic aorta due to various pathologies and comorbidities as opposed to non-pathological aging.
- Development of computational models that can account for such changes has been proposed as a methodology to assess the risk of an impending catastrophic event like aneurysm rupture or dissection.

Ex-vivo experimental characterization of the mechanical response of the aortic tissue in good health and disease, and the theoretical development of appropriate constitutive equations are precursors to applying this methodology. This dissertation addresses some of these and the conclusions for the current work are listed below.

5.1 Conclusions from peeling experiments on porcine thoracic aorta

Higher peel force per unit width and peeling energy per unit area were required to advance a tear in the ascending aorta compared to the descending aorta. Mean peel force per unit width in the circumferential direction was lower than in the longitudinal direction for all the thoracic aortic segments. The mean stretch experienced by the peeled halves during the peel test falls in the linear to non-linear transition region of the uniaxial stress-strain curve for the entire thoracic aorta. Thus, the influence of the nonlinear mechanical behavior of the aorta was found to be minimal in the estimation of the peeling energy per unit area. This confirms the validity of assuming a linear

relationship between the first Piola-Kirchhoff stress and stretch in the peeled halves during peeling experiments on the thoracic aorta.

5.2 Conclusions from uniaxial experiments on the porcine thoracic aorta

To determine the constitutive response of the aorta, uniaxial experiments on the porcine thoracic aorta showed the need for conducting off-axis tests and measuring full 2d deformation during the test. The E_{XY} versus nominal stretch showed a strong dependence on the orientation highlighting the anisotropic response of the porcine thoracic aorta. The nominal stress at failure decreased from the circumferential direction of the aorta to the longitudinal direction. Constitutive parameters reported in literature based on biaxial test data along the planes of symmetry are unable to qualitatively represent the deformation undergone by off-axis specimens during a uniaxial test.

5.3 Conclusions from the study of stress distribution at a circular hole in two-fiber reinforced materials

Our analysis indicates a strong dependence of the local stress distribution around a circular hole on the constitutive equation chosen to model the two-fiber reinforced material. It was shown how two constitutive relations having a similar biaxial response along the directions of symmetry exhibit substantially different distribution of the stress concentration factor. The variation of the stress concentration factor with the nominal stretch is also strongly dependent on the constitutive equation. The abridged constitutive relation, which is dependent on a subset of the full invariant set necessary for modeling two fiber reinforced materials, displays a spike in the stress concentration factor at an angle $90 - \phi$ under uniaxial extension (where ϕ is the fiber angle). The spike in SCF is so high for the abridged relation that one invariably expects failure to occur at $90 - \phi$. Such a spike in the stress concentration factor is absent when using an extended model that appropriately reduces to the linearized elastic orthotropic case. Further, it indicates how the location of failure predicted by two constitutive relations can be extremely different. Additionally, abridged model shows an out-of-plane uniaxial response (i.e. in the direction orthogonal to the plane of the fibers) that is not typically observed in experiments on fiber reinforced materials. We suggest that a

careful choice of the constitutive relation becomes crucial when one is interested in studying stress distribution near discontinuities and inhomogeneities.

5.4 Recommendations for future work

Studying the biaxial response of the thoracic aorta by obtaining specimens at different orientations is an immediate requirement for the development of appropriate constitutive equations to model its behavior. Constitutive equations based on classical invariants have high covariance between the response functions, thus rendering them unfriendly for an experimentalist in interpreting the data[142]. There are new approaches that may address certain problems of using classical invariants to describe the constitutive behavior of anisotropic materials (see [143], [144], [145], [146], [147], [148]). Investigating these approaches to modeling biological tissues where lack of enough experimental data is pervasive is worth considering.

REFERENCES

[1] J. A. Rhodin, "Architecture of the vessel wall," *Comprehensive physiology*, pp. 1–31, 2011.

[2] R. S. Elsayed, R. G. Cohen, F. Fleischman, and M. E. Bowdish, "Acute type a aortic dissection," *Cardiology clinics*, vol. 35, no. 3, pp. 331–345, 2017.

[3] F. Schroeder, S. Polzer, M. Slažanskỳ, V. Man, and P. Skácel, "Predictive capabilities of various constitutive models for arterial tissue," *Journal of the mechanical behavior of biomedical materials*, vol. 78, pp. 369–380, 2018.

[4] J. A. Peña, M. A. Martínez, and E. Peña, "Layer-specific residual deformations and uniaxial and biaxial mechanical properties of thoracic porcine aorta," *Journal of the Mechanical Behavior of Biomedical Materials*, vol. 50, pp. 55–69, 2015.

[5] L. F. Hiratzka, G. L. Bakris, J. A. Beckman, R. M. Bersin, V. F. Carr, D. E. Casey, K. A. Eagle, L. K. Hermann, E. M. Isselbacher, E. A. Kazerooni, *et al.*, "2010 accf/aha/aats/acr/asa/sca/scai/sir/sts/svm guidelines for the diagnosis and management of patients with thoracic aortic disease," *Journal of the American College of Cardiology*, vol. 55, no. 14, pp. e27–e129, 2010.

[6] R. Erbel, V. Aboyans, C. Boileau, E. Bossone, R. D. Bartolomeo, H. Eggebrecht, A. Evangelista, V. Falk, H. Frank, *et al.*, "2014 esc guidelines on the diagnosis and treatment of aortic diseases: Document covering acute and chronic aortic diseases of the thoracic and abdominal aorta of the adult the task force for the diagnosis and treatment of aortic diseases of the european society of cardiology (esc)," *European heart journal*, vol. 35, no. 41, pp. 2873–2926, 2014.

[7] K. H. Chau and J. A. Elefteriades, "Natural history of thoracic aortic aneurysms: size matters, plus moving beyond size," *Progress in cardiovascular diseases*, vol. 56, no. 1, pp. 74–80, 2013.

[8] M. A. Coady, J. A. Rizzo, G. L. Hammond, G. S. Kopf, and J. A. Elefteriades, "Surgical intervention criteria for thoracic aortic aneurysms: a study of growth rates and complications," *The Annals of thoracic surgery*, vol. 67, no. 6, pp. 1922–1926, 1999.

[9] D. A. Vorp, "Biomechanics of abdominal aortic aneurysm," *Journal of biomechanics*, vol. 40, no. 9, pp. 1887–1902, 2007.

[10] D. A. Vorp, B. J. Schiro, M. P. Ehrlich, T. S. Juvonen, M. A. Ergin, and B. P. Griffith, "Effect of aneurysm on the tensile strength and biomechanical behavior of the ascending thoracic aorta," *The Annals of thoracic surgery*, vol. 75, no. 4, pp. 1210–1214, 2003.

[11] D. C. Iliopoulos, R. P. Deveja, E. P. Kritharis, D. Perrea, G. D. Sionis, K. Toutouzas, C. Stefanadis, and D. P. Sokolis, "Regional and directional variations in the mechanical properties of ascending thoracic aortic aneurysms," *Medical engineering & physics*, vol. 31, no. 1, pp. 1–9, 2009.

[12] D. P. Sokolis, E. P. Kritharis, and D. C. Iliopoulos, "Effect of layer heterogeneity on the biomechanical properties of ascending thoracic aortic aneurysms," *Medical & biological engineering & computing*, vol. 50, no. 12, pp. 1227–1237, 2012.

[13] A. Tsamis, J. T. Krawiec, and D. A. Vorp, "Elastin and collagen fibre microstructure of the human aorta in ageing and disease: a review," *Journal of the Royal Society Interface*, vol. 10, no. 83, p. 20121004, 2013.

[14] A. Duprey, O. Trabelsi, M. Vola, J.-P. Favre, and S. Avril, "Biaxial rupture properties of ascending thoracic aortic aneurysms," *Acta biomaterialia*, vol. 42, pp. 273–285, 2016.

[15] O. Trabelsi, F. M. Davis, J. F. Rodriguez-Matas, A. Duprey, and S. Avril, "Patient specific stress and rupture analysis of ascending thoracic aneurysms," *Journal of biomechanics*, vol. 48, no. 10, pp. 1836–1843, 2015.

[16] D. Farotto, P. Segers, B. Meuris, J. Vander Sloten, and N. Famaey, "The role of biomechanics in aortic aneurysm management: requirements, open problems and future prospects," *Journal of the mechanical behavior of biomedical materials*, vol. 77, pp. 295–307, 2018.

[17] G. Martufi, A. Forneris, J. J. Appoo, and E. S. Di Martino, "Is there a role for biomechanical engineering in helping to elucidate the risk profile of the thoracic aorta?," *The Annals of thoracic surgery*, vol. 101, no. 1, pp. 390–398, 2016.

[18] K. Rajagopal, C. Bridges, and K. Rajagopal, "Towards an understanding of the mechanics underlying aortic dissection," *Biomechanics and modeling in mechanobiology*, vol. 6, no. 5, pp. 345–359, 2007.

[19] J. Elefteriades, *Acute aortic disease*. CRC Press, 2007.

[20] L. A. Pape, M. Awais, E. M. Woznicki, T. Suzuki, S. Trimarchi, A. Evangelista, T. Myrmel, M. Larsen, K. M. Harris, K. Greason, *et al.*, "Presentation, diagnosis, and outcomes of acute aortic dissection: 17-year trends from the international registry of acute aortic dissection," *Journal of the American College of Cardiology*, vol. 66, no. 4, pp. 350–358, 2015.

[21] J. Golledge and K. A. Eagle, "Acute aortic dissection," *The Lancet*, vol. 372, no. 9632, pp. 55–66, 2008.

[22] J. Humphrey and M. Epstein, "Cardiovascular solid mechanics: cells, tissues, and organs," 2002.

[23] S. Sherifova and G. A. Holzapfel, "Biomechanics of aortic wall failure with a focus on dissection and aneurysm: A review," *Acta biomaterialia*, 2019.

[24] D. Mohan and J. W. Melvin, "Failure properties of passive human aortic tissue. iuniaxial tension tests," *Journal of biomechanics*, vol. 15, no. 11, pp. 887–902, 1982.

[25] D. Mohan and J. W. Melvin, "Failure properties of passive human aortic tissue. iibiaxial tension tests," *Journal of biomechanics*, vol. 16, no. 1, pp. 31–44, 1983.

[26] D. C. Iliopoulos, E. P. Kritharis, A. T. Giagini, S. A. Papadodima, and D. P. Sokolis, "Ascending thoracic aortic aneurysms are associated with compositional remodeling and vessel stiffening but not weakening in age-matched subjects," *The Journal of thoracic and cardiovascular surgery*, vol. 137, no. 1, pp. 101–109, 2009.

[27] D. P. Sokolis, E. P. Kritharis, A. T. Giagini, K. M. Lampropoulos, S. A. Papadodima, and D. C. Iliopoulos, "Biomechanical response of ascending thoracic aortic aneurysms: association with structural remodelling," *Computer methods in biomechanics and biomedical engineering*, vol. 15, no. 3, pp. 231–248, 2012.

[28] C. M. García-Herrera, J. M. Atienza, F. Rojo, E. Claes, G. Guinea, D. J. Celentano, C. García-Montero, and R. L. Burgos, "Mechanical behaviour and rupture of normal and pathological human ascending aortic wall," *Medical & biological engineering & computing*, vol. 50, no. 6, pp. 559–566, 2012.

[29] K. Khanafer, A. Duprey, M. Zainal, M. Schlicht, D. Williams, and R. Berguer, "Determination of the elastic modulus of ascending thoracic aortic aneurysm at different ranges of pressure using uniaxial tensile testing," *The Journal of thoracic and cardiovascular surgery*, vol. 142, no. 3, pp. 682–686, 2011.

[30] J. E. Pichamuthu, J. A. Phillippi, D. A. Cleary, D. W. Chew, J. Hempel, D. A. Vorp, and T. G. Gleason, "Differential tensile strength and collagen composition in ascending aortic aneurysms by aortic valve phenotype," *The Annals of thoracic surgery*, vol. 96, no. 6, pp. 2147–2154, 2013.

[31] A. Ferrara, S. Morganti, P. Totaro, A. Mazzola, and F. Auricchio, "Human dilated ascending aorta: mechanical characterization via uniaxial tensile tests," *Journal of the mechanical behavior of biomedical materials*, vol. 53, pp. 257–271, 2016.

[32] R. J. Okamoto, J. E. Wagenseil, W. R. DeLong, S. J. Peterson, N. T. Kouchoukos, and T. M. Sundt, "Mechanical properties of dilated human ascending aorta," *Annals of biomedical engineering*, vol. 30, no. 5, pp. 624–635, 2002.

[33] T. Pham, C. Martin, J. Elefteriades, and W. Sun, "Biomechanical characterization of ascending aortic aneurysm with concomitant bicuspid aortic valve and bovine aortic arch," *Acta biomaterialia*, vol. 9, no. 8, pp. 7927–7936, 2013.

[34] N. Choudhury, O. Bouchot, L. Rouleau, D. Tremblay, R. Cartier, J. Butany, R. Mongrain, and R. L. Leask, "Local mechanical and structural properties of healthy and diseased human ascending aorta tissue," *Cardiovascular Pathology*, vol. 18, no. 2, pp. 83–91, 2009.

[35] M. Di Giuseppe, G. Alotta, V. Agnese, D. Bellavia, G. M. Raffa, V. Vetri, M. Zingales, S. Pasta, and M. Pilato, "Identification of circumferential regional heterogeneity of ascending thoracic aneurysmal aorta by biaxial mechanical testing," *Journal of molecular and cellular cardiology*, vol. 130, pp. 205–215, 2019.

[36] C. Manopoulos, I. Karathanasis, I. Kouerinis, D. C. Angouras, A. Lazaris, S. Tsangaris, and D. P. Sokolis, "Identification of regional/layer differences in failure properties and thickness as important biomechanical factors responsible for the initiation of aortic dissections," *Journal of Biomechanics*, vol. 80, pp. 102–110, 2018.

[37] A. R. Babu, A. G. Byju, and N. Gundiah, "Biomechanical properties of human ascending thoracic aortic dissections," *Journal of biomechanical engineering*, vol. 137, no. 8, 2015.

[38] N. F. MacLean, N. L. Dudek, and M. R. Roach, "The role of radial elastic properties in the development of aortic dissections," *Journal of vascular surgery*, vol. 29, no. 4, pp. 703–710, 1999.

[39] G. Sommer, T. C. Gasser, P. Regitnig, M. Auer, and G. A. Holzapfel, "Dissection properties of the human aortic media: an experimental study," *Journal of biomechanical engineering*, vol. 130, no. 2, p. 021007, 2008.

[40] J. Tong, G. Sommer, P. Regitnig, and G. A. Holzapfel, "Dissection properties and mechanical strength of tissue components in human carotid bifurcations," *Annals of biomedical engineering*, vol. 39, no. 6, pp. 1703–1719, 2011.

[41] J.-H. Kim, S. Avril, A. Duprey, and J.-P. Favre, "Experimental characterization of rupture in human aortic aneurysms using a full-field measurement technique," *Biomechanics and modeling in mechanobiology*, vol. 11, no. 6, pp. 841–853, 2012.

[42] A. Romo, P. Badel, A. Duprey, J.-P. Favre, and S. Avril, "In vitro analysis of localized aneurysm rupture," *Journal of Biomechanics*, vol. 47, no. 3, pp. 607–616, 2014.

[43] F. M. Davis, Y. Luo, S. Avril, A. Duprey, and J. Lu, "Pointwise characterization of the elastic properties of planar soft tissues: application to ascending thoracic aneurysms," *Biomechanics and modeling in mechanobiology*, vol. 14, no. 5, pp. 967–978, 2015.

[44] F. M. Davis, Y. Luo, S. Avril, A. Duprey, and J. Lu, "Local mechanical properties of human ascending thoracic aneurysms," *Journal of the mechanical behavior of biomedical materials*, vol. 61, pp. 235–249, 2016.

[45] J. Robertson and K. Viner Smith, "An analysis of certain factors associated with the production of experimental dissection of the aortic media, in relation to the pathogenesis of dissecting aneurysm," *The Journal of pathology and bacteriology*, vol. 60, no. 1, pp. 43–49, 1948.

[46] A. E. Hirst Jr and V. J. Johns Jr, "Experimental dissection of media of aorta by pressure: its relation to spontaneous dissecting aneurysm," *Circulation research*, vol. 10, no. 6, pp. 897–903, 1962.

[47] M. W. Carson and M. R. Roach, "The strength of the aortic media and its role in the propagation of aortic dissection," *Journal of biomechanics*, vol. 23, no. 6, pp. 579–588, 1990.

[48] I. Tiessen and M. Roach, "Factors in the initiation and propagation of aortic dissections in human autopsy aortas," *Journal of biomechanical engineering*, vol. 115, pp. 123–125, 1993.

[49] C. M. He and M. R. Roach, "Changes in tearing pressure with the geometry of dissections in porcine aortas," in *Proceedings of the 1995 Fourteenth Southern Biomedical Engineering Conference*, pp. 38–41, IEEE, 1995.

[50] A. S. Tam, M. C. Sapp, and M. R. Roach, "The effect of tear depth on the propagation of aortic dissections in isolated porcine thoracic aorta," *Journal of biomechanics*, vol. 31, no. 7, pp. 673–676, 1998.

[51] J. Tong, T. Cohnert, P. Regitnig, J. Kohlbacher, R. Birner-Grünberger, A. J. Schriefl, G. Sommer, and G. A. Holzapfel, "Variations of dissection properties and mass fractions with thrombus age in human abdominal aortic aneurysms," *Journal of biomechanics*, vol. 47, no. 1, pp. 14–23, 2014.

[52] S. Pasta, J. A. Phillippi, T. G. Gleason, and D. A. Vorp, "Effect of aneurysm on the mechanical dissection properties of the human ascending thoracic aorta," *The Journal of Thoracic and Cardiovascular Surgery*, vol. 143, no. 2, pp. 460–467, 2012.

[53] D. C. Angouras, E. P. Kritharis, and D. P. Sokolis, "Regional distribution of delamination strength in ascending thoracic aortic aneurysms," *Journal of the mechanical behavior of biomedical materials*, vol. 98, pp. 58–70, 2019.

[54] C. Noble, N. Smulders, R. Lewis, M. J. Carré, S. E. Franklin, S. MacNeil, and Z. A. Taylor, "Controlled peel testing of a model tissue for diseased aorta," *Journal of biomechanics*, vol. 49, no. 15, pp. 3667–3675, 2016.

[55] Y. Wang, J. A. Johnson, F. G. Spinale, M. A. Sutton, and S. M. Lessner, "Quantitative measurement of dissection resistance in intimal and medial layers of human coronary arteries," *Experimental mechanics*, vol. 54, no. 4, pp. 677–683, 2014.

[56] Y. Luo, Z. Fan, S. Baek, and J. Lu, "Machine learning–aided exploration of relationship between strength and elastic properties in ascending thoracic aneurysm," *International journal for numerical methods in biomedical engineering*, vol. 34, no. 6, p. e2977, 2018.

[57] X. He, S. Avril, and J. Lu, "Prediction of local strength of ascending thoracic aortic aneurysms," *Journal of the Mechanical Behavior of Biomedical Materials*, vol. 115, p. 104284, 2021.

[58] X. He, S. Avril, and J. Lu, "Estimating aortic thoracic aneurysm rupture risk using tension–strain data in physiological pressure range: an in vitro study," *Biomechanics and Modeling in Mechanobiology*, vol. 20, no. 2, pp. 683–699, 2021.

[59] M. Liu, H. Dong, X. Lou, G. Iannucci, E. P. Chen, B. G. Leshnower, and W. Sun, "A novel anisotropic failure criterion with dispersed fiber orientations for aortic tissues," *Journal of Biomechanical Engineering*, vol. 142, no. 11, 2020.

[60] D. P. Sokolis, "Passive mechanical properties and structure of the aorta: segmental analysis," *Acta physiologica*, vol. 190, no. 4, pp. 277–289, 2007.

[61] T. C. Gasser and G. A. Holzapfel, "Modeling the propagation of arterial dissection," *European Journal of Mechanics-A/Solids*, vol. 25, no. 4, pp. 617–633, 2006.

[62] T. C. Gasser, R. W. Ogden, and G. A. Holzapfel, "Hyperelastic modelling of arterial layers with distributed collagen fibre orientations," *Journal of the royal society interface*, vol. 3, no. 6, pp. 15–35, 2006.

[63] A. Ferrara and A. Pandolfi, "A numerical study of arterial media dissection processes," *International journal of fracture*, vol. 166, no. 1, pp. 21–33, 2010.

[64] L. Wang, S. M. Roper, X. Luo, and N. A. Hill, "Modelling of tear propagation and arrest in fibre-reinforced soft tissue subject to internal pressure," *Journal of Engineering Mathematics*, vol. 95, no. 1, pp. 249–265, 2015.

[65] L. Wang, S. M. Roper, N. A. Hill, and X. Luo, "Propagation of dissection in a residually-stressed artery model," *Biomechanics and modeling in mechanobiology*, vol. 16, no. 1, pp. 139–149, 2017.

[66] M. Rausch, G. Karniadakis, and J. Humphrey, "Modeling soft tissue damage and failure using a combined particle/continuum approach," *Biomechanics and modeling in mechanobiology*, vol. 16, no. 1, pp. 249–261, 2017.

[67] S. Baek, R. L. Gleason, K. Rajagopal, and J. Humphrey, "Theory of small on large: potential utility in computations of fluid–solid interactions in arteries," *Computer methods in applied mechanics and engineering*, vol. 196, no. 31-32, pp. 3070–3078, 2007.

[68] O. Gültekin, H. Dal, and G. A. Holzapfel, "A phase-field approach to model fracture of arterial walls: theory and finite element analysis," *Computer methods in applied mechanics and engineering*, vol. 312, pp. 542–566, 2016.

[69] O. Gültekin and G. A. Holzapfel, "A brief review on computational modeling of rupture in soft biological tissues," *Advances in Computational Plasticity*, pp. 113–144, 2018.

[70] C. E. Korenczuk, R. Y. Dhume, K. K. Liao, and V. H. Barocas, "Ex vivo mechanical tests and multiscale computational modeling highlight the importance of intramural shear stress in ascending thoracic aortic aneurysms," *Journal of biomechanical engineering*, vol. 141, no. 12, 2019.

[71] G. Chagnon, M. Rebouah, and D. Favier, "Hyperelastic energy densities for soft biological tissues: a review," *Journal of Elasticity*, vol. 120, no. 2, pp. 129–160, 2015.

[72] G. A. Holzapfel, T. C. Gasser, and R. W. Ogden, "A new constitutive framework for arterial wall mechanics and a comparative study of material models," *Journal of elasticity and the physical science of solids*, vol. 61, no. 1-3, pp. 1–48, 2000.

[73] G. A. Holzapfel and R. W. Ogden, "Constitutive modelling of passive myocardium: a structurally based framework for material characterization," *Philosophical Transactions of the Royal Society A: Mathematical, Physical and Engineering Sciences*, vol. 367, no. 1902, pp. 3445–3475, 2009.

[74] J. Humphrey, R. Strumpf, and F. Yin, "Determination of a constitutive relation for passive myocardium: I. a new functional form," *Journal of biomechanical engineering*, vol. 112, no. 3, pp. 333–339, 1990.

[75] J. Humphrey, R. Strumpf, and F. Yin, "Determination of a constitutive relation for passive myocardium: Ii.parameter estimation," *Journal of biomechanical engineering*, vol. 112, no. 3, pp. 340–346, 1990.

[76] J. Murphy, "Transversely isotropic biological, soft tissue must be modelled using both anisotropic invariants," *European Journal of Mechanics-A/Solids*, vol. 42, pp. 90–96, 2013.

[77] J. Murphy, "Evolution of anisotropy in soft tissue," *Proceedings of the Royal Society A: Mathematical, Physical and Engineering Sciences*, vol. 470, no. 2161, p. 20130548, 2014.

[78] C. Horgan and J. Murphy, "Some unexpected behaviour in shear for elasticity models of arterial tissue that only use the i 1, i 4, i 6 invariants," *IMA Journal of Applied Mathematics*, vol. 79, no. 5, pp. 820–829, 2014.

[79] C. Horgan and J. Murphy, "The counterintuitive out-of-plane strength of some incompressible orthotropic hyperelastic materials," *International Journal of Solids and Structures*, vol. 115, pp. 170–179, 2017.

[80] J. Murphy and S. Biwa, "The counterintuitive mechanical response in simple tension of arterial models that are separable functions of the i1, i4, i6 invariants," *International Journal of Non-Linear Mechanics*, vol. 90, pp. 72–81, 2017.

[81] D. M. Milewicz, S. K. Prakash, and F. Ramirez, "Therapeutics targeting drivers of thoracic aortic aneurysms and acute aortic dissections: insights from predisposing genes and mouse models," *Annual review of medicine*, vol. 68, pp. 51–67, 2017.

[82] C. van Baardwijk and M. R. Roach, "Factors in the propagation of aortic dissections in canine thoracic aortas," *Journal of biomechanics*, vol. 20, no. 1, pp. 67–73, 1987.

[83] R. Rivlin and A. G. Thomas, "Rupture of rubber. i. characteristic energy for tearing," *Journal of polymer science*, vol. 10, no. 3, pp. 291–318, 1953.

[84] C. M. Witzenburg, R. Y. Dhume, S. B. Shah, C. E. Korenczuk, H. P. Wagner, P. W. Alford, and V. H. Barocas, "Failure of the porcine ascending aorta: multidirectional experiments and a unifying microstructural model," *Journal of biomechanical engineering*, vol. 139, no. 3, p. 031005, 2017.

[85] A. R. Rao, *Peeling and torsional shear of the porcine thoracic aorta*. PhD thesis, Texas A&M University, 2019.

[86] J. Tong, Y. Cheng, and G. A. Holzapfel, "Mechanical assessment of arterial dissection in health and disease: advancements and challenges," *Journal of biomechanics*, vol. 49, no. 12, pp. 2366–2373, 2016.

[87] M. Kozuń, M. Kobielarz, A. Chwiłkowska, and C. Pezowicz, "The impact of development of atherosclerosis on delamination resistance of the thoracic aortic wall," *Journal of the mechanical behavior of biomedical materials*, vol. 79, pp. 292–300, 2018.

[88] S. Pal, A. Tsamis, S. Pasta, A. D'Amore, T. G. Gleason, D. A. Vorp, and S. Maiti, "A mechanistic model on the role of radially-running collagen fibers on dissection properties of human ascending thoracic aorta," *Journal of biomechanics*, vol. 47, no. 5, pp. 981–988, 2014.

[89] H. Wolinsky and S. Glagov, "A lamellar unit of aortic medial structure and function in mammals," *Circulation research*, vol. 20, no. 1, pp. 99–111, 1967.

[90] M. Kozuń, T. Płonek, M. Jasiński, and J. Filipiak, "Effect of dissection on the mechanical properties of human ascending aorta and human ascending aorta aneurysm," *Acta of bioengineering and biomechanics*, vol. 21, no. 2, 2019.

[91] M. Kozuń, "Delamination properties of the human thoracic arterial wall with early stage of atherosclerosis lesions," *Journal of Theoretical and Applied Mechanics*, vol. 54, 2016.

[92] S. A. OLeary, B. J. Doyle, and T. M. McGloughlin, "The impact of long term freezing on the mechanical properties of porcine aortic tissue," *Journal of the mechanical behavior of biomedical materials*, vol. 37, pp. 165–173, 2014.

[93] D. B. Alfson and S. W. Ham, "Type b aortic dissections: current guidelines for treatment," *Cardiology clinics*, vol. 35, no. 3, pp. 387–410, 2017.

[94] J. M. Atienza, G. V. Guinea, F. J. Rojo, R. J. Burgos, C. García-Montero, F. J. Goicolea, P. Aragoncillo, and M. Elicesa, "The influence of pressure and temperature on the behavior of the human aorta and carotid arteries," *Revista Española de Cardiología (English Edition)*, vol. 60, no. 3, pp. 259–267, 2007.

[95] Y. Wang, J. Hahn, and Y. Zhang, "Mechanical properties of arterial elastin with water loss," *Journal of biomechanical engineering*, vol. 140, no. 4, 2018.

[96] C. Martin, T. Pham, and W. Sun, "Significant differences in the material properties between aged human and porcine aortic tissues," *European Journal of Cardio-Thoracic Surgery*, vol. 40, no. 1, pp. 28–34, 2011.

[97] R. Grant, "Content and distribution of aortic collagen, elastin and carbohydrate in different species," *Journal of atherosclerosis research*, vol. 7, no. 4, pp. 463–472, 1967.

[98] Y. Hosoda, K. Kawano, F. Yamasawa, T. Ishii, T. Shibata, and S. Inayama, "Age-dependent changes of collagen and elastin content in human aorta and pulmonary artery," *Angiology*, vol. 35, no. 10, pp. 615–621, 1984.

[99] P. B. Dobrin, "Biaxial anisotropy of dog carotid artery: estimation of circumferential elastic modulus," *Journal of biomechanics*, vol. 19, no. 5, pp. 351–358, 1986.

[100] J. Humphrey, T. Kang, P. Sakarda, and M. Anjanappa, "Computer-aided vascular experimentation: a new electromechanical test system," *Annals of biomedical engineering*, vol. 21, no. 1, pp. 33–43, 1993.

[101] C. S. Roy, "The elastic properties of the arterial wall," *The Journal of physiology*, vol. 3, no. 2, pp. 125–159, 1881.

[102] R. N. Vaishnav, J. Vossoughi, D. J. Patel, L. N. Cothran, B. R. Coleman, and E. L. Ison-Franklin, "Effect of hypertension on elasticity and geometry of aortic tissue from dogs," *Journal of biomechanical engineering*, vol. 112, no. 5, pp. 70–74, 1990.

[103] H. W. Weizsäcker and T. D. Kampp, "Passive elastic properties of the rat aorta.," *Biomedizinische Technik. Biomedical engineering*, vol. 35, no. 10, pp. 224–234, 1990.

[104] M. Lillie and J. Gosline, "The effects of polar solutes on the viscoelastic behavior of elastin," *Biorheology*, vol. 30, no. 3-4, pp. 229–242, 1993.

[105] M. Lillie and J. Gosline, "Swelling and viscoelastic properties of osmotically stressed elastin," *Biopolymers*, vol. 39, no. 5, pp. 641–652, 1996.

[106] Y. Zou and Y. Zhang, "The orthotropic viscoelastic behavior of aortic elastin," *Biomechanics and modeling in mechanobiology*, vol. 10, no. 5, pp. 613–625, 2011.

[107] V. Kumar, A. K. Abbas, N. Fausto, and J. C. Aster, *Robbins and Cotran pathologic basis of disease, professional edition e-book*. Elsevier health sciences, 2014.

[108] K. R. Rajagopal and K. Rajagopal, "Modeling of the aorta: Complexities and inadequacies," *AORTA Journal*, vol. 8, no. 4, p. 91, 2020.

[109] D. J. Patel, D. L. Fry, and J. S. Janicki, "The elastic symmetry of arterial segments in dogs," *Circulation research*, vol. 24, no. 1, pp. 1–8, 1969.

[110] H. W. Weizsacker and J. G. Pinto, "Isotropy and anisotropy of the arterial wall," *Journal of biomechanics*, vol. 21, no. 6, pp. 477–487, 1988.

[111] J. P. V. Geest, M. S. Sacks, and D. A. Vorp, "The effects of aneurysm on the biaxial mechanical behavior of human abdominal aorta," *Journal of biomechanics*, vol. 39, no. 7, pp. 1324–1334, 2006.

[112] G. A. Holzapfel, G. Sommer, C. T. Gasser, and P. Regitnig, "Determination of layer-specific mechanical properties of human coronary arteries with nonatherosclerotic intimal thickening and related constitutive modeling," *American Journal of Physiology-Heart and Circulatory Physiology*, vol. 289, no. 5, pp. H2048–H2058, 2005.

[113] M. L. Raghavan, M. W. Webster, and D. A. Vorp, "Ex vivo biomechanical behavior of abdominal aortic aneurysm: assessment using a new mathematical model," *Annals of biomedical engineering*, vol. 24, no. 5, pp. 573–582, 1996.

[114] C. E. Korenczuk, L. E. Votava, R. Y. Dhume, S. B. Kizilski, G. E. Brown, R. Narain, and V. H. Barocas, "Isotropic failure criteria are not appropriate for anisotropic fibrous biological tissues," *Journal of biomechanical engineering*, vol. 139, no. 7, 2017.

[115] Q. Chen, Y. Wang, and Z.-Y. Li, "Re-examination of the mechanical anisotropy of porcine thoracic aorta by uniaxial tensile tests," *Biomedical engineering online*, vol. 15, no. 2, pp. 493–506, 2016.

[116] M. Jiang, R. L. Sridhar, A. B. Robbins, A. D. Freed, and M. R. Moreno, "A versatile biaxial testing platform for soft tissues," *Journal of the Mechanical Behavior of Biomedical Materials*, p. 104144, 2020.

[117] J. Blaber, B. Adair, and A. Antoniou, "Ncorr: open-source 2d digital image correlation matlab software," *Experimental Mechanics*, vol. 55, no. 6, pp. 1105–1122, 2015.

[118] S. Zeinali-Davarani, M.-J. Chow, R. Turcotte, and Y. Zhang, "Characterization of biaxial mechanical behavior of porcine aorta under gradual elastin degradation," *Annals of biomedical engineering*, vol. 41, no. 7, pp. 1528–1538, 2013.

[119] J. Ferruzzi, D. A. Vorp, and J. Humphrey, "On constitutive descriptors of the biaxial mechanical behaviour of human abdominal aorta and aneurysms," *Journal of the Royal Society Interface*, vol. 8, no. 56, pp. 435–450, 2011.

[120] M. R. Hill, X. Duan, G. A. Gibson, S. Watkins, and A. M. Robertson, "A theoretical and non-destructive experimental approach for direct inclusion of measured collagen orientation and recruitment into mechanical models of the artery wall," *Journal of biomechanics*, vol. 45, no. 5, pp. 762–771, 2012.

[121] Y. Zou and Y. Zhang, "An experimental and theoretical study on the anisotropy of elastin network," *Annals of biomedical engineering*, vol. 37, no. 8, pp. 1572–1583, 2009.

[122] N. Gundiah, M. B. Ratcliffe, and L. A. Pruitt, "The biomechanics of arterial elastin," *Journal of the Mechanical Behavior of Biomedical Materials*, vol. 2, no. 3, pp. 288–296, 2009.

[123] J. Humphrey, "Vascular adaptation and mechanical homeostasis at tissue, cellular, and sub-cellular levels," *Cell biochemistry and biophysics*, vol. 50, no. 2, pp. 53–78, 2008.

[124] K. R. Rajagopal and A. R. Srinivasa, "On the thermomechanics of materials that have multiple natural configurations part i: Viscoelasticity and classical plasticity," *Zeitschrift für angewandte Mathematik und Physik ZAMP*, vol. 55, no. 5, pp. 861–893, 2004.

[125] K. R. Rajagopal and A. R. Srinivasa, "On the thermomechanics of materials that have multiple natural configurations. part ii: Twinning and solid to solid phase transformation," *Zeitschrift für angewandte Mathematik und Physik*, vol. 55, no. 6, pp. 1074–1093, 2004.

[126] J. Humphrey and K. Rajagopal, "A constrained mixture model for growth and remodeling of soft tissues," *Mathematical models and methods in applied sciences*, vol. 12, no. 03, pp. 407–430, 2002.

[127] M. L. Raghavan, J. Kratzberg, E. M. C. de Tolosa, M. M. Hanaoka, P. Walker, and E. S. da Silva, "Regional distribution of wall thickness and failure properties of human abdominal aortic aneurysm," *Journal of biomechanics*, vol. 39, no. 16, pp. 3010–3016, 2006.

[128] S. Sherifova, G. Sommer, C. Viertler, P. Regitnig, T. Caranasos, M. A. Smith, B. E. Griffith, R. W. Ogden, and G. A. Holzapfel, "Failure properties and microstructure of healthy and aneurysmatic human thoracic aortas subjected to uniaxial extension with a focus on the media," *Acta biomaterialia*, vol. 99, pp. 443–456, 2019.

[129] C. Sang, S. Maiti, R. N. Fortunato, J. Kofler, and A. M. Robertson, "A uniaxial testing approach for consistent failure in vascular tissues," *Journal of biomechanical engineering*, vol. 140, no. 6, 2018.

[130] Y. Fung, K. Fronek, and P. Patitucci, "Pseudoelasticity of arteries and the choice of its mathematical expression," *American Journal of Physiology-Heart and Circulatory Physiology*, vol. 237, no. 5, pp. H620–H631, 1979.

[131] A. Goriely and M. Tabor, "Rotation, inversion and perversion in anisotropic elastic cylindrical tubes and membranes," *Proceedings of the Royal Society A: Mathematical, Physical and Engineering Sciences*, vol. 469, no. 2153, p. 20130011, 2013.

[132] S. G. Lekhnitskii, "Anisotropic plates," tech. rep., Foreign Technology Div Wright-Patterson Afb Oh, 1968.

[133] G. David and J. Humphrey, "Redistribution of stress due to a circular hole in a nonlinear anisotropic membrane," *Journal of biomechanics*, vol. 37, no. 8, pp. 1197–1203, 2004.

[134] A. J. M. Spencer, "Constitutive theory for strongly anisotropic solids," in *Continuum theory of the mechanics of fibre-reinforced composites*, pp. 1–32, Springer, 1984.

[135] R. W. Penn, "Volume changes accompanying the extension of rubber," *Transactions of the Society of Rheology*, vol. 14, no. 4, pp. 509–517, 1970.

[136] K. Paranjothi, U. Saravanan, R. Krishnakumar, and K. Balakrishnan, "Mechanical properties of abnormal human aortic and mitral valves," in *Mechanics of Biological Systems and Materials, Volume 2*, pp. 65–72, Springer, 2011.

[137] S. Jahnavi, U. Saravanan, N. Arthi, G. Bhuvaneshwar, T. Kumary, S. Rajan, and R. Verma, "Biological and mechanical evaluation of a bio-hybrid scaffold for autologous valve tissue engineering," *Materials Science and Engineering: C*, vol. 73, pp. 59–71, 2017.

[138] J. Merodio and R. Ogden, "Material instabilities in fiber-reinforced nonlinearly elastic solids under plane deformation," *Archives of Mechanics*, vol. 54, no. 5-6, pp. 525–552, 2002.

[139] C. O. Horgan and M. G. Smayda, "The importance of the second strain invariant in the constitutive modeling of elastomers and soft biomaterials," *Mechanics of Materials*, vol. 51, pp. 43–52, 2012.

[140] G. Savin, *Stress distribution around holes*. National Aeronautics and Space Administration, 1970.

[141] J. A. Elefteriades and E. A. Farkas, "Thoracic aortic aneurysm: clinically pertinent controversies and uncertainties," *Journal of the American College of Cardiology*, vol. 55, no. 9, pp. 841–857, 2010.

[142] J. C. Criscione, "Rivlins representation formula is ill-conceived for the determination of response functions via biaxial testing," in *The Rational Spirit in Modern Continuum Mechanics*, pp. 197–215, Springer, 2004.

[143] J. C. Criscione, "A constitutive framework for tubular structures that enables a semi-inverse solution to extension and inflation," *Journal of Elasticity*, vol. 77, no. 1, pp. 57–81, 2004.

[144] M. Itskov and N. Aksel, "A class of orthotropic and transversely isotropic hyperelastic constitutive models based on a polyconvex strain energy function," *International journal of solids and structures*, vol. 41, no. 14, pp. 3833–3848, 2004.

[145] M. Latorre and F. J. Montáns, "What-you-prescribe-is-what-you-get orthotropic hyperelasticity," *Computational Mechanics*, vol. 53, no. 6, pp. 1279–1298, 2014.

[146] M. Rubin and M. Jabareen, "Physically based invariants for nonlinear elastic orthotropic solids," *Journal of Elasticity*, vol. 90, no. 1, pp. 1–18, 2008.

[147] M. Shariff, "Nonlinear transversely isotropic elastic solids: an alternative representation," *Quarterly journal of mechanics and applied mathematics*, vol. 61, no. 2, pp. 129–149, 2008.

[148] M. Shariff, "Physical invariants for nonlinear orthotropic solids," *International journal of solids and structures*, vol. 48, no. 13, pp. 1906–1914, 2011.

APPENDIX A

Appendix A

Figure A.1 shows the variation of the nominal stress with nominal stretch, and figures A.2, A.3 and A.4 show the dependence of E_{XX}, E_{YY} and E_{XY}, respectively on nominal stretch for the loading part of the 8^{th} cycle.

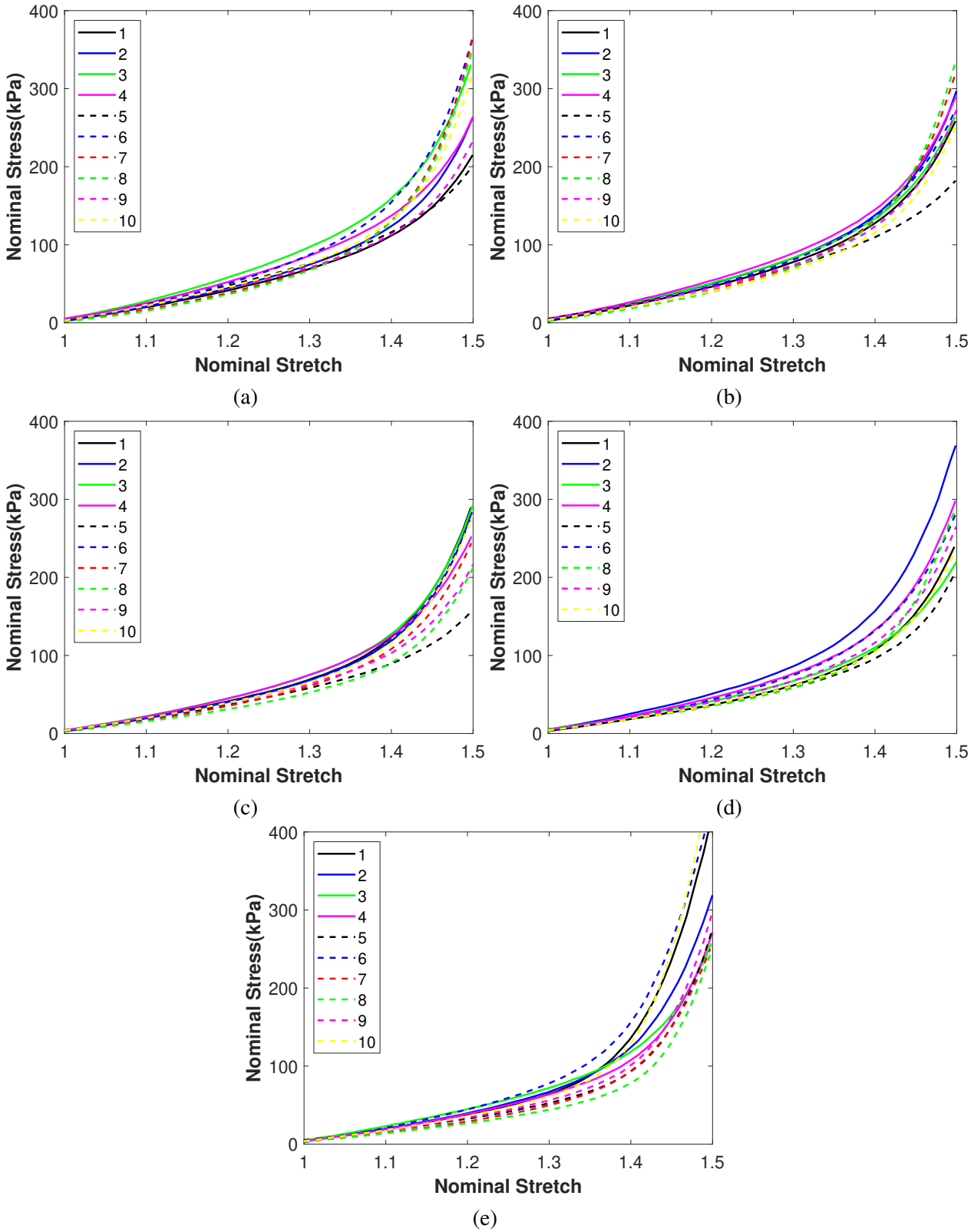

Figure A.1: Variation of the nominal stress with nominal stretch for samples oriented at (a)0^o (circ), (b) 30^o, (c) 45^o, (d) 60^o, (e) 90^o (long) with the circumferential direction for the loading part of 8^{th} cycle. The legend in the figure indicates the aorta from which the specimen is obtained.

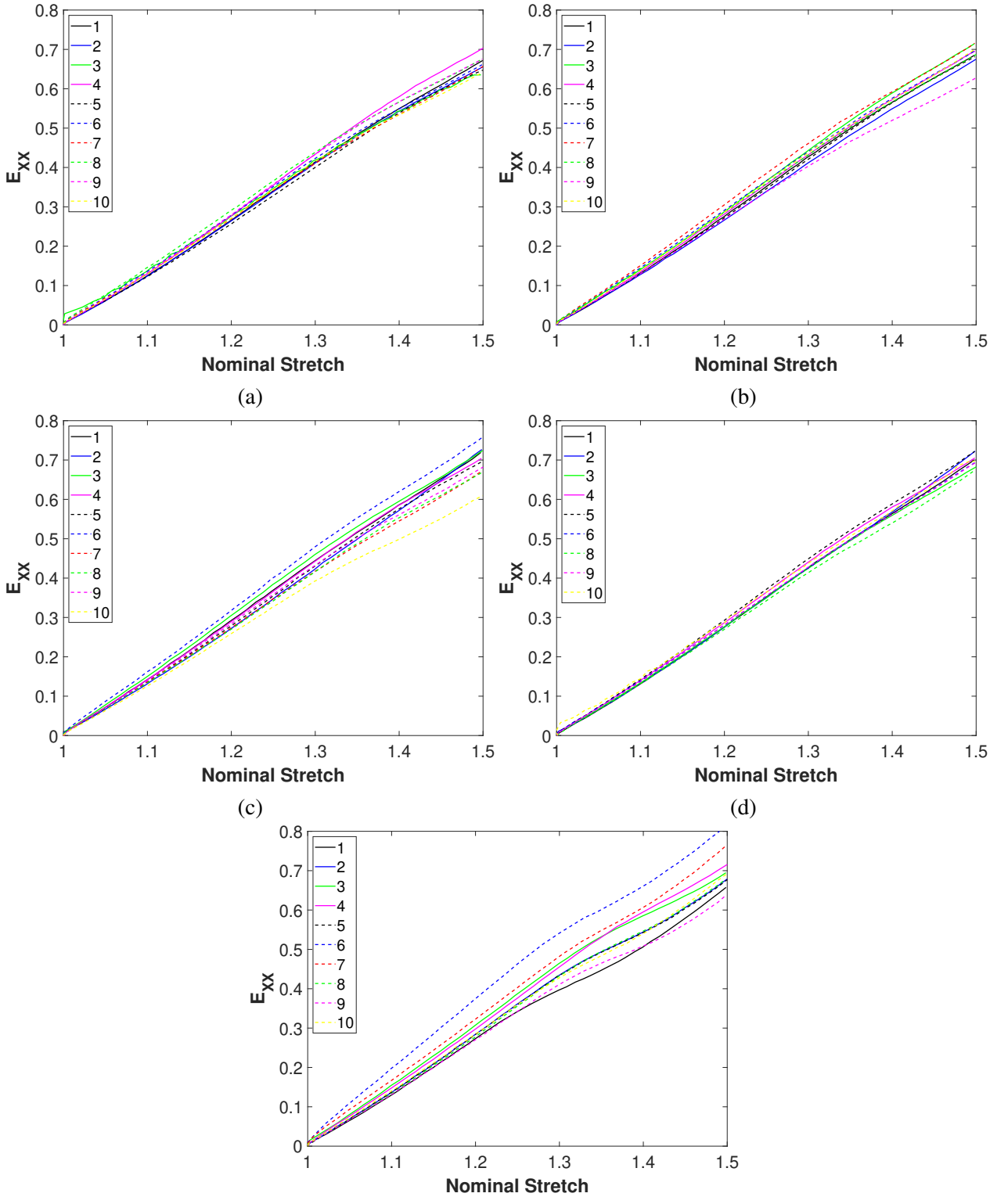

Figure A.2: Variation of E_{XX} with nominal stretch for samples oriented at (a)0^o (circ), (b) 30^o, (c) 45^o, (d) 60^o, (e) 90^o (long) with the circumferential direction for the loading part of 8^{th} cycle. The legend in the figure indicates the aorta from which the specimen is obtained.

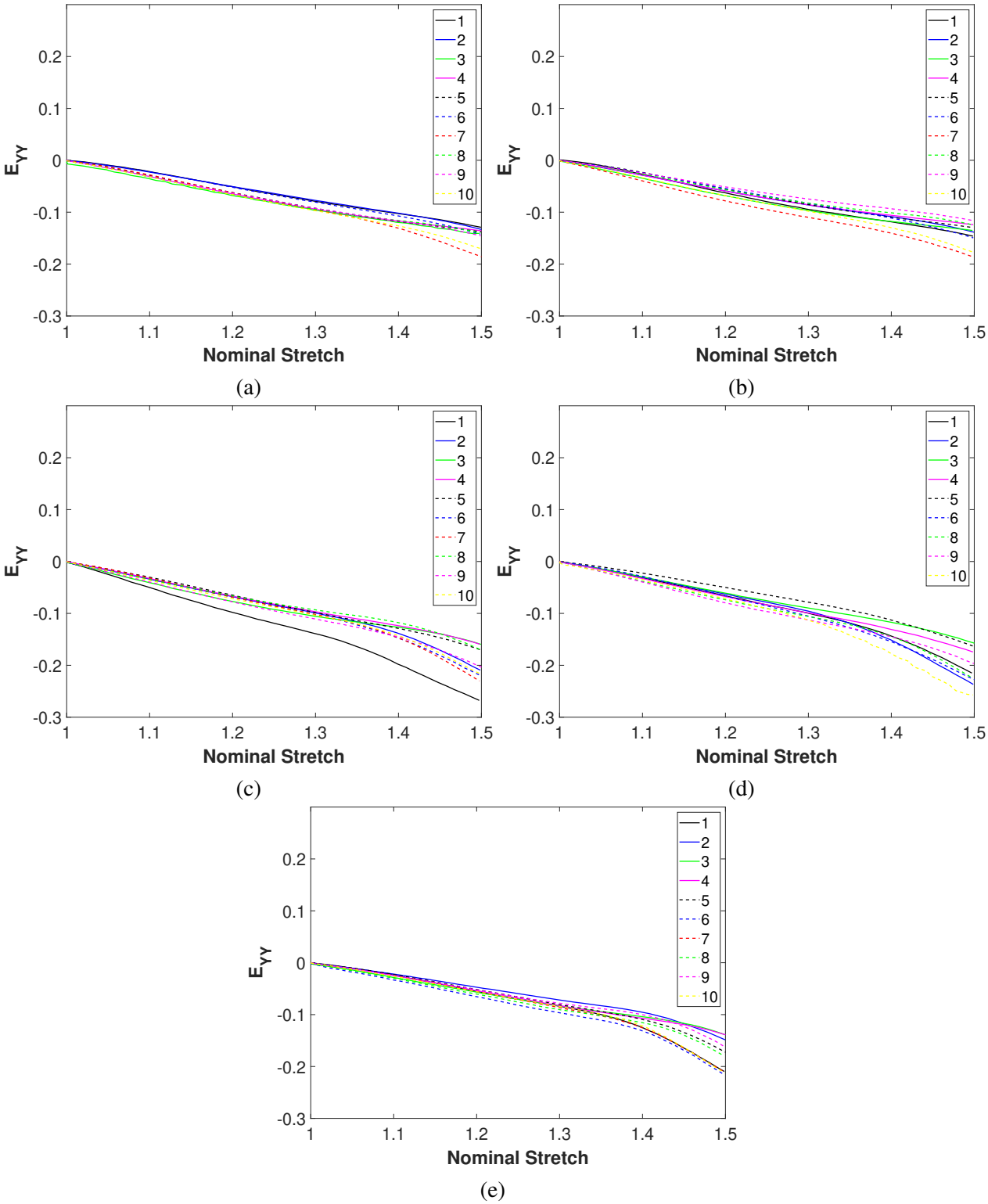

Figure A.3: Variation of E_{YY} with nominal stretch for samples oriented at (a)0^o (circ), (b) 30^o, (c) 45^o, (d) 60^o, (e) 90^o (long) with the circumferential direction for the loading part of 8^{th} cycle. The legend in the figure indicates the aorta from which the specimen is obtained.

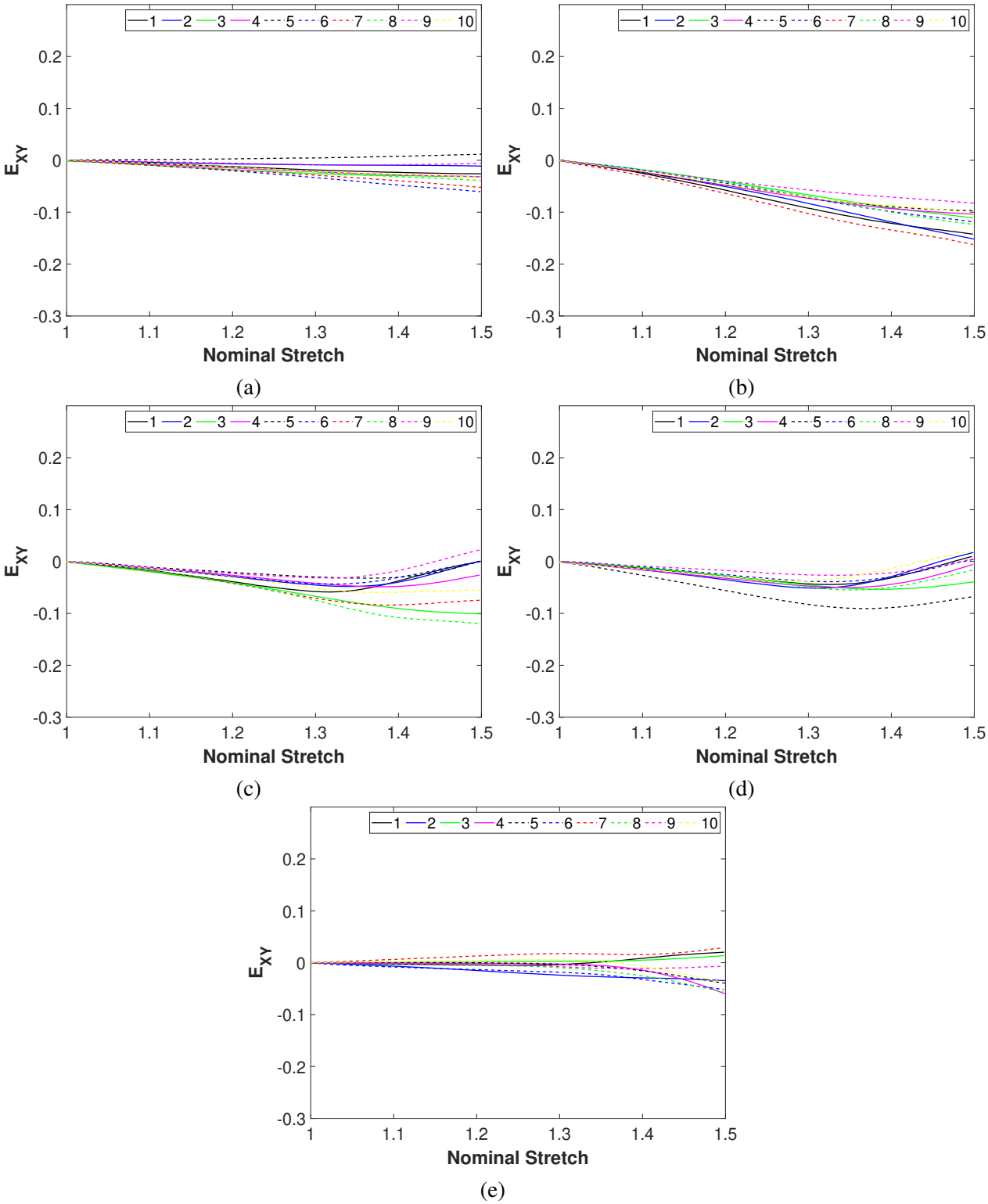

Figure A.4: Variation of E_{XY} with nominal stretch for samples oriented at (a)0^o (circ), (b) 30^o, (c) 45^o, (d) 60^o, (e) 90^o (long) with the circumferential direction for the loading part of 8^{th} cycle. The legend in the figure indicates the aorta from which the specimen is obtained.